UNIVERSITY OF CALIFORNIA, SAN DIEGO

Gas-Source Molecular Beam Epitaxial Growth and Characterization of the (Al,In,Ga)NP/GaP Material System and Its Applications to Light-Emitting Diodes

A dissertation submitted in partial satisfaction of the
requirements for the degree Doctor of Philosophy
in
Electrical Engineering (Applied Physics)

by

Vladimir Odnoblyudov

Committee in charge:

Professor Charles Tu, Chair
Professor Leonid Butov
Professor John Crowell
Professor Yu-Hwa Lo
Professor Paul Yu

2006

The dissertation of Vladimir Odnoblyudov is approved, and it is acceptable in quality and form for publication on microfilm:

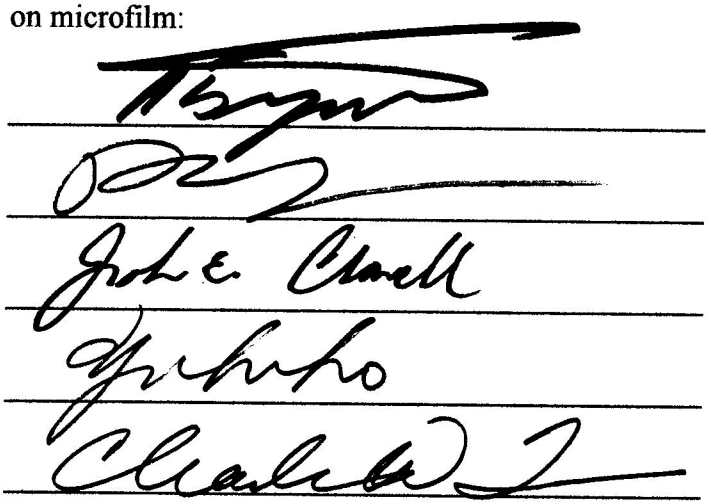

Chair

University of California, San Diego

2006

To my wife Alla and son Alan

Table of Contents

Signature Page……iii

Dedication……...iv

Table of Contents…….....v

List of figures…….....viii

Acknowledgments……xiii

Vita ……..……...xv

Abstract…….xix

Chapter 1. Introduction……1

1.1. Background……..1

1.2. Current status……...3

1.2.1. Light-emitting diodes…….3

1.2.2. Dilute nitrides…….……...12

1.3. Tasks and proposed approach……19

1.4. Scope of the dissertation……21

References……..24

Chapter 2. Experimental details……31

2.1. Overview……....31

2.2. GSMBE growth system with nitrogen plasma source……...32

2.3. Characterization…….…39

2.3.1. Material characterization…….……39

2.3.2. Light-emitting diode characterization……..43

2.4. LED fabrication…….44

References……..48

Chapter 3. Growth and characterization of (Al,In,Ga)NP……..49

3.1. Overview……49
3.2. Growth and characterization of GaNP layers……50
3.2.1. Growth details……..50
3.2.2. Optical properties……52
3.2.3. Structural properties…….……58
3.3. AlGaNP bulk layers……...61
3.3.1. Growth and characterization details…….61
3.3.2. Thermodynamic analysis and structural properties…….63
3.4. InGaNP quantum wells……..70
3.4.1. Growth details……..70
3.4.2. Optical properties……72
3.4.3. Electron effective mass……78
3.4.4. InGaNP/GaP band offsets……....81
3.5. Conclusions……....86
References……..88

Chapter 4. (Al,In,Ga)NP-based light-emitting diodes…….90

4.1. Overview……90
4.2. Fabrication of (Al,In,Ga)NP LED chips……91
4.2.1. General procedures……..91
4.2.2. Contacts optimization……..92
4.3. Band offsets of (Al,In,Ga)NP and AlInGaP LED structures……....99
4.4. LED growth details……..103
4.5. LEDs with a bulk GaNP active region…….106
4.5.1. LED chip characterization…….107
4.5.2. Color stability…….112
4.6. InGaNP QW-based LEDs……114
4.6.1. Single and multiple quantum well LEDs……...…115
4.6.2. Current overflow in the quantum well……...118
4.7. Effect of AlGaP claddings……...120

4.8. Conclusions……..126
References……128

Chapter 5. Summary and suggestions for future work…….129

5.1. Summary……..129
5.2. Accomplished tasks…….132
5.3. Suggestions for future work…….133
References……137

Appendix A. Metamorphic growth of InGaP layers on GaP (100) substrates…...138

A.1. Overview……..138
A.2. Growth and characterization details…….139
A.3. Optical and structural properties……..140
A.4. Conclusions……..146
References……148

List of figures

Chapter 1.

Figure 1.1. Different approaches to obtain white light……...5

Figure 1.2. Luminous efficiency of visible-spectrum LEDs and other light sources versus time (adopted from E. Fred Shubert, *Light Emitting Diodes*, 2003)…….....5

Figure 1.3. State-of-the-art LED internal quantum efficiency versus the wavelength (adopted from Paul S. Martin, Lumileds, IEEE Santa Clara, 2003)…..……...7

Figure 1.4. Typical emission spectrum of InGaN/GaN blue, InGaN/GaN green, and AlInGaP/GaAs red LEDs at room temperature (after Toyoda Gosei Corp., 2000)…..……...9

Figure 1.5. Typical light output power versus injection current of InGaN/GaN blue, InGaN/GaN green, and AlInGaP/GaAs red LEDs at room temperature (after Toyoda Gosei Corp., 2000)……..……9

Figure 1.6. Typical output intensity of InGaN/GaN blue, InGaN/GaN green, and AlInGaP/GaAs red LEDs versus ambient temperature (after Toyoda Gosei Corp., 2000)……..……..10

Figure 1.7. Typical forward current-voltage (I-V) characteristic of InGaN/GaN blue, InGaN/GaN green, and AlInGaP/GaAs red LEDs at room temperature (after Toyoda Gosei Corp., 2000)…… ……...10

Chapter 2.

Figure 2.1. Schematic of the modified Varian GEN II Gas-Source Molecular Beam Epitaxy system……..……..33

Figure 2.2. Nitrogen plasma source……..35

Figure 2.3. Optical emission spectrum of the nitrogen plasma source…….36

Figure 2.4. The optical intensity – nitrogen flux diagram for the nitrogen plasma source……38

Figure 2.5. Schematic of the photoluminescence measurement system…….....40

Figure 2.6. Schematic of the x-ray measurement system…….41

Figure 2.7. Schematic of the electroluminescence measurement system…….43

Chapter 3.

Figure 3.1. A schematic of the GaNP test sample……...51

Figure 3.2. a) Dependence of the PL peak wavelength on nitrogen composition in GaNP at room temperature; b) RT PL spectrums of: 1 – test structure with [N]=0.62%, 2 - test structure with [N]=1.17%.....53

Figure 3.3. Dependence of RT PL intensity and FWHM of RT PL peak of $GaN_{0.006}P_{0.994}$ bulk layers on substrate temperature …….…….54

Figure 3.4. Dependence of PL intensity of $GaN_{0.0062}P_{0.9938}$ layer on layer thickness….55

Figure 3.5. A band diagram of GaP/GaNP/GaP double heterostructure……56

Figure 3.6. a) Dependence of the photon energy vs. temperature for 70-Å-thick $GaN_{0.005}P$ QW. Symbols are experimental data, and solid lines are the best Varshni fit; b) PL spectrums for the 70-Å-thick $GaN_{0.005}P$ QW, taken at different temperatures…….……...58

Figure 3.7. (400) x-ray rocking curves for 100-nm-thick GaNP layers with different nitrogen concentrations ([N] = 0.4%, 0.6%, 1.16%)…….……59

Figure 3.8. Dependence of the FWHM of x-ray peak of $GaN_{0.006}P_{0.994}$ bulk layer on substrate temperature……..……60

..

Figure 3.9. (400) x-ray diffraction rocking curves of AlNP layers with the nitrogen composition varied from 0 to 4.21%.....62

Figure 3.10. Dependence of the nitrogen composition in AlNP and GaNP layers on plasma intensity….……64

Figure 3.11. Dependence of free Gibbs energy on the substrate temperature for Reactions formation of AlP, GaP, GaN and AlN…… ……...66

Figure 3.12. (004) x-ray diffraction rocking curves of 0.1-μm-thick AlGaNP layers with different nitrogen and aluminum composition. The peak positions from AlGaNP epi-layers are indicated…….……..67

Figure 3.13. a) Nitrogen concentration in AlGaNP layers vs. aluminum composition for the same plasma source conditions used; b) full widths at half maximum of (004) x-ray diffraction peaks vs. aluminum composition in the AlGaNP layer……...68

Figure 3.14. Photoluminescence spectra of as-grown and annealed 7-nm-thick $In_{0.1}GaN_{0.005}P$ quantum well in GaP barriers……73

Figure 3.15. a) Dependence of transition energy in $In_yGa_{1-y}N_{0.008}P_{0.992}$ QW on *y*: 1 – at 20K, 2 – at 300K; 3 – dependence of RT PL intensity of $In_yGa_{1-y}N_{0.008}P_{0.992}$ QW on *y*; b) PL spectra of$In_{0.1}$ $Ga_{0.9}N_{0.008}P_{0.992}$ QW recorded at 1 – 20K, 2 – 300K……74

Figure 3.16. The x-y compositional plane for 7-nm-thick $In_yGa_{1-y}N_xP_{1-x}$ QW in GaP barriers at 300 K. Solid lines are constant direct-energy values; dashed lines are constant strain with respect to GaP; symbols are experimental data; and filled area is the indirect bandgap region of $In_yGa_{1-y}N_xP_{1-x}$ material……....75

Figure 3.17. a) Dependence of the photon energy vs. temperature for 7-nm-thick $In_{0.1}GaN_{0.005}P$ QW. Symbols are experimental data, solid lines are the best Varshni fit; b) PL spectrums for the 7-nm-thick $In_{0.1}GaN_{0.005}P$ QW, taken at different temperatures……...77

Figure 3.18. a) Dependence of the transition energy vs. quantum well width for $In_yGa_{1-y}N_{0.005}P_{0.995}$ QW with different indium concentrations: 5%, 10% and 20%; b) Dependence of the transition energy vs. inverse squared quantum well width for the QWs in.)……...79

Figure 3.19. Dependence of the electron effective mass in $In_yGa_{1-y}N_{0.005}P_{0.995}$ vs. indium concentration……...…….80

Figure 3.20. A band diagram of GaP/InGaNP/GaP double heterostructure……..82

Figure 3.21. Calculated conduction and valence band offsets of GaP/$In_yGa_{1-y}N_{0.005}P_{0.995}$/GaP as a function of y……...85

Chapter 4.

Figure 4.1. a) Micrograph of the *n*-type metal contacts, deposited on a GaP substrate; b) I-V characteristic, recorded between two *n*-type contacts……93

Figure 4.2. a) Micrograph of the p-type metal contacts, deposited on a p-type GaP contact layer; b) I-V characteristic, recorded between two *p*-type

contacts…….…….95

Figure 4.3. Dependence of the free carrier concentration on the hole mobility in p-type GaP layer……..……...96

Figure 4.4. a) Schematic of the p-i-n diode structure; b) on-wafer I-V characteristics of the *p-i-n* diode structure with different RTA time……..……98

Figure 4.5. Dependence of the EL peak energy vs. Al concentration in AlInGaP-based LEDs……..……...100

Figure 4.6. Band diagram of a GaNP-based LED…….101

Figure 4.7. Different types of LED structures studied: a) bulk GaNP - based LED; b) InGaNP single or multiple QW – based LED; c) InGaNP single QW – based LED with AlGaP cladding layers…...……...105

Figure 4.8. LED chip micrograph, taken under optical microscope……..107

Figure 4.9. Electroluminescence spectra at different drive currents of a 380 μm × 380 μm LED chip with a 0.1-μm-thick $GaN_{0.006}P_{0.994}$ active layer…..…...108

Figure 4.10. a) Normalized electroluminescence peak intensity of three LED chips with different thickness of GaNP active layer; b) normalized EL peak intensity vs. GaNP active layer thickness…….……..109

Figure 4.11. Current-voltage characteristics of three LED chips with different thickness of GaNP active layer……..……...110

Figure 4.12. Wavelength shift vs. the drive current for bare GaNP-based LED chips and AlInGaP-based LED chips……..112

Figure 4.13. Thermal resistivity of InGaP vs. In concentration in the alloy……114

Figure 4.14. EL spectra, taken at 20 mA drive current, for $In_yGa_{1-y}N_{0.005}P_{0.995}$ QW – based LEDs with y = 0, 0.14, and 0.17……...115

Figure 4.15. EL intensity vs. the drive current for LED chips with different number of QWs. Inset shows saturation current as a function of the number of QWs in the LED structure…… ……117

Figure 4.16. EL intensity vs. the drive current for bare InGaNP single QW – based LED chip (curve 1), and for LED chip in epoxy dome (curve 2)……...…117

Figure 4.17. Cross section SEM image of InGaNP single QW – based LED with AlGaP

cladding layers……121

Figure 4.18. I-V characteristics of LED structure A and LED structure B…….121

Figure 4.19. Conduction and valence band offsets of $Al_xGa_{1-x}P/GaP$ as a function of x……..……...123

Figure 4.20. Current-voltage characteristics for LED structures with different Al concentration in the cladding layer ($0 \leq x \leq 0.77$)……..124

Figure 4.21. Current-voltage characteristics of three LED chips with different thickness of GaNP active layer……...125

Chapter 5.

Figure 5.1. a) Band diagram of $Al_xGa_{1-x}P/Al_yGa_{1-y}P/Al_xGa_{1-x}P$ structure; b) band diagram of $Al_xGa_{1-x}P$ / $Al_yGa_{1-y}NP$ / $Al_xGa_{1-x}P$ structure for LED application……...135

Appendix A.

Figure A.1. Layer-by-layer schematic of Structures #1 and #2……...140

Figure A.2. AFM images at 5 μm (top row) and 20 μm (bottom row) full scale of the metamorphic buffer layer grown at (a) 500^0C and (b) 400^0C……...141

Figure A.3. (400) x-ray rocking curves of Structures #1: 1- $In_xGa_{1-x}P$ linearly graded (x from 0 to 0.3) metamorphic buffer layer; 2 - $In_{0.3}Ga_{0.7}P$ constant-composition metamorphic buffer layer……143

Figure A.4. Dependence of FWHM of x-ray peak vs. indium composition in the structures of Fig. A.3…….……..144

..

Figure A.5. a) PL spectra (recorded at 20 K) of a series of Structures #1 samples with different x; b) dependence of PL peak position and PL intensity on In composition……...145

Figure A.6. Room-temperature (curve 1) and low-temperature (curve 2) PL spectrum of Structure #2 with $In_{0.3}Ga_{0.5}P/In_{0.5}Ga_{0.5}P$ (7 nm)/$In_{0.3}Ga_{0.7}P$ QW……...146

Acknowledgements

I have been working at UCSD on my thesis for three years. I had an amazing experience here. First of all, I would like to thank my advisor Professor Charles Tu for accepting me to be his student three years ago. I came in solely as an MBE grower, and during these three years I learned material characterization, device processing, packaging and measurement. I want to cordially thank Professor Tu for guiding me throughout this long educational process, sometimes the most rewarding and sometimes disappointing. And I appreciate the most Professor Tu's advice, support, and mentoring during the disappointment times, as this truly showed his care about me.

I am sincerely grateful to Professors Paul Yu, Yu-Hwa Lo, John Crowell, and Leonid Butov for serving on my committee and making valuable suggestions to my work.

Next, I would like to thank UCSD graduate students from other research groups in the ECE department for assistance and hands-on help during the work on my dissertation. Kevin Tetz, Shadi Daeha, David Keogh and Soroubh Raychudhuri are among those whose participation was the most valuable. Thanks are also due to former students Dr. David Hong and Dr. Rebecca Welty for their generous consulting on machinery maintenance and device processing. Many thanks to friendly and professional UCSD staff, who made my work at UCSD so much easier.

There is a special acknowledgement to the research group of Laboratory of Semiconductor Nanoheterostructures at Ioffe-Physico Technical Institute, Saint-Petersburg, Russia, were I earned my Bachelor and Masters Degrees, prior to coming to UCSD. I would like to thank the most Dr. Anton Egorov – truly my first teacher and

mentor on the technology of Molecular Beam Epitaxy, who later recommended me to Professor Charles Tu. Many thanks to Dr. Alexey Kovsh for introducing me to the technology of MBE, and guiding my very first steps in learning the basics of it. I also appreciate the mentoring I received from Professor Victor Ustinov, Professor Alexey Zhukov and Professor Nikolay Ledentsov during my work in Ioffe Institute.

Most of all, I want to thank my wife, Alla, who inspired, loved and encouraged me, since I was a third-year bachelor student. Without her understanding and support I could not have finished my study at UCSD. Special thanks are also to my 18-months-old son Alan, who is an endless source of love and inspiration for me. I am indebted to my parents and my brother for giving me spiritual support.

Materials in this dissertation (Chapters 3-4, and Appendix A) were partially published in Journal of Crystal Growth 279, 20 (2005), Journal of Vacuum Science and Technology B 23, 1317 (2005), Applied Physics Letters 88, 071907 (2006), and accepted for publication in Applied Physics Letters.

Vita

July 1, 1980	Born, Saint-Petersburg, Russia
2001	B.S., Saint-Petersburg State Technical University, Russia
	(research done at Ioffe Physico-Technical Institute, Russia)
2003	M.S., Saint-Petersburg State Technical University
	(research done at Ioffe Physico-Technical Institute, Russia)
2003-2006	Research Assistant, University of California, San Diego
2006	Ph.D., University of California, San Diego

Publications in Journals

1. **V.A. Odnoblyudov** and C.W.Tu
   Room-temperature yellow-amber emission from InGaP quantum wells grown on an InGaP metamorphic buffer layer on GaP(100) substrates
   Journal of Crystal Growth 279, 20 (2005)

2. **V.A. Odnoblyudov** and C.W.Tu
   Gas-source molecular beam epitaxial growth of Ga(In)NP on GaP (100) substrates for yellow-amber light-emitting devices
   Journal of Vacuum Science and Technology B 23, 1317 (2005)

3. **V.A. Odnoblyudov** and C.W.Tu
   Growth and characterization of AlGaNP on GaP(100) substrates
   Applied Physics Letters 88, 071907 (2006)

4. **V.A. Odnoblyudov** and C.W.Tu
   Optical properties of InGaNP quantum wells grown on GaP (100) substrates by gas-source molecular beam epitaxy
   Applied Physics Letters, accepted

5. **V. A. Odnoblyudov** and C.W.Tu
   Amber GaNP-based light-emitting diodes directly grown on GaP(100) substrates
   Journal of Vacuum Science and Technology B, accepted

6. **V.A. Odnoblyudov** and C.W. Tu
   Growth and fabrication of InGaNP-based yellow-red light emitting diodes
   Applied Physics Letters, accepted

Patents filed:

1. **V.A.Odnoblyudov** and C.W.Tu
   High-efficiency light-emitting diodes
   US application # US 60 / 617465 on 10/08/2004

Conference presentations:

1. **V.A.Odnoblyudov** and C.W.Tu
   Room-Temperature Yellow-Amber Emission from InGaP Quantum Wells Grown on an InGaP Metamorphic Buffer Layer on GaP(100) Substrates
   46th Electronic Materials Conference, Notre Dame University, Notre Dame, Indiana June 23-25, 2004,

2. **V.A.Odnoblyudov** and C.W.Tu

GSMBE growth of Ga(In)NP on GaP (100) substrates for yellow-amber light-emitting devices

NAMBE Conference, Banff Center, Canada, October 10-14, 2004

3. **V.A. Odnoblyudov** and C.W.Tu

   Yellow-red light-emitting diodes directly grown on GaP substrates

   RESEARCH EXPO 2005, UCSD, February 25 (***Best Poster Award***)

4. **V.A. Odnoblyudov** and C.W.Tu

   Ga(In)NP-Based Yellow-Red Light-Emitting Diodes Directly Grown on GaP (100) Substrates

   47th Electronic Materials Conference, Santa Barbara, California, June 20-23, 2005

5. **V.A. Odnoblyudov** and C.W.Tu

   Growth and fabrication of GaInNP-based yellow-red light-emitting diodes on GaP (100) substrates

   NAMBE Conference, Santa Barbara, California, September 11-14, 2005

6. **V.A. Odnoblyudov** and C.W.Tu

   Growth and fabrication of yellow-red light-emitting diodes on GaP substrates

   RESEARCH EXPO 2006, UCSD, February 25 (***Best Poster Award***)

7. **V.A. Odnoblyudov** and C.W.Tu

   Growth and fabrication of InGaNP quantum well based yellow-red light-emitting diodes

   48th Electronic Materials Conference, Pennsylvania State University, June 27th-30th, 2006

8. C.W. Tu, **V.A. Odnoblyudov**, and Y.G. Hong

Bandgap Engineering and Device Applications of Dilute Nitrides: Ga(In)NP
2006 International Conference on Silicon Electronics and Photonics (ICSEP '06), Taipei, Taiwan, April 1-2, 2006

ABSTRACT OF THE DISSERTATION

Gas-Source Molecular Beam Epitaxial Growth and Characterization of the (Al,In,Ga)NP/GaP Material System and Its Applications to Light-Emitting Diodes

by

Vladimir Odnoblyudov

Doctor of Philosophy in Electrical Engineering (Applied Physics)

University of California, San Diego, 2006

Professor Charles W. Tu, Chair

Nitrogen incorporation into GaAs has received much attention in the last decade, because of its application to long-wavelength lasers. However, nitrogen incorporation into GaP (100) has not received much attention to date despite the promising application of this material system to yellow-amber-red light-emitting diodes. In order to investigate the not yet well-studied (Al,In,Ga)NP material system, we use gas-source molecular beam (MBE), in which nitrogen radicals are used as nitrogen precursor, to grow these mixed group-V alloy semiconductors with excellent crystallinity.

This dissertation is divided into two major parts. In the first part we describe the growth and characterization of the (Al,In,Ga)NP material system. Optical and structural properties of GaNP bulk layers, AlGaNP bulk layers, and InGaNP quantum wells are studied. The dependence of the GaNP band gap vs. nitrogen concentration and temperature dependent PL are analyzed. For AlGaNP layers, using a thermodynamic

approach we explain the difference between nitrogen incorporation into GaP and AlP. The dependence of the emission wavelength vs. nitrogen and indium compositions is studied for InGaNP QWs. The electron effective mass is determined for InGaNP materials with different indium concentration. The conduction and valence band offsets are calculated for the InGaNP/GaP heterojunction.

In the second part, we describe LED chip fabrication and contacts optimization. The development of *n*-type and *p*-type contacts is discussed. A description of LED chip processing optimization is given for a *p*-*i*-*n* diode structure. The band offsets are compared for (Al,In,Ga)NP-based LED structures and conventional AlInGaP-based LED structures; they are 2-3 times higher in LEDs based on the (Al,In,Ga)NP material system. Growth and fabrication results for bulk GaNP-based amber LEDs are discussed. Color stability (electroluminescence peak wavelength shift vs. current) is compared for GaNP-based LEDs and AlInGaP-based LEDs; the wavelength shift of (Al,In,Ga)NP-based LED chips is ~ 6 times less than that of AlInGaP-based LED chips, in the drive current range of 10 - 60 mA. The influence of In concentration in InGaNP QWs on EL properties of LED chips is reported. Single and multiple InGaNP QW-based LEDs are studied.

Chapter 1. Introduction.

1.1. Background

Semiconductor heterostructures have been playing a very important role in science and everyday life for the last several decades. Light-emitting diodes (LEDs)[1], diode lasers[2,3,4], vertical cavity surface emitting lasers (VCSELs)[5], heterojunction bipolar transistors[6,7], and solar cells[8] are examples of electronic and photonic devices built using semiconductor heterostructures. LEDs experience one of the fastest developments in semiconductor optoelectronics in recent years. Within two decades, LEDs are expected to replace conventional light sources, much like transistors replaced vacuum tubes. The rapid progress in development of semiconductor devices can be partially attributed to the improvements of the growth technology of semiconductors. The control of material properties and purity of semiconductors has been achieved from use of liquid phase epitaxy (LPE) in the early 60s to use of molecular beam epitaxy (MBE) and metal organic chemical vapor deposition (MOCVD) in the 80s. The choice of semiconductors for making a particular device is determined by specific optical and electrical design requirements and ability to grow these materials using one of the growth techniques.

Electronic band structure and lattice constant of a semiconductor are two main criteria for heterostructure design. Use of compound semiconductors, such as AlGaAs, InGaN, InGaAsP, InGaNAs and InGaNAs, gives possibilities to construct a material with

a given electronic band structure and lattice constant for a particular device application. "Bandgap engineering" is a widely used term to describe the process of creation of semiconductor heterostructures with a given band structure.

On the other hand, the search for novel materials that might exhibit new properties and/or improve existing devices is still an important issue. One of the youngest members in the family of III-V compound semiconductors is dilute nitrides (III-NV). Dilute nitrides (InGaNAs-GaAs) with a small amount of nitrogen (<4%) initially captured the attention of researchers as a potential replacement for InGaAsP-InP material system in the laser application for optical fiber communication. That is because laser diodes based on the InGaAsP-InP material system have disadvantages of relatively poor temperature stability[9] and unsuitable for distributed Bragg reflectors (DBRs) for VCSELs.

Another material system from the dilute nitride family is (Al,In,Ga)NP. Study of this alloy is interesting because of several reasons: first, $GaN_{0.02}P_{0.998}$ is lattice matched to Si and possible integration of Si-based electronics and III-V-semiconductor based optoelectronics can be realized; second, adding a small amount of nitrogen (~0.4%) converts indirect bandgap GaP into direct bandgap material and makes it efficient light emitter in the yellow-red spectral range. The second reason is a key point to motivate development of light-emitting devices (e.g., LEDs) based on dilute nitride phosphide material system. The motivation of this research is supported by the fact that substantial improvement of the existing yellow-red LED technology is required due to poor

temperature stability of conventional AlInGaP-based LEDs. A more detailed description of the history and current status of LEDs and dilute nitrides is given below.

1.2. Current status

This dissertation is devoted to a study of the (Al,In,Ga)NP material system grown on GaP (100) substrates and its application to yellow-red LEDs. Much theoretical end experimental work has been done on LEDs and III-NV dilute nitrides. The following gives an overview of the history and current status of LEDs and III-NV dilute nitrides with an emphasis on the (In,Ga)NP material system.

1.2.1. Light-emitting diodes

Right now solid-state lighting is one of the most exciting subjects in research and business. Light emitting diodes are widely used for full-color displays, signaling, traffic lights, automotive lights[10], etc. The total LED market size is estimated to be $ 3 Billion in 2005 and growing 15-20% per year. The number of applications is growing rapidly. The market size is going to grow dramatically once white LEDs reaches the level of price/performance of conventional incandescent and fluorescent lamps.

In the 1960s, several groups pursued the demonstration of semiconductor lasers. The first viable LEDs were by-products in this pursuit. During the last 40 years, LEDs

have become devices in their own right and today are versatile light sources with a bright future.

White LEDs are the ultimate goal to replace incandescent and fluorescent lamps for general lighting. Many advantages include reduced pollution caused by carbon-related elements, reduced electrical energy consumption, increased lifetime, and improved human visual experience. In contrast to many other light sources, LEDs have the potential of converting electricity to light with near-unity efficiency. Intensive work is being done now to improve the efficiency and reduce the cost of white LEDs. Much progress is expected in the area of white LEDs, since they have the potential to deliver a substantially higher luminous efficiency compared with conventional incandescent and fluorescent light sources. Whereas conventional light sources have typical luminous performance of 15-100 lm/W, white LEDs have the potential for luminous efficiencies exceeding 300 lm/W[11].

There are three main approaches to produce white light: blue LED and yellow phosphorus, ultraviolet LED plus tri-color phosphorus, and tri-color mixing from red, green and blue LED (RGB approach). These approaches are illustrated in Fig.1.1. Each of these approaches has its advantages and disadvantages, which are discussed in details in Ref. [1]. The RGB approach is theoretically the most efficient one, since it does not require absorbtion and re-emission of the light. Three wavelengths for the best RGB tri-color mixing are 460, 540 and 610 nm (see Ref. [11]). Currently, the first two are produced from AlGaInN LEDs, and the last, 610 nm, from AlGaInP LEDs grown on GaAs substrates. Figure 1.2[12] (updated by E. Fred Schubert [1] in 2000) shows the

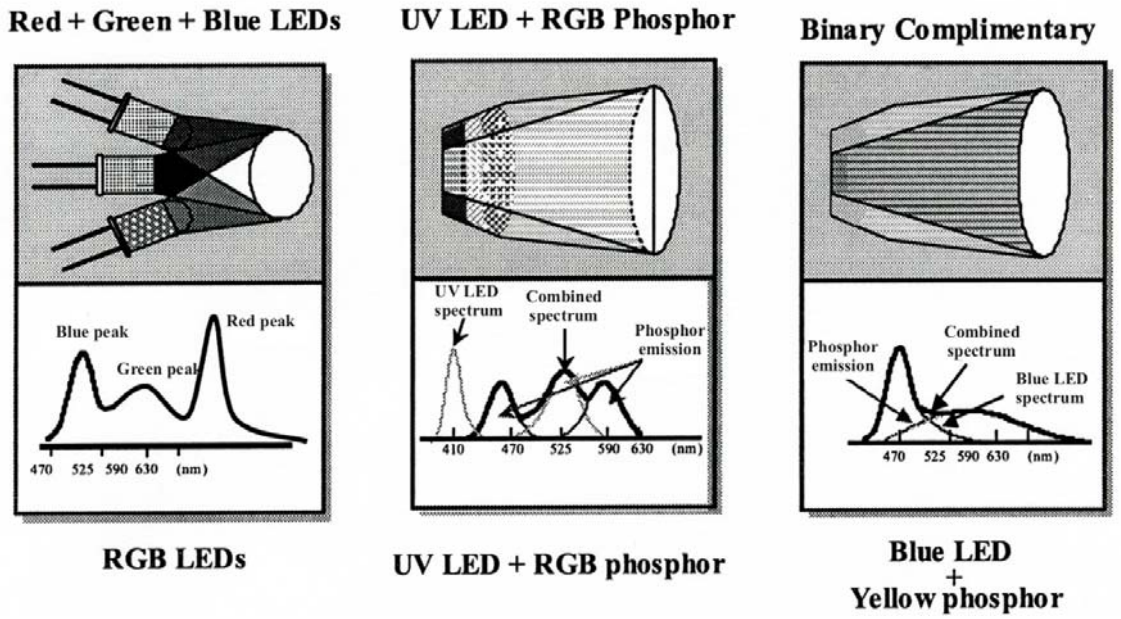

Figure 1.1. Different approaches to obtain white light.

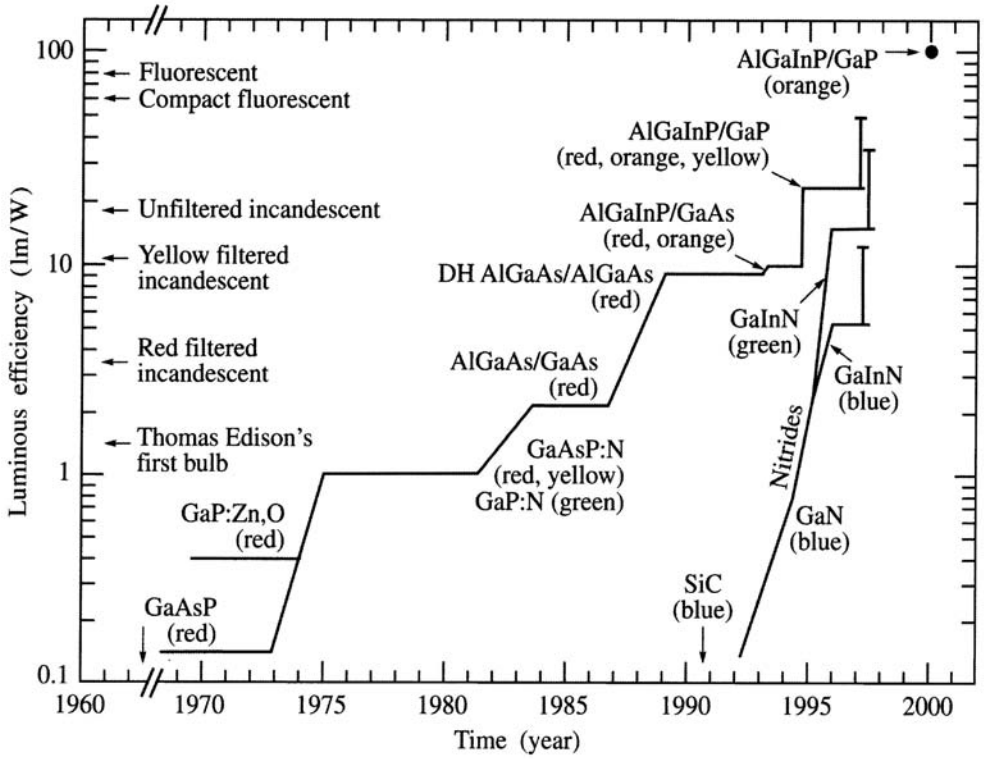

Figure 1.2. Luminous efficiency of visible-spectrum LEDs and other light sources versus time (adopted from E. Fred Shubert, *Light Emitting Diodes*, 2003).

evolution of different LED's performance (luminous efficiency) with time to the state-of-the-art LEDs. One can see that AlInGaP-based and InGaN-based LEDs are the brightest in the yellow-red and blue-green spectral regions, respectively.

Ultraviolet, blue and green LEDs are produced using the AlGaInN material system grown on sapphire substrates. First GaN p-n-homojunction LED was reported by Akasaki *et al*, subsequently after the discovery of the p-type doping of GaN with Mg[13]. These LEDs were grown on sapphire substrates. LEDs had an efficiency of about 1%, which was surprisingly high for this highly dislocated material grown on a mismatched substrate. It also was the first demonstration that nitride LED efficiencies are not affected by dislocations in the same way as III-V arsenide and phosphide light-emitters. The closest name associated with GaN LEDs and lasers is the Nichia Chemical Industries Corporation, Japan. A team of researchers that included Shuji Nakamura has made numerous contributions to the development of GaN growth, LEDs and lasers. They first demonstrated viable blue and green InGaN double-heterostructure LEDs[14,15,16] that achieved efficiencies of 10%[17], and the demonstration of the first pulsed and CW InGaN/GaN blue laser operating at room temperature[18]. The InGaN material system is also suited for white LEDs, based on phosphor wavelength converters[19] and on semiconductor wavelength converters[20].

There is a decrease in internal quantum efficiency (Fig. 1.3) of GaN-based LEDs[21] in the 500-550 nm range due to the high indium concentration required in InGaN quantum wells (QW). High indium concentration results in a large strain, and phase separation in the QW occurs, which decreases the internal quantum efficiency

substantially. Figure 1.3 shows that the internal quantum efficiency of the yellow-red AlInGaP-based LEDs also decreases from 650 nm to 600 nm.

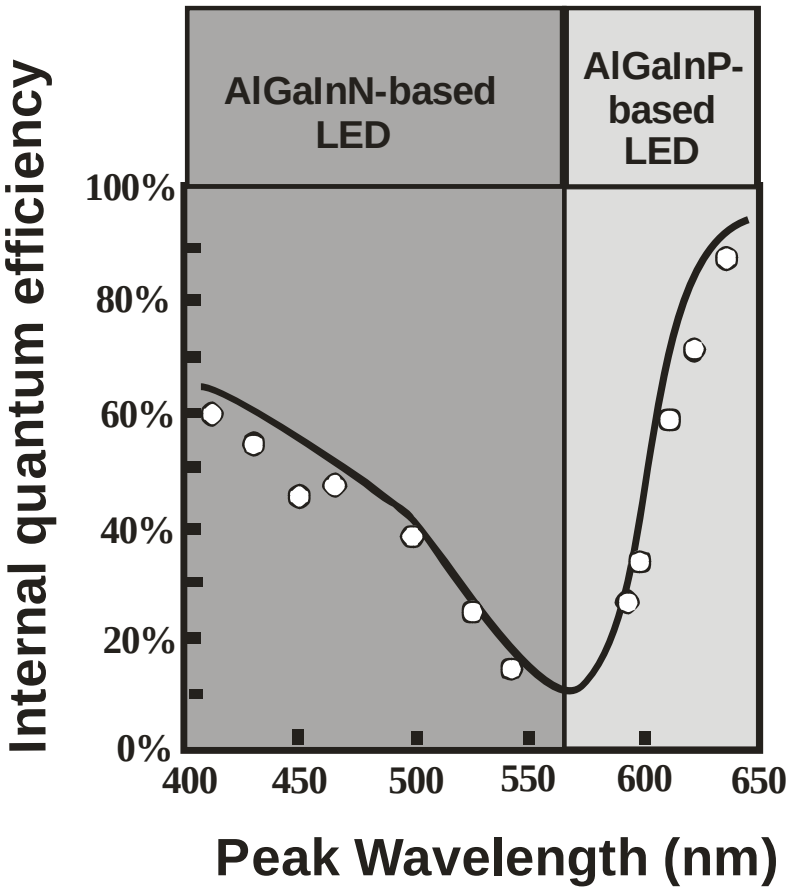

Figure 1.3. State-of-the-art LED internal quantum efficiency versus the wavelength (adopted from Paul S. Martin, Lumileds, IEEE Santa Clara, 2003).

Nowadays AlInGaP grown on GaAs substrates is the primary material for commercial production of yellow-red light emitting diodes. The AlInGaP material system was first developed in Japan for visible lasers[22,23,24,25]. Efforts started with AlInGaP/GaInP double heterostructure lasers using $Ga_{0.5}In_{0.5}P$ as the active material, which is lattice-matched to GaAs substrates. The bandgap energy of lattice-matched GaInP is approximately 1.9 eV (650nm), making the material suitable for visible lasers

emitting in the red (laser pointers, digital video disk players). Subsequent to the AlInGaP laser development that occurred in the early 1980s, AlInGaP LED development started at the end of the 1980s[26,27,28]. In contrast to the AlInGaP laser structures, LED structures typically employ current-spreading layers so that the entire p-n junction plane of the LED chip lights up and not just the region below the top ohmic contact. Further improvements were achieved by using multiple quantum well (MQW) active regions[29], coherently strained MQW active regions[30,31], distributed Bragg reflectors[32], and transparent GaP substrate technology[33]. Comprehensive reviews of the AlInGaP material system[34,35,36] can be found in references 25, 26, and 27.

The addition of Al to the GaInP active region allows one to obtain shorter emission wavelengths including the orange and yellow spectral region. However, $(Al_xGa_{1-x})_{0.5}In_{0.5}P$ becomes an indirect bandgap semiconductor at an Al compositions of $x \approx 0.53$, so the internal quantum efficiency decreases when going into shorter wavelengths, as illustrated in Fig. 1.3. There are several other problems with AlInGaP-based LEDs. First, small (<75 meV) conduction band-offsets[37] of LEDs emitting at wavelengths shorter than 610 nm result in poor temperature stability of the device. A second problem is the complicated and high-cost procedure of removing the light-absorbing GaAs substrate and wafer-bonding a transparent GaP substrate or a reflective layer on a carrier[38].

A summary of the current status of the blue, green and red LED technologies is presented in Figures 1.4, 1.5, 1.6, and 1.7[39]. Optical emission spectra of red AlInGaP-based and green and blue GaInN-based LEDs are shown in Fig. 1.4. Green LEDs have a

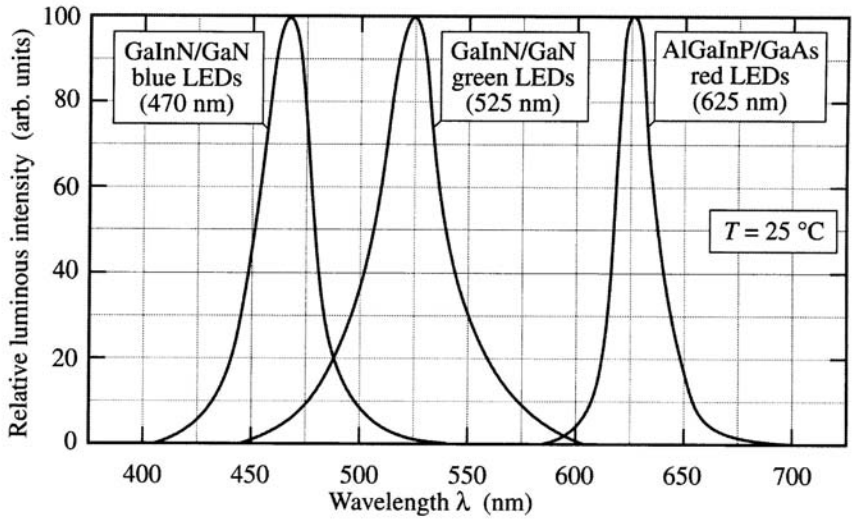

Figure 1.4. Typical emission spectrum of InGaN/GaN blue, InGaN/GaN green, and AlInGaP/GaAs red LEDs at room temperature (after Toyoda Gosei Corp., 2000).

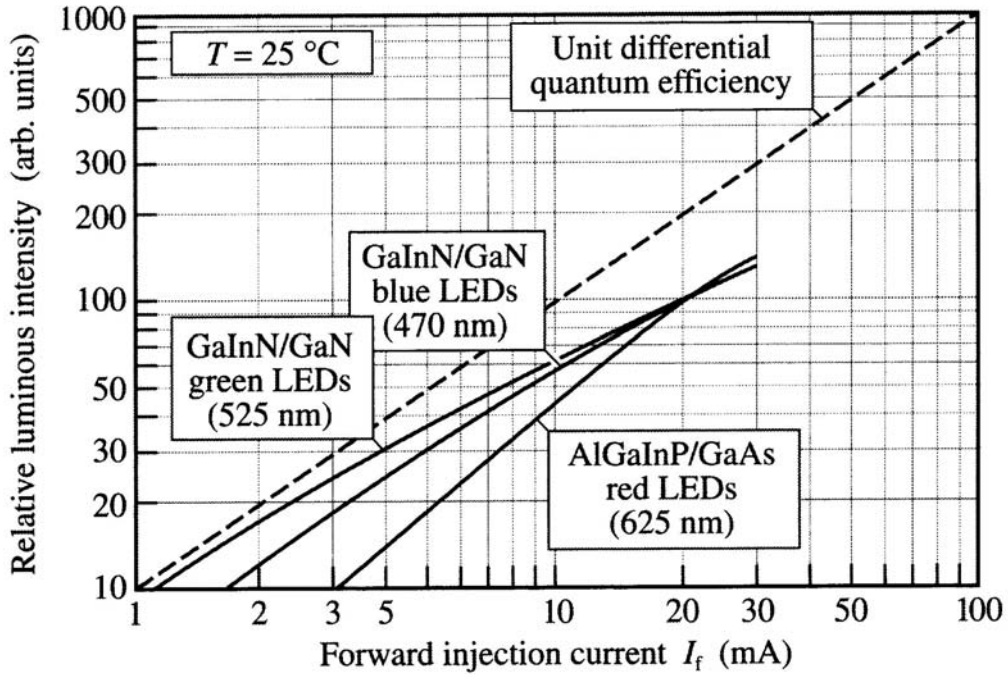

Figure 1.5. Typical light output power versus injection current of InGaN/GaN blue, InGaN/GaN green, and AlInGaP/GaAs red LEDs at room temperature (after Toyoda Gosei Corp., 2000).

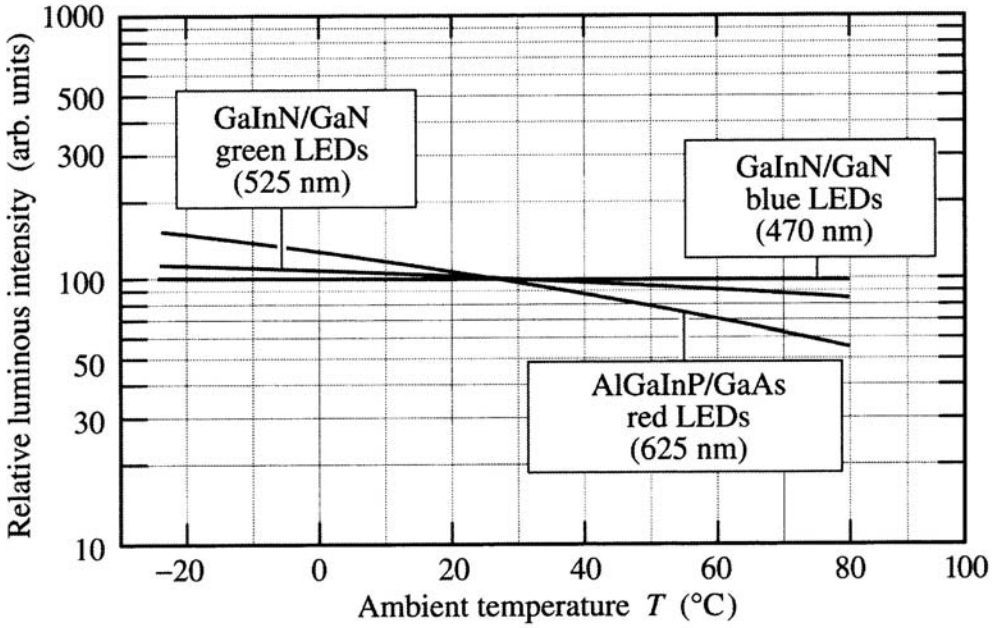

Figure 1.6. Typical output intensity of InGaN/GaN blue, InGaN/GaN green, and AlInGaP/GaAs red LEDs versus ambient temperature (after Toyoda Gosei Corp., 2000).

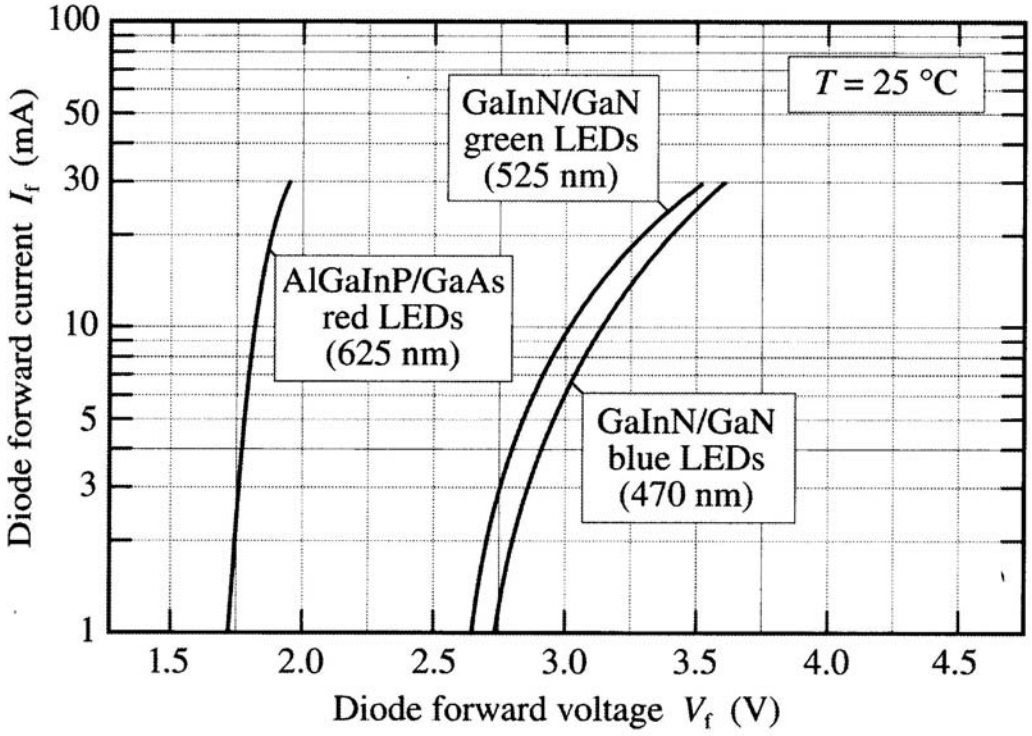

Figure 1.7. Typical forward current-voltage (I-V) characteristic of InGaN/GaN blue, InGaN/GaN green, and AlInGaP/GaAs red LEDs at room temperature (after Toyoda Gosei Corp., 2000).

noticeably wider emission spectrum than either blue or red LEDs. This is due to the formation of In-rich clusters during the growth of InGaN. Formation of such In-rich clusters depends strongly on the growth conditions. The light output vs. injection current is shown in Fig. 1.5. The unity-slope line, which corresponds to an ideal LED with unity differential quantum efficiency, is shown by the dashed line. The mature AlInGaP LED closely follows the unity-slope line. However, the green LED has a large deviation from unity differential quantum efficiency slope because of the lower maturity of the InGaN material system, especially with high concentrations of In. The temperature dependence of the optical emission intensity is shown in Fig. 1.6. This figure reveals that III-V nitride diodes have a much weaker temperature dependence than AlInGaP-based LEDs. This is an illustration of the previously mentioned poor temperature stability of AlInGaP-based LEDs. This is one of the main obstacles for utilizing AlInGaP red LEDs for white LEDs in RGB approach. Ultra bright white LEDs require operation at high currents (>100mA), which results in the heating of the LED chip and a decrease of its luminous performance. Another obstacle for adopting RGB approach is its higher cost as compared to UV + yellow phosphorus approach.

The forward current-voltage characteristics of a blue InGaN, a green InGaN, and a red AlInGaP LED are shown in Fig. 1.7. The turn-on voltage scales with the emission energy, indicating a well-behaved characteristic. The diode series resistance can be extracted from the slope of the I-V characteristics. The blue and green diodes have a higher series resistance than the red AInGaP diode. The larger resistance in InGaN LEDs can be attributed to several factors including the “lateral” resistance in n-type buffer layer

for devices grown on sapphire substrates, strong polarization effects occurring in the nitride material family, lower p-type conductivity in the cladding layer, and higher p-type contact resistance. The lower p-type conductivity is due to the high acceptor activation energy (~200 meV) in GaN and InGaN so that only a small fraction of acceptors is activated.

Thus, despite the relative maturity of both technologies, some problems still exist. We are mainly concerned about the problems with AlInGaP-based yellow-red LEDs, since we are addressing this spectral region in our work. The summarized problems are: poor temperature stability, decrease of the quantum efficiency in the 650- 580 nm range, and use of an absorbing GaAs substrate for the initial AlInGaP growth.

1.2.2. Dilute nitrides

The new class of materials, dilute nitrides, captured much attention of the scientific community in the early 90s. Incorporation of a small amount (<5%) of nitrogen into GaAs was initially investigated. Several theoretical issues have been addressed, including phase stability of GaNAs alloys[40] and N solubility in GaNAs[41,42,43]. The interest to GaNAs alloys was due to their possible applications in 1.3-1.55 μm lasers for optical fiber communications, since adding a small amount of nitrogen (~3.5%) into GaAs results in bandgap reduction[44,45] of about 300 meV. Early theoretical studies projected bandgap bowings based primarily on calculations for large N fractions[46,47,48,49,50,51,52,53]. The first attempts to explain this unusual behavior were based on a dielectric model that predicted highly nonlinear composition dependency of the bandgap for alloys of dilute

nitride semiconductor compounds[54]. Several other theoretical explanations of the large bandgap reduction in III-V-N alloys have been proposed[55,56,57,58]. Recently, it has been demonstrated that the band anticrossing (BAC) model, in which localized N states interact with the extended states of the conduction band, can explain the unusual properties of III-V-N alloys[59].

For experimental studies, different growth techniques and nitrogen sources were used to grow GaNAs alloy. Weyers *et al.*[60,61] reported 1.6% in GaN_xAs_{1-x} using metalorganic chemical vapor deposition (MOCVD) and NH_3 cracked in a microwave plasma as the N source. Bharatan *et al*.[62] attempted to grow GaN_xAs_{1-x} on GaAs and GaP using electron cyclotron resonance metalorganic MBE (MOMBE), but only polycrystalline films were obtained. Kondow *et al.* also reported 1.5% N incorporation in GaAs using gas-source molecular beam epitaxy (GSMBE) and RF plasma N radical beam source[63,64].

For device applications, Kondow *et al.* fabricated the first current-injection $In_{0.3}Ga_{0.7}N_{0.004}As_{0.0996}$/GaAs quantum well laser grown by GSMBE with continuous – wave lasing near 1.18 μm[65]. A laser operating near 1.3 μm under RT pulse operation using a GaInNAs active layer grown by MOCVD was realized by Sato *et al*.[66]. Egorov et al.[67] reported high-power CW operation of InGaNAs lasers at 1.3 μm, grown by solid source MBE with a RF plasma source. To date, the optical and structural properties of the InGaNAs material grown on GaAs, as well as its application for long wavelength (1.3-1.55 μm) optoelectronic devices are well studied. This is not the case for (In, Al)GaNP material system grown on GaP substrates.

Incorporation of N into GaP was studied back in 1965[68]. It is well known that at very low concentrations (~ 10^{16} cm^{-3}), an isolated N introduces a highly localized state in GaP, where the energy level is located slightly below the conduction band minimum. Such a spatial localization leads to quasi-direct transitions in GaP:N, which made GaP:N a widely used material for green LEDs, even though GaP has an indirect bandgap[69]. With slightly increased N concentrations, N forms NN_i pairs, which shift light emission wavelength from green to yellow[70,71]. The effect of nitrogen doping of $In_xGa_{1-x}P$ [72] and $GaAs_xP_{1-x}$[73] was also studied in the early 70s.

For GaNP alloys, theoretical studies indicate that difficulties arise in synthesizing GaNP alloys as a result of the large differences in lattice structure (GaN: wurtzite and GaP: zincblende) and a lattice constant (~20%) between GaN and GaP. Using the delta lattice parameter (DLP) model[43] based on the concept that the bonding in alloys is determined largely by the energy of the electrons, Stringfellow predicted a miscibility gap in GaNP at 700^0C [74]. This miscibility gap would be the main obstacle preventing the successful growth of this material.

Different growth techniques have been utilized to grow GaNP. For example, Li *et al.*[75] achieved 0.08% of N in GaN_xP_{1-x} using chemical beam epitaxy with co-injected tertiarybutylphosphine (TBP) and ammonia (NH_3). Miyoshi *et al.*[76,77,78,79] obtained 4% of N in GaN_xP_{1-x} using MOVPE with DMHy as the N source, while Baillargeon *et al.*[80,81] reported up to 7.6% of N incorporation in GaP grown by MBE using dissociated NH_3 as the N source. Finally, as high as 16% N concentration in GaN_xP_{1-x} without any phase

separation has been obtained by Bi and Tu[82], but the epilayers were completely relaxed due to large strain.

As far as the composition dependence of the bandgap energy of this alloy is concerned, Sakai *et al.*[47] and Baillargeon *et al.*[80], using Van Vechten's model[83,84], predicted a negative bandgap energy region, while Miyoshi *et al.*[85], using a semi-empirical tight-binding calculation of the electronic structure of II-V semiconductors developed by Vogl *et al.*[86], found that no semimetallic region exists. The data of Baillargeon *et al.*[81] show that the bandgap energy of GaN_xP_{1-x} follows the prediction based on Van Vechten's model with N concentrations less than 4% [83,84]. Bi and Tu's results[82] show that although a large bandgap bowing is expected, the material is still a semiconductor up to 16% of N, rather that semimetal, in agreement with predictions by Miyoshi *et al.*[85], contrary to the predictions of Sakai *et al.*[47] and Baillargeon *et al.*[80]. The reason is due to the fact that Van Vechten's model is based on the perturbation theory; it is valid only for bowing smaller than the average bandgap. Thus, at dilute N concentrations, the Van Vechten model predicts the trend in agreement with experiments; but at higher N concentrations, it deviates from experimental data.

All described experimental work assumed that GaNP alloys were indirect bandgap materials due to poor PL emission. Ballaiche *et al.*, however, using 512-atom supercell pseudopotential band structure calculations, predicted a transition from indirect to direct bandgap at nitrogen concentration of 3% for GaNP[87] alloys, but there has been no report on optoelectronic devices based on GaNP alloys until the year of 2000, when Xin *et al.*[88] reported red LEDs based on GaNP alloys. This work was a result of a series

of publications on GSMBE growth and characterization of GaNP material on GaP (100) substrates. The series started with a report on an experimental observation of indirect-to-direct bandgap transition of GaNP at about 0.43% of nitrogen incorporated[89]. The band anticrossing model was applied by Wu *et al*.[90] to explain this transition in GaNP. Also, band anticrossing in GaNP was analyzed by Buyanova *et al*.[91]. Photoluminescence and absorption coefficient study of GaN_xP_{1-x} bulk layers grown on GaP substrates were used by Xin and Tu to reveal experimentally the direct bandgap nature of GaN_xP_{1-x} ($x>0.43\%$). Study of the photoluminescence properties of GaNP/GaP quantum wells[92] allowed them to determine the electron effective mass in $GaN_{0.025}P_{0.975}$, which turned out to be $0.9m_e$. This large value of the electron effective mass is due to mixture of X and Γ wave functions of the conduction band in GaNP[93].

Some of the structural and optical properties of GaN_xP_{1-x} alloys grown on GaP substrates were studied by Buyanova *et al*. Raman studies were performed on GaN_xP_{1-x} bulk layers[94]. Several effects have been observed: first, frequencies of GaP-like and GaN-like longitudinal optical phonons exhibit strong compositional dependence, due to a combined effect of alloying and biaxial strain; second, a dramatic quenching of two-phonon Raman scattering and an emergence of zone-edge GaP-like vibrations were found. Compositional disorder in the alloy was proposed to be a reason for those effects to appear.

Radiative recombination mechanisms in GaN_xP_{1-x} alloys[95] as well as time-resolved photoluminescence[96] were studied by Buyanova *et al*. It was found that PL emission in GaNP with $x<4\%$ originates from the optical transitions within the N-related

localized states. Using time-resolved PL, an abrupt shortening of the radiative lifetime of the near-bandgap photoluminescence, caused by radiative recombination within N-related centers, was found to occur at about 0.5% of nitrogen, i.e., within the same range of N compositions as the appearance of the direct-bandgap-like behavior of GaNP alloy. Next, temperature dependence of GaNP bandgap was studied by Rudko *et al*.[97]. It was shown, that temperature dependence of the bandgap energy of GaNP remains close to the one of the GaP indirect gap except in the vicinity of the bandgap crossover (x~1.3%), where a significantly weaker dependence was observed. The most recent work by Buyanova et al.[98] on properties of GaNP material was devoted to low temperature photoluminescence excitation measurements. New findings included: a) a drastic change in the ratio of oscillator strengths between the optical transitions involving the conduction band (CB) minimum and the high-lying Γ CB state; b) a strong blue shift of the Γ CB state with increasing *x* accompanying a red shift of the CB minimum; c) pinning of the localized N states. The results, described in the last several paragraphs, represent current status of the investigation of GaNP alloys grown on GaP substrates.

Studying of the quaternary InGaNP material followed the initial study of the ternary GaNP alloy. Little research has been done on InGaNP grown on GaP substrates. Xin and Tu[99] reported improvement of structural and optical properties of GaNP when adding In into the alloy. Double-heterostructure red LEDs were fabricated utilizing InGaNP bulk layer as an active region. No more results have appeared to date on the InGaNP material, grown on GaP (100) substrates and devices based on it.

Hong and Tu studied the $In_xGa_{1-x}N_yP_{1-y}$ material system grown on GaAs (100) substrates. First works include X-ray and PL characterization of $In_{0.52}Ga_{0.48}N_yP_{1-y}$ grown on GaAs[100] and study of the effect of nitrogen on the optical and transport properties of $In_{0.52}Ga_{0.48}N_yP_{1-y}$/GaAs[101]. Several important results have been reported, such as: nitrogen incorporation dramatically reduces the $In_xGa_{1-x}P$ bandgap; PL peak energy exhibits an inverted S-shaped dependence with temperature; nitrogen incorporation significantly reduces the free-electron concentration and mobility; and, rapid thermal annealing at 800^0C strongly decreases the free-carrier concentration in $In_{0.52}Ga_{0.48}N_{0.005}P_{0.995}$. Further study[102] revealed similarities between $In_{0.52}Ga_{0.48}N_yP_{1-y}$ and $In_{0.08}Ga_{0.92}N_yAs_{1-y}$ grown on GaAs, such as asymmetric line shape of the PL spectra with a low-energy tail, indicating the presence of N-related localized states; and a decrease of free-carrier concentration in Si-doped $In_{0.52}Ga_{0.48}P$ and $In_{0.08}Ga_{0.92}As$ when adding nitrogen into these alloys.

Other investigation of InGaNP grown on GaAs included: band lineup between InGaNP and GaAs studied by Hong *et al.*[103], Hwang *et al.*[104], and Izadifard *et al.*[105]; grown- in defects in InGaNP studied by Vorona *et al.*[106]; formation of Ga interstitials in $(Al,In)_xGa_{1-x}N_yP_{1-y}$ and their role in carrier recombination studied by Thinh *et al*[107,108]; and hydrogen-related defects in GaNP studied by Buyanova *et al.*[109] and Polimeni *et al.*[110].

Finally, serious attention has been recently paid to the growth of GaNP on Si (100) substrates. This interest is due to lattice matching of $GaN_{0.02}P_{0.98}$ to Si (100). If this growth is successfully realized, this would fulfill a long-sought dream to integrate

mainstream Si-based electronics with III-V-based optoelectronics. Works published by Yonezu *et al*.[111] are currently a milestone in this area. Defect-free GaNP layers have been already reported[112,113,114]. Evaluation of optical and defect properties of GaNP alloys, lattice matched to Si, have been reported by Izadifard *et al*[115].

1.3. Tasks and proposed approaches

So far our knowledge on the (Al,In,Ga)NP material system is limited, despite the studies reviewed in the previous paragraphs. Little information available on the growth of the InGaNP/GaP material system and study of its optical and structural properties. No information is available on the growth of InGaNP/GaP quantum wells, their optical and structural properties, and, consequently, their device applications. Also, growth and characterization of the AlGaNP/GaP material system is not studied to date. Given the current status of research and development of the (Al,In,Ga)NP material system on GaP substrates and its device applications, as well as current stage of development of conventional yellow-red AlInGaP-based LEDs, the following tasks are to be studied in this dissertation:

1. Optimization of the growth conditions of the GaNP/GaP material system.
2. Synthesis of the AlGaNP/GaP material system and study of its structural and optical properties.
3. Synthesis of InGaNP/GaP quantum wells and study of their optical and structural properties.

4. Use of the (Al,In,Ga)NP material system as the active region of LEDs, emitting in the yellow-red spectral range.
5. Developing a fabrication process for (Al,In,Ga)NP–based LEDs.
6. Optimization of the LED structure and its growth conditions.

Synthesizing III-NP is not an easy task because of the existence of a large miscibility gap in this material. In thermodynamic equilibrium based on the entropy of mixing, the alloys composed of elements with a large difference in ionic radii tend to have a miscibility gap[116]. The ionic radii of N and P are 0.72 Å and 1.13 Å[117], respectively, so the difference of ionic radii is 36% for N and P. Therefore, a large miscibility gap in mixed group-V nitride-phosphides is expected, and materials grown within this gap would tend to phase separate rather than forming an alloy. In order to overcome this problem a non-equilibrium growth technique – gas source molecular beam epitaxy with a radio-frequency (RF) nitrogen radical beam source - will be used to incorporate nitrogen into III-P alloys. Because of the large miscibility gap expected, low temperature growth will be required and nitrogen concentrations not exceeding 3% will be used.

As for LED applications of the (Al,In,Ga)NP material system for the yellow-red spectral region, our proposed approach has a number of advantages over currently used AlInGaP-based LEDs. First, all layers of the LED structure are indirect bandgap and transparent to the emitted light. Second, the LED structure is pseudomorphically grown on a transparent GaP (100) substrate, so there is no need for substrate removal and subsequent wafer bonding to a transparent substrate or a reflective layer on a carrier,

which is the case for AlInGaP-based LEDs. Third, the active region formed using proposed material system has 2-3 times larger conduction band offsets as compared to AlInGaP-based LEDs, which should enhance the temperature stability of the device and its luminous performance.

1.4. Scope of the dissertation

The main goal of this dissertation is to investigate the optical and structural properties of the (Al,In,Ga)NP material system grown on a GaP (100) substrate, and use this new material as the active region of yellow-red LEDs. The dissertation has two main parts. In the first main part (Chapter 3) we study growth and characterization of GaNP, AlGaNP and InGaNP materials. In the second main part (Chapter 4) we use the obtained knowledge for applications of the (Al,In,Ga)NP material system in LED structures.

Chapter 2 describes the modification of our GSMBE machine to handle the growth of III-N-P nitrides. An introduction of the material and device characterization methods used in this work will be also mentioned. These methods include double-crystal x-ray diffractometry, photoluminescence, electroluminescence, LED light output using an integrating sphere, and I-V measurements using a probe station. Also, the equipment used for the LED processing will be described.

Chapter 3 is devoted to the growth and characterization of the (Al,In,Ga)NP material system. Structural properties of GaNP as dependent on the substrate temperature will be studied. The dependence of the GaNP band gap vs. nitrogen concentration and

temperature dependent PL will be analyzed. For AlGaNP layers, using thermodynamic approach we explain the difference between nitrogen incorporation into GaP and AlP. We demonstrate and explain the peculiarities of AlGaNP quaternary alloy growth: dependence of nitrogen concentration on Al composition and dependence of crystal quality on Al composition. The dependence of the emission wavelength vs. nitrogen and indium compositions will be studied for InGaNP QWs. The electron effective mass will be determined for InGaNP materials with different indium concentrations. The conduction and valence band offsets are to be calculated for the InGaNP/GaP heterojunction.

In Chapter 4, we describe LED chip fabrication and contacts optimization. *N*-type and *p*-type contacts development will be discussed. A description of LED chip processing optimization will be given for a *p*-*i*-*n* diode structure. The band offsets will be compared for (Al,In,Ga)NP-based LED structures and conventional AlInGaP-based LED structures. Growth and fabrication results for bulk GaNP-based amber LEDs will be discussed. Color stability (EL peak wavelength shift vs. current) will be compared for GaNP-based LEDs and AlInGaP-based LEDs. The influence of the In concentration in InGaNP QWs on EL properties of LED chips will be reported. Single and multiple InGaNP QW-based LEDs will be studied. Current overflow in InGaNP QWs and AlInGaP QWs will be calculated and analyzed.

Chapter 5 summarizes the dissertation, and some aspects for the future work are suggested.

Appendix A presents an alternative method to achieve yellow-red light emission from InGaP, directly grown on a transparent GaP (100) substrate. We will present initial study on metamorphic growth of InGaP layers on GaP substrates, as well as demonstrate room-temperature amber photoluminescence from InGaP QWs, grown on a metamorphic InGaP layer.

References:

[1] Fred Shubert E., Light-emitting diodes, Cambridge (2003).

[2] Miller B.I., Ripper J.E., Dyment J.C., Pinkas E., and Panish M.B., *Appl. Phys. Lett.* **18**, 403 (1971).

[3] Gooch C.H., Electroluminescent Devices, John Willey & Sons, New York (1973).

[4] Hayashi I., Panish M.B., Foy P.W., and Sumsky, *Appl. Phys. Lett*. **17**, 109 (1970).

[5] Li H., Iga K., Vertical-cavity surface-emitting laser devices, Springer (2003).

[6] Asbeck P.M., Chang M.F., Wang K.C., Miller D.L., Sullivan G.J., Sheng N.H., Sovero E., and Higgins J.A., *IEEE Trans. Electron. Dev.* **ED-34**, 2571 (1987).

[7] Nakajima O., Nagata K., Yamachi Y., Ito H., and Ishibashi T., *IEEE Trans. Electron. Dev.* **ED-34**, 2393 (1987).

[8] Whitaker T., *Compound Semicond*. **4**, 32 (1998).

[9] Yano M., Nishi H., Tukusagawa M., *J. Appl. Phys.* **52**, 3172 (1981).

[10] Craford M.G., *SPIE Proc.* **4776**, 1 (2002).

[11] *The Promise of Solid State Lighting for General Illumination: Light Emitting Diodes (LEDs) and Organic Light Emitting Diodes (OLEDs) Update 2002*, Department of Energy (BTS) and the Optoelectronics Industry Development Association.

[12] Craford M.G., Plenary talk on light-emitting diodes, MRS Fall Meeting, Boston, (1999).

[13] Akasaki I., Amano H., Itoh K., Koide N., and Manabe K., GaAs and Related Compounds conference, *Inst. Phys. Conf. Ser.* **129**, 851 (1992).

[14] Nakamura S., Senoh M., and Mukai T., *Jpn. J. Appl. Phys*. **32**, L8 (1993).

[15] Nakamura S., Senoh M., and Mukai T., *Appl. Phys. Lett.* **62**, 2390 (1993).

[16] Nakamura S., Mukai T., and Senoh M., *Appl. Phys. Lett.* **64**, 1687 (1994).

[17] Nakamura S., Senoh M., Iwasa N., Nagahama S., *Jpn. J. Appl. Phys*. **34**, L797 (1995).

[18] Nakamura S., Senoh M., Nagahama S., Iwasa N., Yamada T., Matsushita T., Sugimoto Y. and Kiyoku H., *Appl. Phys. Lett.* **69**, 4056 (1996).

[19] Nakamura S. and Fasol G., *The blue laser diode*, Springer, Berlin (1997).

[20] Guo X. Graff J.W., and Shubert E.F., *IEDM Technical Digest*, **IEDM-99**, 600 (1999).

[21] Martin P.S., "*Illumination with LEDs*", Lumileds presentation, IEEE Santa Clara, February 12th (2003).

[22] Kobayashi K., Kawata S., Gomyo A., Hino I. and Suzuki T., *Electron. Lett*. **21**, 931 (1985).

[23] Ohba Y., Ishikawa M., Sugawara H., Yamamoto T., and Nakanisi T., *J. Cryst. Growth* **77**, 374 (1986).

[24] Ikeda M., Nakano K., Mori Y., Kaneko K. and Watanabe N., *J. Cryst. Growth* **77**, 380 (1986).

[25] Itaya K., Ishikawa M., and Uematsu Y., *Electron. Lett*. **26**, 839 (1990).

[26] Kuo C.P., Fletcher R.M. Osentowski T.D., Lardizabel M.C., Craford M.G., and Robbins V.M., *Appl. Phys. Lett.* **57**, 2937 (1990).

[27] Fletcher R.M., Kuo C.P., Osentowski T.D., and Robbins V.M., US patent 5,008,718 (1991).

[28] Sugawara H., Ishikawa M., Kokubun Y., Nishikawa Y., and Naritsuka S., US patent 5,048,035 (1991).

[29] Huang K.-H. and Chen T.-P., US patent 5,661,742 (1997).

[30] Chang S.J. and Chang C.S., *IEEE Photonics Technol. Lett*. **10**, 772 (1998).

[31] Chang S.J. and Chang C.S., *Jpn. J. Appl. Phys*. **37**, L653 (1998).

[32] Chang S.J. and Chang C.S., Su Y.K., Chang P.T. Wu Y.R., Huang K.H and Chen T.P., *IEE Proceedings-Optoelectronics* **144**, 1 (1997).

[33] Kish F.A. and Fletcher R.M., *Semiconductors and Semimetals* **48**, 149(1997).

[34] Stringfellow G.B. and Craford M.G (Editors), *Semiconductors and Semimetals* **48**, (1997).

[35] Mueller G. (Editor), *Semiconductors and Semimetals* **64**, (2000).

[36] Krames M.R., Amano H., Brown J.J., and Heremans P.L., Special issue of *IEEE J. Select. Top. Quant. Electronics* **8**, 185 (2002).

[37] Patel D., Pikal J.M., Menoni C.S., Thomas K.J., Kish F. A., and Hueschen M.R., *Appl. Phys. Lett*. **75**, 3201 (1999).

[38] F. A. Kish, F. M. Steranka, D. C. DeFevere, D. A. Vanderwater, K. G. Park, C. P. Kuo, T. D. Osentowski, M. J. Peanasky, J. G. Yu, D. A. Steigerwald, M. G. Craford, V. M. Robbins, *Appl. Phys. Lett*. **64**, 2839 (1994).

[39] Toyoda Gosei Corporation, Japan, LED product catalogue (2000).

[40] Neugebauer J., Van de Walle C.G., *Phys .Rev. B* **51**, 10568 (1995).

[41] Kao Y.C., Broekaet T.P.E., Liu H.Y., Tang S., Ho I.H., Stringfellow G.B., *Mater. Res. Soc. Symp. Proc.* **423**, 335 (1996).

[42] Stringfellow G.B. and Hom G., *J. Electrochem. Soc.* **124**, 1806 (1997).

[43] Ilegems M. and Panish M.B., *J. Phys. Chem. Solids* **35**, 409 (1974).

[44] Dutta N.K. and Nelson R.J., *Appl. Phys. Lett*. **38**, 407 (1981).

[45] Egorov A.Yu., Semenova E.S., Ustinov V.M., Hong Y.G., and Tu C.W., *Semiconductors* **36**, 981 (2002).

[46] Bellaiche L and Zunger A., *Phys. Rev.* B **57**, 4425 (1998).

[47] Sakai S., Ueta Y., and Terauchi Y., *Jpn. J. Appl. Phys*. **32**, 4413 (1993).

[48] Wei S.-H. and Zunger A., *Phys. Rev. Lett.* **76**, 664 (1996).

[49] Rubio A. and Cohen M.L., *Phys. Rev.* **B** 51, 4343 (1995).

[50] Ballaiche L., Wei S.-H., and Zunger A., *Phys. Rev.* B **54**, 17568 (1996).

[51] Ballaiche L., Wei S.-H., and Zunger A., *Appl. Phys. Lett.* **70**, 3558 (1997).

[52] Mattila T., Wei S.-H., and Zunger A., *Phys. Rev.* B **60**, 11245 (1999).

[53] Ballaiche L., Wei S.-H., and Zunger A., *Phys. Rev.* B **56**, 10233 (1997).

[54] Van Vechten J.A. and Bergstresser T.K., *Phys. Rev.* B **1**, 3351 (1970).

[55] Jones E.D., Modine N.A., Allerman A.A., Kurtz S.R., Wright A.F., Tozer S.T., and Wei X., *Phys. Rev.* **B** 60, 4430 (1999).

[56] Wang L.-W., *Appl. Phys. Lett.* **78**, 1565 (2001).

[57] Al-Yacoub A., Bellaiche L., *Phys. Rev.* B **62**, 10847 (2000).

[58] Zhang Y., Mascarenhas, Xin H.P., and Tu C.W., *Phys. Rev.* B **63**, 16130 (2001).

[59] Shan W., Walukiewicz W., Ager III J.W., Haller E.E., Geisz J.F., Friedman D.J., Olson J.M., and Kurtz S.R., *Phys. Rev. Lett.* **82**, 1221 (1999).

[60] Weyers M., Sato M., and Ando H., *Jpn. J. Appl. Phys*. **31**, L853 (1992).

[61] Weyers M. and Sato M., *Appl. Phys. Lett*. **62**, 1396 (1993).

[62] Bharatan S., Jones K.S., Abernathy C.R., Pearton S.J., Ren F. Wisk P.W., and Lothian J.R., *J. Vac. Sci. Technol.* A **12**, 1094 (1994).

[63] Kondow M., Uomi K., Hosomi K., Mozume T., 8th Int. MBE Conf., Paper A 11-2, Osaka, Japan August 29-September 2 (1994).

[64] Kondow M., Uomi K., Kitatani T., Watahiki S., and Yazawa Y., *J. Cryst. Growth* **164**, 175 (1996).

[65] Kondow M., Nakahara K., Kitatani T., Yazawa Y., and Uomi K., *Electron. Lett.* **32**, 2244 (1996).

[66] Sato S., Osawa Y., Saitoh T., and Fujimura I., *Electron. Lett.* **33**, 1386 (1997).

[67] Egorov A.Y., Bernklau D., Livshits D., Ustinov V., Alfereov Z.I., and Riechert H., *Electron. Lett.* **35**, 1643 (1999).

[68] Thomas D.G., Hopfield J.J., and Frosch C.J., *Phys. Rev. Lett*. **15**, 857 (1965).

[69] Bergh A.A. and Dean P.J, *Proceedings of IEEE* **60**, 156 (1972).

[70] Logan R.A., White H.G., and Wiegman W., *Appl. Phys. Lett.* **13**, 139 (1968).

[71] Groves W.O., Herzog A.H., and Craford M.G., *Appl. Phys. Lett.* **19**, 184 (1971).

[72] Macksey H.M., Holonyak Jr. N., Dupuis R.D., Campbell J.C., and Zack G.W., *J. Appl. Phys.* **44**, 1333 (1973).

[73] Holonyak Jr. N., Scifres D.R., Burnham R.D., Craford M.G., Groves W.O., Herzog A.H., *Appl. Phys. Lett.* **19**, 254 (1971).

[74] Stringfellow G.B., *J. Cryst. Growth* **27**, 21 (1974).

[75] Li N.Y., Wong W.S., Tomich D.H., Dong H.K., and Tu C.W., *J. Cryst. Growth* **164**, 180 (1996).

[76] Miyoshi S., Yaguchi H., Onabe K., and Ito R., *Appl. Phys. Lett*. **63**, 3506 (1993).

[77] Miyoshi S., Yaguchi H., Onabe K., Ito R., and Shiraki Y., *Inst. Phys. Conf. Ser.* No **136**, 637 (1993).

[78] Miyoshi S., Yaguchi H., Onabe K., Ito R., and Shiraki Y., *J. Cryst. Growth* **145**, 87 (1994).

[79] Miyoshi S., Yaguchi H., Onabe K., Shiraki Y., and Ito R., *Inst. Phys. Conf. Ser.* No **141**, 97 (1995).

[80] Baillargeon J.N., Pearah P.J., Cheng K.Y., Holfler G.E., and Hsieh K.C., *J. Vac. Sci. Technol. B* **10**, 829 (1992).

[81] Baillargeon J.N., Cheng K.Y., Holfler G.E., Pearah P.J., and Hsieh K.C., *Appl. Phys. Lett.* **60**, 2540 (1992).

[82] Bi W.G. and Tu C.W., *Appl. Phys. Lett.* **69**, 3710 (1996).

[83] Van Vechten J.A., *Phys. Rev.* **182**, 891 (1969).

[84] Van Vechten J.A., *Phys. Rev.* **187**, 1007 (1969).

[85] Miyoshi S. and Onabe K., *Topical Workshop on Nitride*, 1 (1995).

[86] Vogl P., Hjalmarson H.P., and Dow J.D., *J. Phys. Chem Solids* **44**, 365 (1983).

[87] Bellaiche L., Wei S.H., and Zunger A., *Phys. Rev. B* **56**, 10233 (1997).

[88] Xin H.P., Welty R.J., Tu C.W., *Appl. Phys. Lett*. **77**, 1946 (2000).

[89] Xin H.P., Tu C.W., Zhang Y., Mascarenhas A., *Appl. Phys. Lett.* **76**, 1267 (2000).

[90] Wu J., Walukiewicz W., Yu K.M., Ager III J.W., Haller E.E., Hong Y.G., Xin H.P., Tu C.W., Phys. Rev. B 65, 241303 (2002).

[91] I.A. Buyanova, M. Izadifard, A. Kasic, H. Arwin, W.M. Chen, H.P. Xin, Y.G. Hong and C.W. Tu, *Phys. Rev.* B **70**, 085209 (2004).

[92] Xin H.P. and Tu C.W., *Appl. Phys. Lett.* **77,** 2180 (2000).

[93] Shan W., Walukiewicz W., Yu K.M., Wu J., Ager III J.W., Haller E.E., Xin H.P., Tu C.W., *Appl. Phys. Lett*. **76**, 3251 (2000).

[94] Buyanova I.A., Chen W.M., Goldys E.M., Xin H.P., and Tu C.W., *Appl. Phys. Lett*. **78**, 3959 (2001).

[95] Buyanova I.A., Rudko G.Yu., Chen W.M., Xin H.P., Tu C.W., *Appl. Phys. Lett.* **80**, 1740 (2002).

[96] Buyanova I.A., Pozina G., Bergman J.P., Chen W.M., Xin H.P., Tu C.W., *Appl. Phys. Lett.* **81**, 52 (2002).

[97] Rudko G.Yu., Buyanova I.A., Chen W.M., Xin H.P., and Tu C.W., *Appl. Phys. Lett.* **81**, 3984 (2002).

[98] Buyanova I.A., Izadifard M., Chen W.M., Xin H.P., and Tu C.W., *Phys. Rev.* B **69**, 201303 (2004).

[99] Xin H.P., Welty R.J., Hong Y.G., Tu, C.W., *J. Crys. Growth* **227-228**, 558 (2001).

[100] Hong Y.G., Juang F.S., Kim M.H., Tu C.W., *J. Crys. Growth* **251**, 437 (2003).

[101] Hong Y.G., Nishikawa A., Tu C.W., *Appl. Phys. Lett.* **83**, 5446 (2003).

[102] Hong Y.G., Nishikawa A., Tu C.W., *J. Vac. Sci. Technol*. B **22**, 1495 (2004).

[103] Hong Y.G., Andre R., Tu C.W., *J. Vac. Sci. Technol*. B **19**, 1413 (2001).

[104] Hwang J.S., Lin K.I., Lin H.C., Hsu S.H., Chen K.C., Lu Y.T., Hong Y.G., and Tu C.W., *Appl. Phys. Lett.* **86**, 061103 (2005).

[105] Izadifard M., Mtchedlidze T., Vorona I., Chen W.M., Buyanova I.A., Hong Y.G., and Tu C.W., *Appl. Phys. Lett.* **86**, 261904 (2005).

[106] Vorona I.P., Mchedlidze T., Izadifard M., Buyanova I.A., Chen W.M., Hong Y.G., Xin H.P., and Tu C.W., *Appl. Phys. Lett.* **86**, 222110 (2005).

[107] Thinh N.Q., Vorona I.P., Izadifard M., Buyanova I.A., Chen W.M., Hong Y.G., Xin H.P., and Tu C.W., *Appl. Phys. Lett.* **85**, 2827 (2004).

[108] Thinh N.Q., Vorona I.P., Buyanova I.A., Chen W.M., Limpijumnong S., Zhang S.B., Hong Y.G., Xin H.P., Tu C.W., Utsumi A., Furukawa Y., Moon S., Wakahara A., and Yonezu H.; *Phys. Rev.* B **70**, 121201 (2004).

[109] Buyanova I.A., Izadifard M., Ivanov I.G., Birch J., Chen W.M., Felici M., Polimeni A., Capizzi M., Hong Y.G., Xin H. P.and Tu C.W., *Phys. Rev.* B **70**, 245215 (2004).

[110] Polimeni A., Masia F., Felici M., Baldassari Hoger von Hogersthal G., Bissiri M., Frova A., Capizzi M., Klar P.J., Stolz W., Buyanova I.A., Chen W.M., Xin H.P., Tu C.W., *Physica* B **340-342**, 371 (2003).

[111] Yonezu H., *Semicond. Sci. Technol.* **17**, 762 (2002).

[112] Furukawa Y., Yonezu H., Ojima K., Samonji K., Fujimoto Y., Momose K., and Aiki K., *Jpn. J. Appl. Phys.***41**, 528 (2002).

[113] Momose K., Yonezu H., Fujimoto Y., Furukawa Y., Motomura Y., and Aiki K., *Appl. Phys. Lett.* **79**, 4151 (2001).

[114] Fujimoto Y., Yonezu H., Utsumi A., Momose K., and Furukawa Y., *Appl. Phys. Lett.* **79**, 1306 (2001).

[115] Izadifard M., Bergman J.P., Vorona I., Chen W.M., Byuanova I.A., Utsumi A., Furukawa Y., Moon S., Wakahara A., and Yonezu H., *Appl. Phys Lett.* **85**, 6347 (2004).

[116] Ferreira L.G., Wei S.W., and Zunger A., Phys. Rev. B 40, 3197 (1989).

[117] Phillips J.C., Bonds and Bands in Semiconductors, Academic Press, New York (1973).

Chapter 2. Experimental techniques.

2.1. Overview

Molecular beam epitaxy (MBE) has been widely used for growing high-quality semiconductor films for different applications as well as for fundamental studies. MBE is an advanced ultra-high vacuum evaporation technique, which uses atomic or molecular beams for growth of high-purity semiconductor thin films. The high-vacuum environment allows the use of in-situ monitoring techniques, such as reflection high-energy electron diffraction (RHEED). The oscillations of the intensity of RHEED patterns are used to determine the growth rate of the semiconductor film as well as layer composition[1]. For III-V compound semiconductors MBE uses elemental sources, such as Ga, Al, In, As_4, and P_4. Typical dopants used for arsenides (e.g., GaAs) and phosphides (e.g., InP) are Si for *n*-type films and Be for *p*-type films. Gas source molecular beam epitaxy (GSMBE) was introduced in 1980. Using of thermally cracked arsine and phosphine allowed better composition control of mixed group-V compounds, such as InGaAsP[2].

All the epitaxial structures described in this thesis were grown by GSMBE. A Radio-Frequency (RF) nitrogen plasma source was used for N incorporation. This is the most commonly used type of nitrogen plasma source. It provides stable atomic nitrogen flux with good uniformity.

Chapter 2 is devoted to a description of the GSMBE system, used for growth, and several techniques used for material characterization, such as photoluminescence and high-resolution x-ray diffraction rocking curves (XRCs). Also, light-emitting diode processing techniques, such as e-beam evaporation, thermal evaporation, photolithography, wire-bonding, rapid thermal annealing (RTA) are discussed. Finally, LED chip characterization techniques, such as electroluminescence (EL) and current-voltage characteristics are described.

2.2. GSMBE growth system with a nitrogen plasma source

A Varian GEN-II MBE system was upgraded to handle group-V hydride gases. A schematic of the GSMBE system is shown in Fig. 2.1. Two separate gas cabinets for AsH_3 (100%) and PH_3 (100%) were installed together with potassium permanganate ($KMnO_4$) scrubbers. Gases are introduced into the growth chamber through two cracking furnaces heated to 980^0C, which crack arsine and phosphine into dimmers and hydrogen before reaching the substrate. Although the GSMBE system is equipped with two group-V precursors, this thesis studies only phosphide materials. Besides the two gas crackers, there are five other sources for solid Al, Ga, In, Si and Be in the growth chamber. The group-III fluxes (Ga, Al, and In) and dopant sources (Si and Be) are controlled by the temperature of effusion cells, and the fluxes of the group-V sources (As, P) are controlled by mass flow controllers (MFCs). For instance, the phosphine MFC allows a maximum

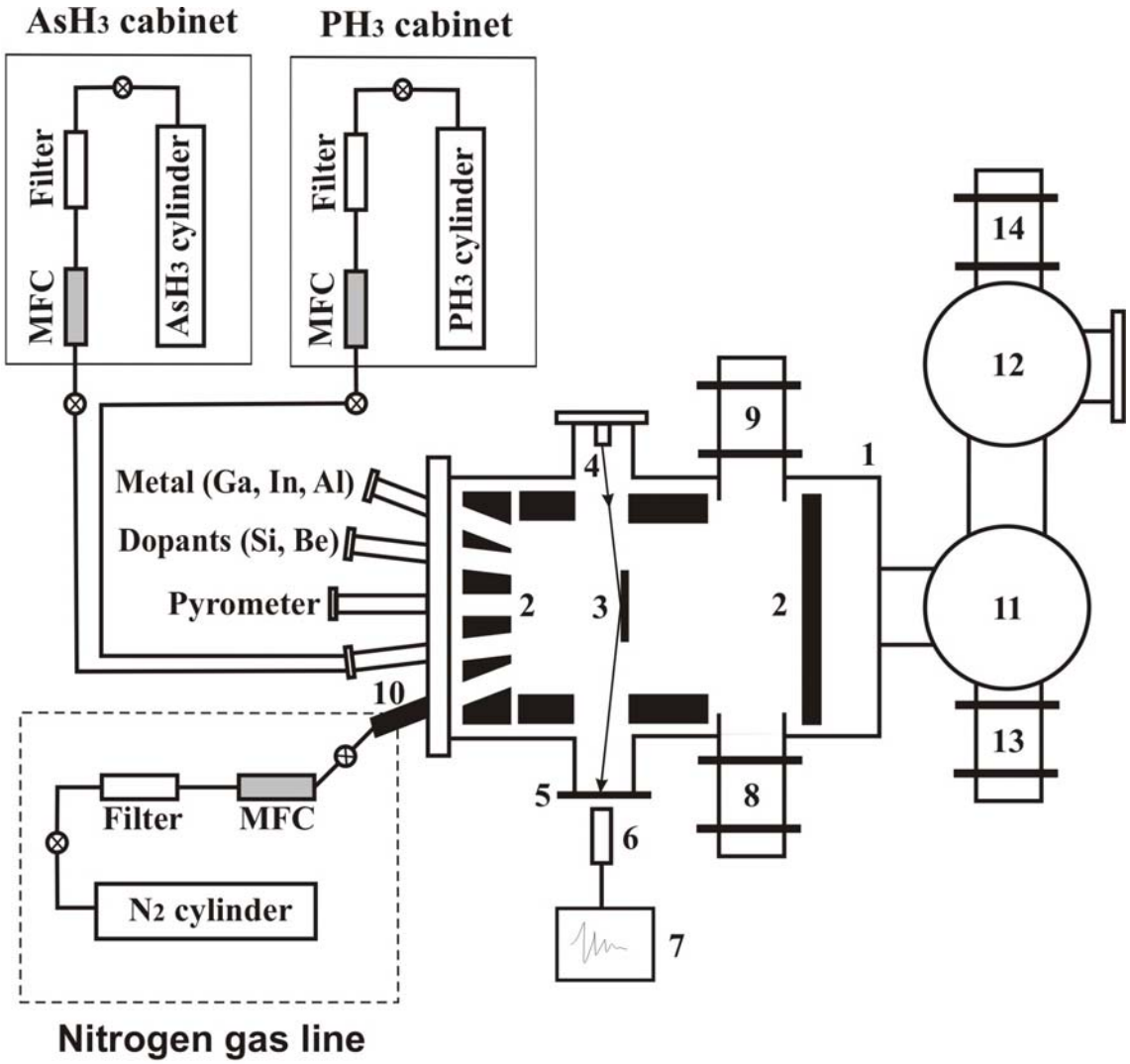

Figure 2.1. Schematic of the modified Varian GEN II Gas-Source Molecular Beam Epitaxy system.

flux of 20 sccm, and the precision of the flux value control is 0.1%, i.e. 0.02 sccm. The typical phosphine flux used during growth is about 4 sccm. All furnaces are equipped in the front with pneumatic shutters, which are both computer- and manually-controllable. Liquid nitrogen shrouds surround the growth chamber and sources to condense background molecules in the chamber for growth of high-purity layers. One Ebara cryopump with a pumping speed of 2200 l/s and one Pfeiffer TMU1600 model turbomolecular pump with a pumping speed of 1500 l/s are used to keep the vacuum in the growth chamber. The typical background pressure in the growth chamber with fed liquid nitrogen and sources heated to operating temperature is about $7*10^{-9}$ Torr. This is without group-V gas introduced into the growth chamber.

A RF plasma source is installed into one of the furnace ports, shown in the region surrounded by dashed lines in Fig.2.1. We use an Oxford Applied Research Model No MPD21 RF nitrogen plasma source with the following features: electrodeless to avoid contamination; UHV-compatible for operating at pressures of less than 10^{-5} Torr and a wide range of beam flux of 0-5 sccm with a step of 0.005 sccm (controlled by MFC). Ultra-high purity (99.99%) N_2 gas first goes through a regulator, which maintains a constant pressure of 50 psi, and a purifier (Matheson Gases & Equipment, 6190-V4MM Membrane Type) to remove water vapor and oxygen. Then N_2 gas goes through an MFC and, finally, the RF plasma source, where nitrogen radicals are generated and escape into the growth chamber through a beam exit aperture, which has 16 holes with a diameter of 0.3 mm.

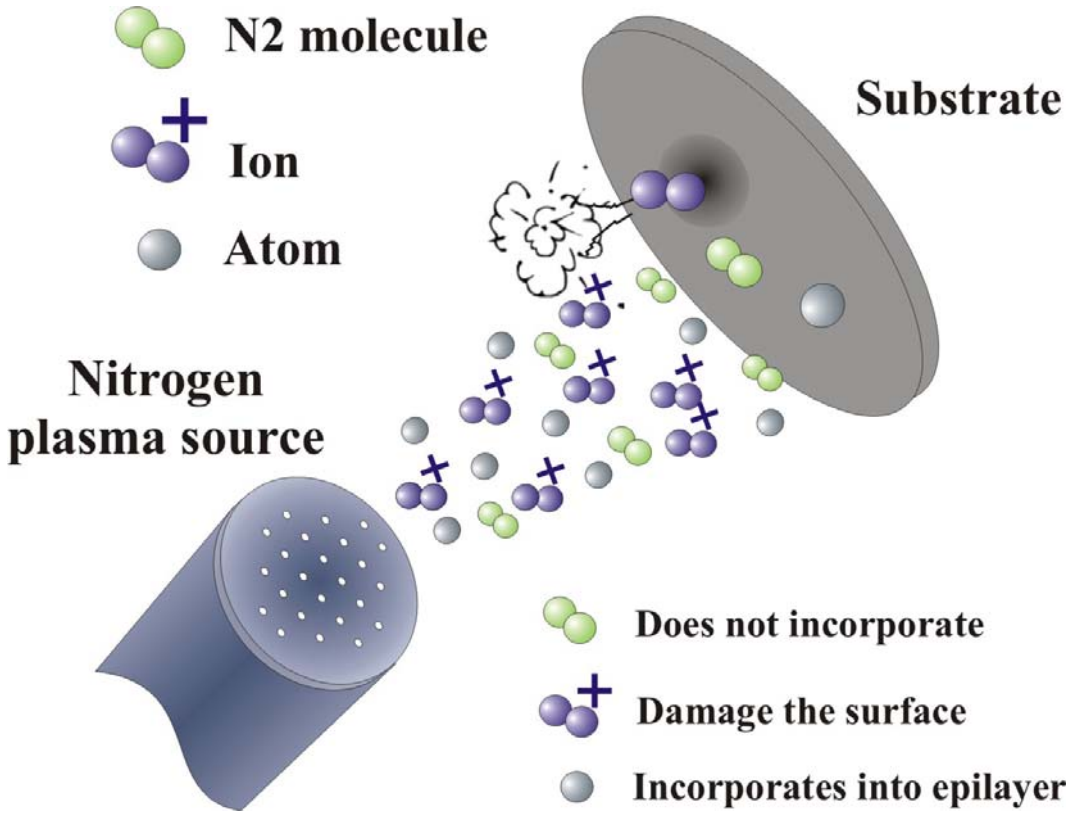

Figure 2.2. Nitrogen plasma source.

The basics of the plasma source is creation of a plasma discharge in a pyrolytic boron nitride (PBN) tube. The discharge is created from inductively-coupled RF excitation at 13.56 MHz. Nitrogen molecules are excited or break their bonds in this plasma discharge. Thus, part of the molecular nitrogen converts into atomic nitrogen in the source, but there are a number of other species (Fig.2.2) coming out of the aperture: excited molecular nitrogen, and ions, which are formed in the plasma source by impact ionizatio. Unbroken nitrogen molecules do not participate in the growth process, but nitrogen atoms incorporate into the growing film with certain efficiency. Ions may

damage the surface of the growing layer without incorporation. A shutter in front of the plasma source cuts off the nitrogen beam, when no nitride growth is required. A manual valve is installed between the MFC and the gas inlet of the RF plasma source to isolate the N_2 gas line from the growth chamber during the idle state.

The optical spectrum of our nitrogen plasma source at typical growth conditions (250 Watt, 0.5 sccm, see below in details) is shown in Fig. 2.3. The spectrum was measured using a CCD spectrometer. An optical fiber, coupled to a plasma source view port is used to deliver the optical signal into the spectrometer. The regions of the spectrum corresponding to atomic nitrogen and molecular nitrogen are show in Fig. 2.3. The intensities of the peaks corresponding to atomic nitrogen are higher than those of molecular nitrogen, showing high efficiency of the plasma source.

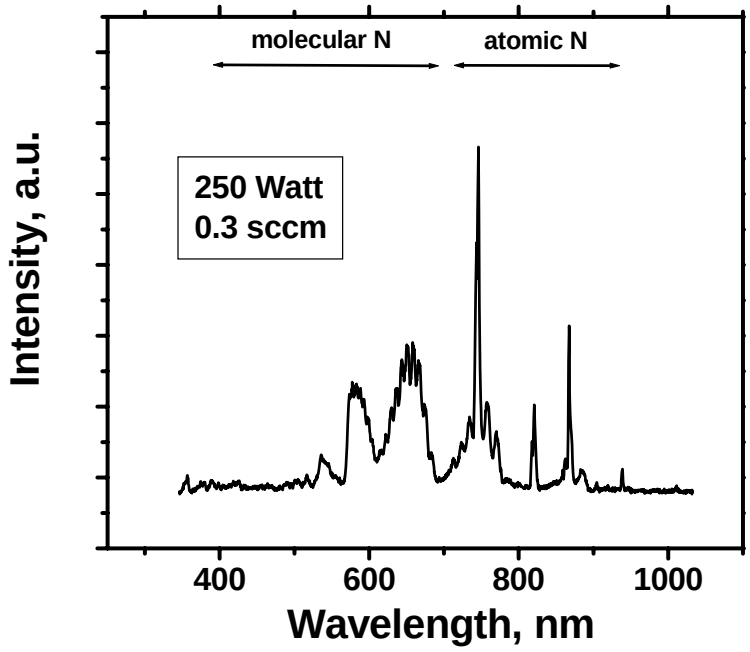

Figure 2.3. Optical emission spectrum of the nitrogen plasma source.

There are two main parameters of the plasma source – applied RF power (0-500 Watts, controlled by a plasma source power supply), and the nitrogen flux (0-3 sccm, controlled by an MFC). These parameters determine the optical emission intensity of the plasma discharge. Optical emission intensity is monitored by a Si detector. The amount of nitrogen, incorporated into the growing film, is proportional to the optical emission intensity of the nitrogen plasma source. The experimental dependence of the optical intensity of the plasma source on the source parameters is shown in Fig. 2.4. The symbols are experimental data. The family of the lines represents dependence of the plasma intensity vs. the nitrogen flux at a given applied RF power. One can see that increasing both N_2 flux and applied RF power leads to an increase of the plasma intensity, thus, an increase of the nitrogen incorporation into the growing film. The solid red line in Fig 2.4 borders the region of the graph where the plasma is intensity proportional to the nitrogen flux for all plasma values applied. The region of the graph above the solid red line shows saturation of the dependencies, which means that the efficiency of the nitrogen plasma source is lower than in the region below the solid red line.

The same plasma intensity can be achieved using higher nitrogen flux and lower RF power or lower nitrogen flux and higher RF power. The choice of the plasma source conditions for the best crystal and optical quality of the growing nitrogen-containing film is based on the next statements:

- If the applied RF power is too low (< 100 W), the plasma discharge is unstable and may switch into low-intensity mode, which is not efficient for producing reactive atomic nitrogen.

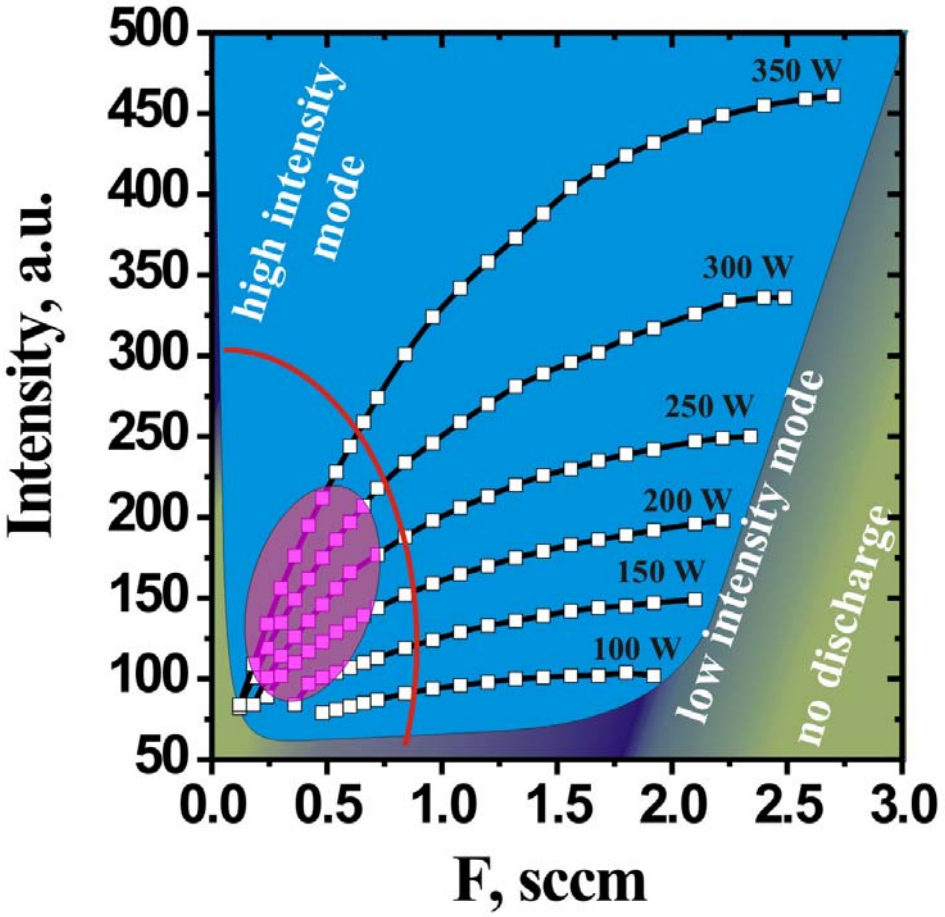

Figure 2.4. The optical intensity – nitrogen flux diagram for the nitrogen plasma

- If the applied RF power is too high (>350 W), the plasma source produces more ions, which may damage the surface.
- If the nitrogen flux is too high (above the solid red line), the dependence of the intensity vs. flux saturates, which means low efficiency of the plasma source at relatively high pressure in the growth chamber. However, we would like to have the maximum plasma source efficiency at the lowest nitrogen flux possible, to keep the

pressure low in the growth chamber and have enough atomic nitrogen to incorporate into the growing film.

- If the nitrogen flux is too low, the plasma discharge is unstable, which may lead to its attenuation.

Based on the above statements, we have determined the area in Fig 2.4 (violet color oval), which represents the best plasma source conditions for the growth of dilute nitrides with nitrogen concentrations 0.5%≤[N]≤2%. Fine-tuning of the plasma source conditions within this region is based on the evaluation of crystalline and optical properties of the samples.

2.3. Characterization

This section describes material and device (LED) characterization techniques used in this study. The material characterization techniques include photoluminescence (PL), x-ray diffraction (XRC), and Hall measurement setup. For the LED characterization we use an electroluminescence (EL) setup, a probe station for current-voltage (I-V) measurements, and an integrating sphere for light intensity measurement.

2.3.1. Material characterization

The main optical characterization technique, used in this study is photoluminescence, which is a sensitive way to characterize the optical properties of semiconductors. By observing the photon emission associated with transitions from optically excited states, the bandgap of a material can be easily determined. Figure 2.5 shows a schematic of our PL setup. An Argon ion laser, emitting at 514 nm, or a HeCd laser, emitting at 325 nm is used as the light source. A typical Ar ion laser optical output power of 100 mW and HeCd laser optical output power of 10 mW are used to excite the sample. Photoluminescence is collected in a back scattering configuration, focused into and dispersed by a 50-cm monochromator. Finally, the signal is detected at the exit of the monochromator by a photo-multiplier tube (PMT) through an amplifier. For low temperature measurement, the sample is mounted on the cold finger of a closed-cycle cryostat.

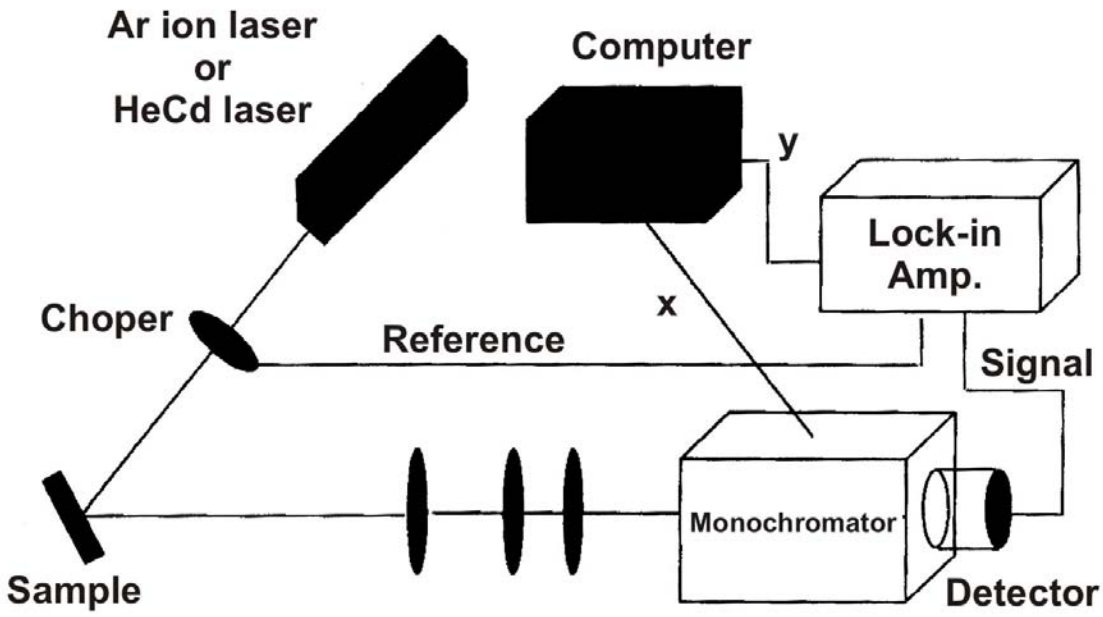

Figure 2.5. Schematic of the photoluminescence measurement system.

High-resolution X-ray diffraction is used to characterize structural properties of the samples. Cu Kα line (λ=1.5406 Å) is used in the XRC measurements. The system is presented in Fig. 2.6. The x-ray apparatus is a multiple-crystal x-ray diffractometer[3], which consists of a Phyllips PW 1729 x-ray generator, a Bartels monochromator composed of four Ge crystals set in the (+,-,-,+) configuration[4], a Philips PW 1711/10 wide-angle proportional detector and a Lansing four-way adjustable sample holder. The sample is initially mounted with the surface at the Bragg angle, θ_B, with respect to the incident beam. The detector is initially set at $2\theta_B$ to detect the (400) diffraction. During the measurements, the angular position of the sample is rocked around θ_B with the angular position of the detector fixed at $2\theta_B$. Thus, the recorded curve is called a rocking curve. The typical current and voltage used for the X-ray generator are 20-25 mA and 35 kV, respectively.

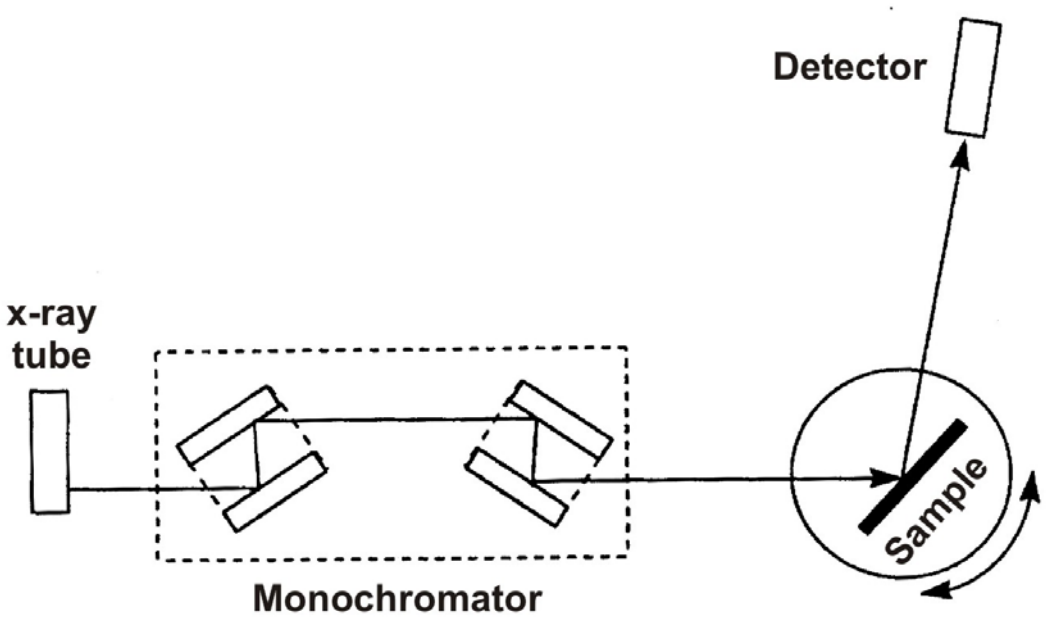

Figure 2.6. Schematic of the x-ray measurement system.

High-resolution XRCs are measured for two purposes. The first is to characterize the crystalline quality of the epilayers. In XRCs broadening of the X-ray peaks occurs for many reasons, such as inhomogeneous lattice parameters due to strain relaxation of the film, composition fluctuations, micron-tilting of lattice planes due to interfacial misfit dislocations[5,6]. Therefore, any broadening of the x-ray peak indicates quality degradation. The other purpose is to determine the layer composition and thickness. By comparing simulated curves based on the dynamic theory[7,8] with experimental data, the layer composition, thickness, crystal quality, and interfacial quality can be deduced. In order to obtain an accurate alloy composition, however, it is important to use the strain-free lattice constant of the epilayer. For a system consisting of an epilayer and a substrate, the epilayer can be fully strained, partially strained, or fully relaxed. The peak separation between the substrate and epilayer in the (400) reflection will differ by about a factor of two for for fully strained and fully relaxed epilayer.

In addition to PL and XRC, the standard Hall measurement set up is used to determine free carrier concentration and carrier mobility in the epilayers. This measurement is important to calibrate doping concentrations for light-emitting diode structures. Rectangular test samples with dimensions about 0.5 cm X 0.5 cm are used. Four indium dots are used as contacts at the corners of the sample. By measuring the resistance of the sample in between the contacts with and without an applied magnetic field, free carrier concentration and carrier mobility are determined.

2.3.2. Light-emitting diode characterization

For LED chip characterization three main techniques are used: electroluminescence, current-voltage measurement, and integrating sphere.

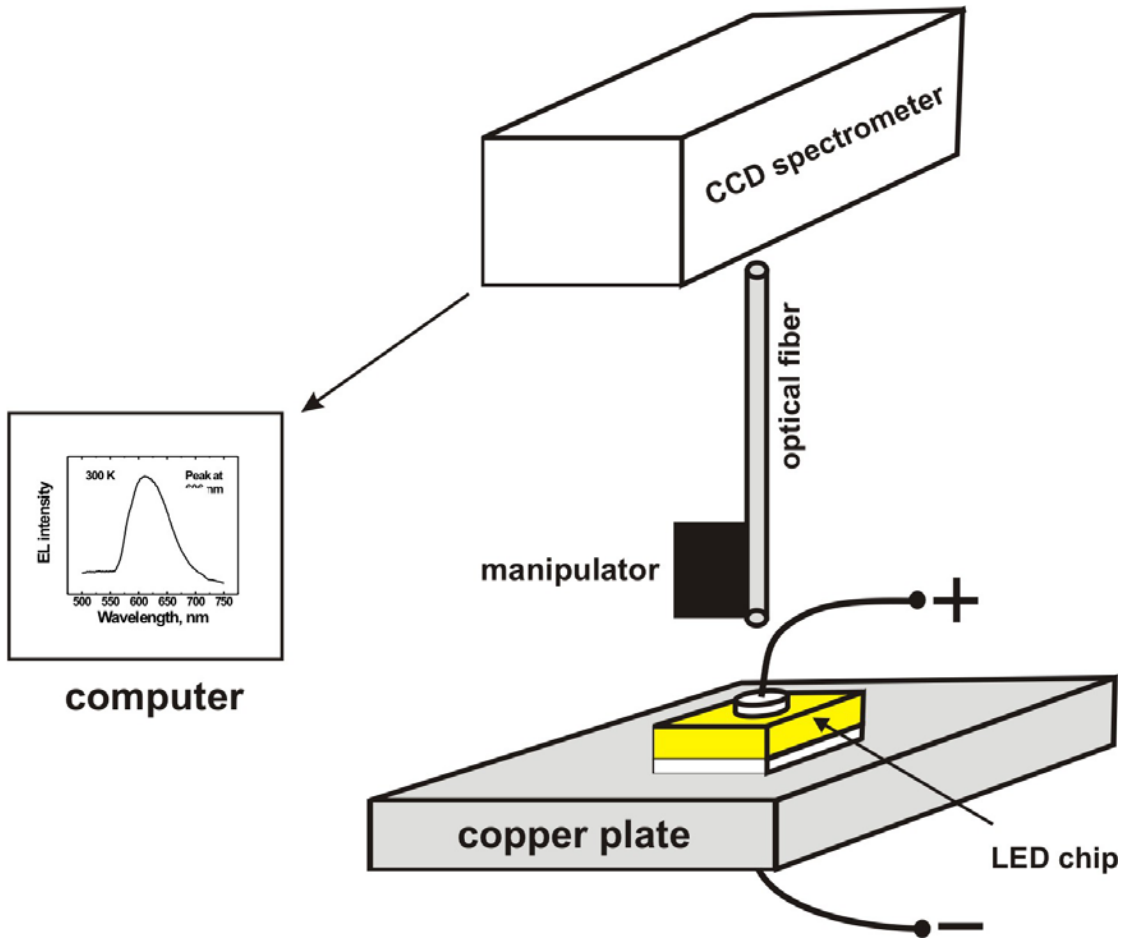

Figure 2.7. Schematic of the electroluminescence measurement system.

Electroluminescence is a measurement of the optical signal (optical emission spectrum) from the sample under a drive current. The experimental set up is shown in Fig. 2.7. An LED chip with broad area *n*-type metal contact on the bottom and circular *p*-

type metal contact on the top is placed on a copper plate. A direct current source is connected to the electrodes. An optical fiber is used to carry the optical signal to a CCD spectrometer BWTEK (BTC112E), operating in the 510 – 710 nm wavelength range. The optical fiber is fixed in a 3D micromanipulator to maximize the optical signal input from the LED chip. The CCD spectrometer is connected to a computer, where EL spectra are generated and analyzed. A typical DC current range of 5 – 150 mA is used for spectrum recording.

For current-voltage (I-V) measurements a Hewlett Packard probe station and an oscilloscope are used. I-V measurements are important to analyze the series resistance of an LED structure, the contact resistance, the offset voltage, and the reverse breakdown voltage. The voltage range of -30 V to 6 V is used for carrying out the I-V measurements.

A 20-cm-diameter integrating sphere is used for light intensity measurements of the packaged LED chips. The use of the integrating sphere is a courtesy of B. Yhan and J. J. Song of Xepix.

2.4. LED fabrication

This section describes the experimental processing equipment used for LED fabrication. The detailed description of the processing optimization is given in Chapter 4.

LED chip fabrication from LED wafers consists of contact deposition and LED chip dicing. Contact deposition includes depositing back-side *n*-type metal contact on the bottom of the grown LED wafer and 180-μm-diameter *p*-type metal contacts on top of the wafer. LED chip dicing then takes place to dice the processed wafer into individual LED chips.

For *n*-type contact deposition we use e-beam evaporation, which uses a high-energy electron beam to melt the surface of a target and evaporate it onto the sample. The process takes place in a high-vacuum chamber with the base pressure of about $5*10^{-7}$ Torr. To form an *n*-type contact on the GaP semiconductor wafer, we use three different targets: Ge, Au, and Ni. The thickness of the depositing metal is controlled *in-situ* by an oscillating crystal thickness monitor, in which changing settings allow to adjust the monitor to measure the thickness of a certain metal. The metal growth rate is controlled by the electron current, and a typical growth rate is 1-2 Å/s.

For circular *p*-type contact the process includes several major steps: spinning photoresist on the surface of the wafer; exposure under the mask in a Karl Seuss Microscope (KSM); development of the photoresist in a PLSI developer solution to form the circle features on the surface; depositing AuZn metal contact using a thermal evaporator; and, finally, lift-off in acetone. The last process dissolves the photoresist under the deposited metal and it lifts-off everywhere, but the circle areas where photoresist has been developed. This leaves the circular metal contacts on the top of the LED wafer.

The thermal evaporator is different from the e-beam evaporator. In the thermal evaporator a small quantity of the metal is put into a PBN crucible. A DC current of 8-12 A goes through the metal spire inside the crucible and heats it up. The metal melts and evaporates on the exposed sample surface. The thickness is monitored *in-situ*, using the oscillating crystal thickness monitor. A typical growth rate is about 1-2 Å/s, and it is controlled by an applied voltage. The reason for using a thermal evaporator for *p*-type contact deposition is the following. We use a $Au_{0.1}Zn_{0.9}$ alloy for *p*-type contacts. One slug (2 mm X 2 mm X 3 mm) of AuZn is used for one process in the thermal evaporator. In an e-beam evaporator the target size has to be much bigger to fill in the crucible. Heating the surface of AuZn may cause Zn segregation and evaporation, which will lead to a decrease of the Zn concentration in the target, and, consequently in the deposited contact layer. Therefore, thermal evaporator is used for p-type contact deposition.

Both *n*-type and *p*-type contacts are annealed by a Rapid Thermal Annealing technique to assure the alloying of the deposited metal with the semiconductor. The homemade RTA machine is a small (25 cm long, 5 cm diameter) glass tube with a substrate holder and powerful halogen lamp, which heats up the sample in about 5-10 seconds to the desired temperature. The temperature is controlled by a thermocouple, which has a feedback with the lamp power supply. This closed loop stabilizes the temperature of the substrate. The process takes place in nitrogen atmosphere to reduce oxidation of the semiconductor surface.

Dicing of the LED chip wafer with deposited contacts into individual LED chips is done manually under an optical microscope. The chip size is around 380 μm X 380 μm. Visual chip inspection is performed under an optical microscope, before characterization, to measure chip dimensions and assure good facet quality.

References:

[1] T. Sakamoto, Proc. NATO ASI, **93** (1998).

[2] M. B. Panish, J. Electrochem. Soc. **127**, 2729 (1980).

[3] J. C. P. Chang, J. Chen, J. M. Fernandez, H. H. Weider, and K. L. Kavanagh, Appl. Phys. Lett. **60**, 1129 (1992).

[4] W. J. Bartels, J. Vac. Sci. Techn. **B 1**, 338 (1983).

[5] P. M. Mooney, J. L. Jordan-Sweet, G. B. Stephenson, and J. O.Chu, Advances in x-ray Analysis **38**.

[6] P. Gay, P. B. Hirsh, and A. Kelly, Act. Metal. **1**, 315 (1953).

[7] S. Bensoussan, C. Malgrange, and M. Sauvage-Simkin, J. Appl. Cryst. **20**, 222 (1987).

[8] B. K. Tanner, Adv. X-ray Anal. **33**, 1 (1990).

Chapter 3. Growth and characterization of (Al,In,Ga)NP.

3.1. Overview

This chapter is devoted to the growth and characterization of GaNP layers, AlGaNP bulk layers, and InGaNP quantum wells (QWs) grown on GaP (100) substrates by plasma-assisted GSMBE. For each of the materials, growth and characterization details are given, and some of the optical and structural properties are studied.

For GaNP layers, growth conditions (e.g. substrate temperature) are optimized. Dependence of the GaNP band gap vs. nitrogen concentration is studied. Temperature dependent PL is measured and analyzed.

For AlGaNP layers, we explain the difference between nitrogen incorporation into GaP and AlP, using thermodynamic approach. We demonstrate and explain peculiarities of AlGaNP quaternary alloy growth: dependence of nitrogen concentration on Al composition and dependence of crystal quality on Al composition.

Temperature - dependent PL and dependence of the emission wavelength vs. nitrogen and indium compositions are studied for InGaNP QWs. Electron effective mass is determined for InGaNP material with different indium concentrations. Conduction and valence band offsets are calculated for the InGaNP/GaP heterojunction.

3.2. Growth and characterization of GaNP layers

This section is devoted to growth and characterization of GaNP layers. Some of the optical and structural properties of GaNP layers grown on GaP (100) substrates were studied by room-temperature and low-temperature PL and XRC.

3.2.1. Growth details

All the samples were grown on GaP(100) substrates. Substrate temperature was varied from 430^0C to 650^0C for different layers grown and the growth rate of 1μm/h was used.

Figure 3.1 shows a schematic of the test structure, which consists of a 200-nm-thick GaP buffer layer, a 200-nm-thick GaP bottom and top barrier layer and a 7-to-200-nm-thick GaN_xP_{1-x} active region with various *x*.

After the surface oxide of a GaP substrate is removed at 640^0C under P_2 flux, a GaP buffer layer was grown. Nitrogen plasma was ignited at the end of the buffer layer growth, without growth interruption to minimize the negative effect of a low-quality transition layer, formed at the moment of plasma ignition. This layer is a result of uncontrolled nitrogen incorporation into the growing film, when plasma discharge is ignited and plasma conditions are tuned. One can lower the uncontrolled nitrogen

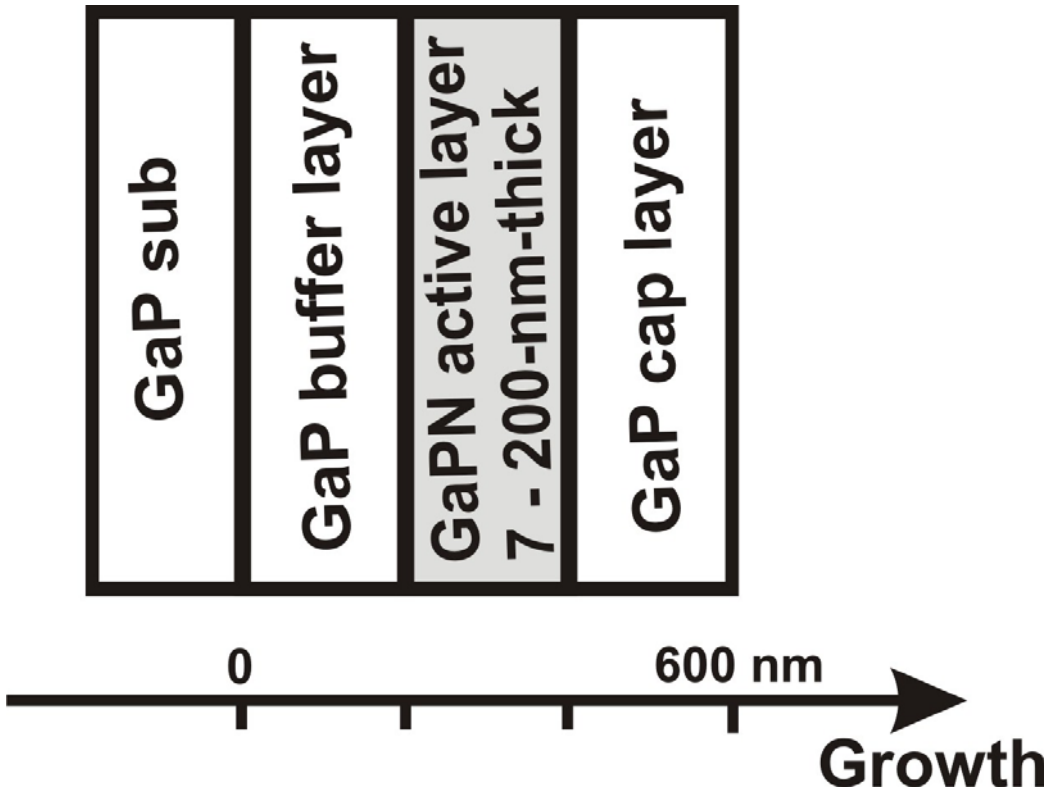

Figure 3.1. A schematic of the GaNP test sample.

incorporation by keeping the substrate temperature above 600^0C at the ignition moment and continuing the growth. After plasma conditions are set for the growth parameters, the substrate temperature was lowered to the growth temperature of GaNP, between 430^0C and 540^0C. Growth is monitored by reflection of high-energy electron diffraction (RHHED). A typical PH_3 flow rate of 3.5 sccm is used for the growth of GaP layers. A slightly reduced PH_3 flow rate is used for the growth of GaNP layers, in order to maintain a constant V/III ratio. The GaP cap layer is grown at a substrate temperature of 640^0C.

All the samples are annealed after the growth under a P_2 flux of 4.5 sccm at a substrate temperature of 700-720^{0}C for 2 minutes.

We use an Ar ion laser in the PL setup, presented in Fig. 2.5, for PL study of bulk GaNP, and a HeCd laser for the study of thin GaNP layers (quantum wells).

3.2.2. Optical properties

GaP is an indirect bandgap material, but it was previously demonstrated by our group[1,2,3,4,5,6] that adding a small amount of nitrogen (~0.5%) into GaP converts this material into direct bandgap and shifts the emission wavelength into the yellow spectral range.

The dependence of room-temperature (RT) PL peak wavelength from 200-nm-thick GaN_xP_{1-x} layers on nitrogen composition is shown in Fig. 3.2a. Increasing the nitrogen composition in the layer results in red shift of the PL peak position. This is similar to the GaNAs material system grown on GaAs substrates, but nitrogen seems to have a bigger impact when added into GaP. In particular, adding one percent of nitrogen into GaP decreases the bandgap by 320 meV versus 180 meV in GaAs[7]. This difference could be due to the different strain and nitrogen energy levels with respect to the conduction band in GaAs and GaP. Increasing the nitrogen concentration in the GaNP bulk layers from 0.6 to 1.7% shifts the light emission color from yellow-amber (605 nm) to red (670 nm). Room-temperature PL spectra of two GaNP samples with nitrogen

composition 0.62% and 1.17%, respectively, are shown in Fig. 3.2b. Unlike in GaNAs, increasing the N concentration in GaNP does not result in a decrease of the PL intensity.

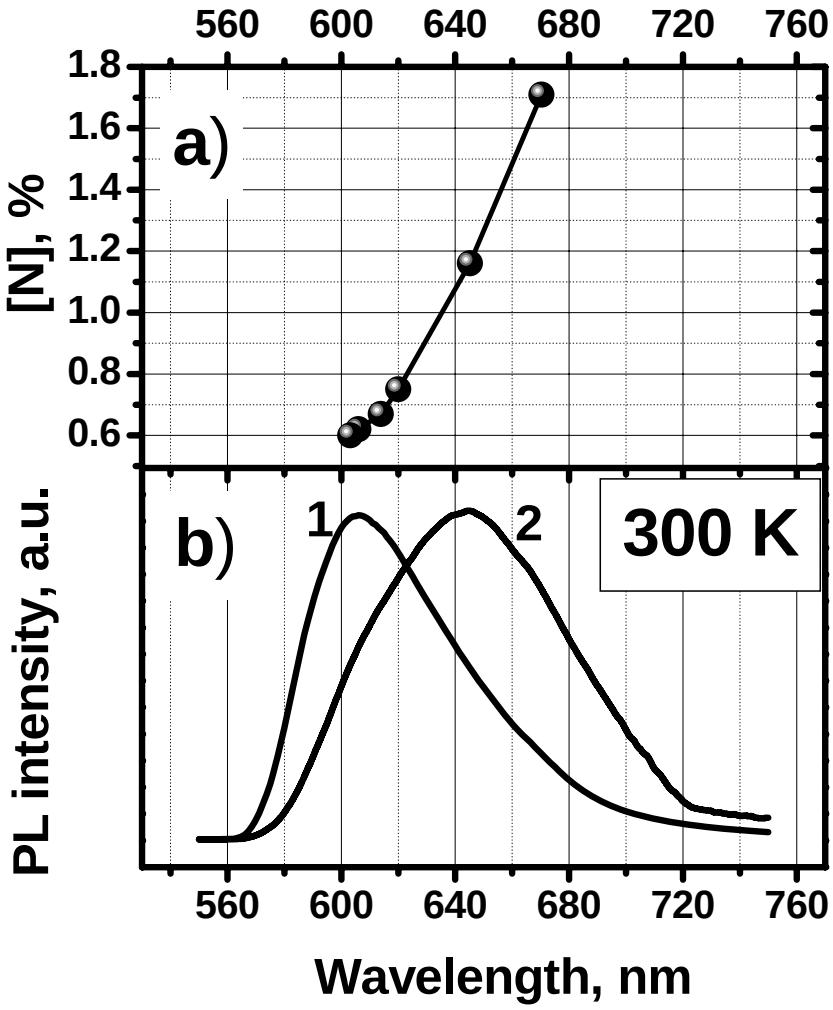

Figure 3.2. a) Dependence of the PL peak wavelength on nitrogen composition in GaNP at room temperature; b) RT PL spectrums of: 1 – test structure with [N]=0.62%, 2 - test structure with [N]=1.17%.

Figure 3.3 shows the dependence of PL intensity and FWHM of the PL peak of a 200-nm-thick $GaN_{0.006}P_{0.994}$ layer on substrate temperature. The highest PL intensity is

observed in the 500 to 520^{0}C window (shaded area in Fig. 3.3), and the FWHM of the PL peak has the minimum in the same window. The influence of the substrate temperature on structural properties of the GaNP bulk layers is described in the paragraph 3.2.3.

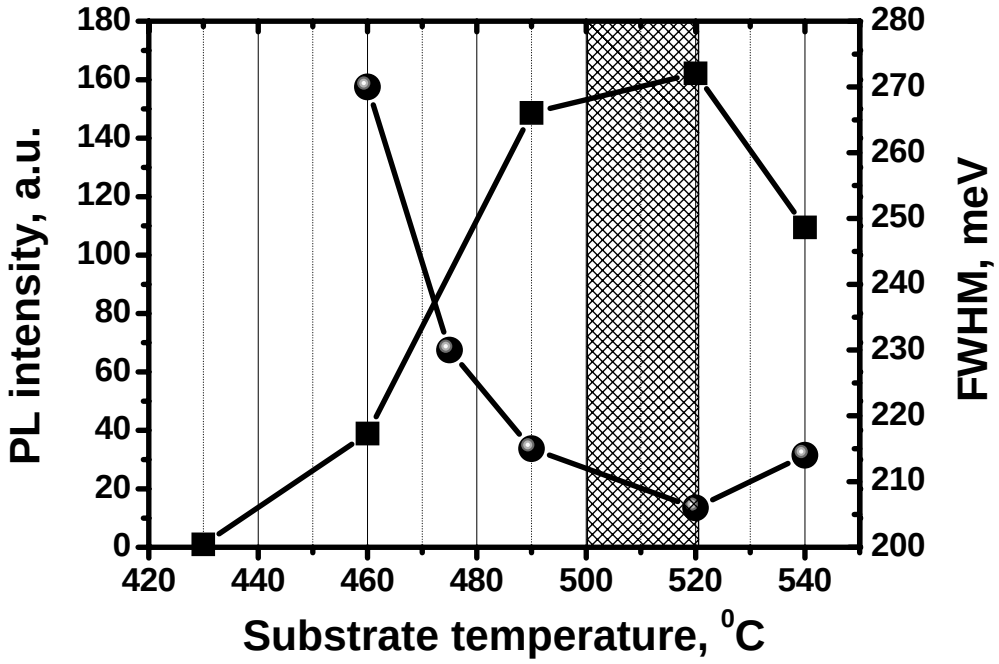

Figure 3.3. Dependence of RT PL intensity and FWHM of RT PL peak of $GaN_{0.006}P_{0.994}$ bulk layers on substrate temperature.

A wavelength of 610 nm, important for RGB white LEDs, requires [N]=0.62% in bulk GaN_xP_{1-x} layers (see Fig. 3.2a). We have studied influence of the thickness of $GaN_{0.0062}P_{0.9938}$ layer on PL intensity. Figure 3.4 shows the dependence of $GaN_{0.0062}P_{0.9938}$ PL intensity on layer thickness, *W*. The PL intensity increases with *W* increasing up to 200 nm because of increased light absorption and electron-hole recombination. Nitrogen affects mainly the conduction band of GaP, so the valence band

position is almost the same for both GaP and GaNP. Thus, holes are free to move between GaNP and GaP, and increasing the thickness of the GaNP active layer results in an increase of the probability of electron-hole recombination. Thus, the PL intensity increases with layer thickness. Then the PL intensity starts to decrease slowly with thickness. Based on Matthew and Blakeslee's model[8], the critical thickness of $GaN_{0.0062}P_{0.9938}$ layer grown on GaP is calculated to be 300 nm, which is in good agreement with our experimental data, showing a decrease of PL intensity when $W > 200$ nm.

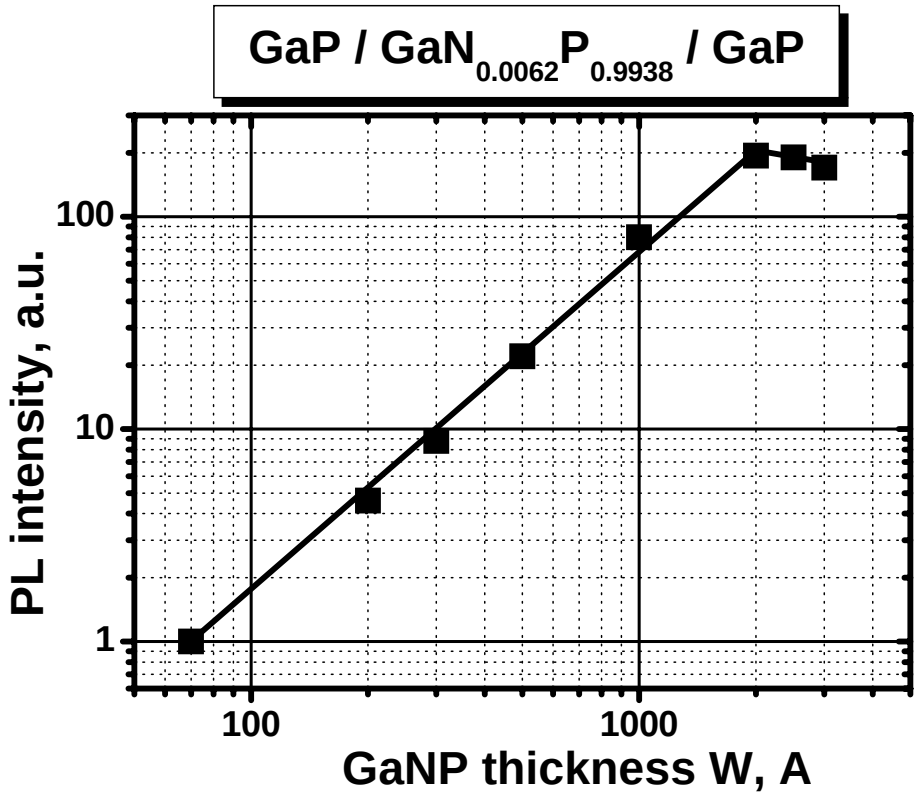

Figure 3.4. Dependence of PL intensity of $GaN_{0.0062}P_{0.9938}$ layer on layer thickness.

It is important to mention that in this experiment the Ar laser light gets absorbed mainly in the GaNP layer and little absorption takes place in the GaP confinement layers, limiting the number of carriers, that are get excited in GaP and diffuse into GaNP. Figure 3.5 clarifies this statement. Figure 3.5 represents the band diagram of the GaP/ $GaN_{0.0062}P_{0.9938}$/GaP structure with corresponding energy bandgaps. Eg of GaP is 2.26 eV (Fig. 3.5), and since GaP is an indirect bangap semiconductor, Eg is the energy distance between X-valley of the conduction band and Γ-valley of the valence band. The energy distance between Γ-valleys of the conduction and valence bands is 2.76 eV, i.e. larger than the GaP bandgap. Eg of $GaN_{0.0062}P_{0.9938}$ is 2.032 eV, and GaNP is a direct bandgap semiconductor. The energy of an Ar ion laser (514 nm) is 2.41 eV. This energy is not

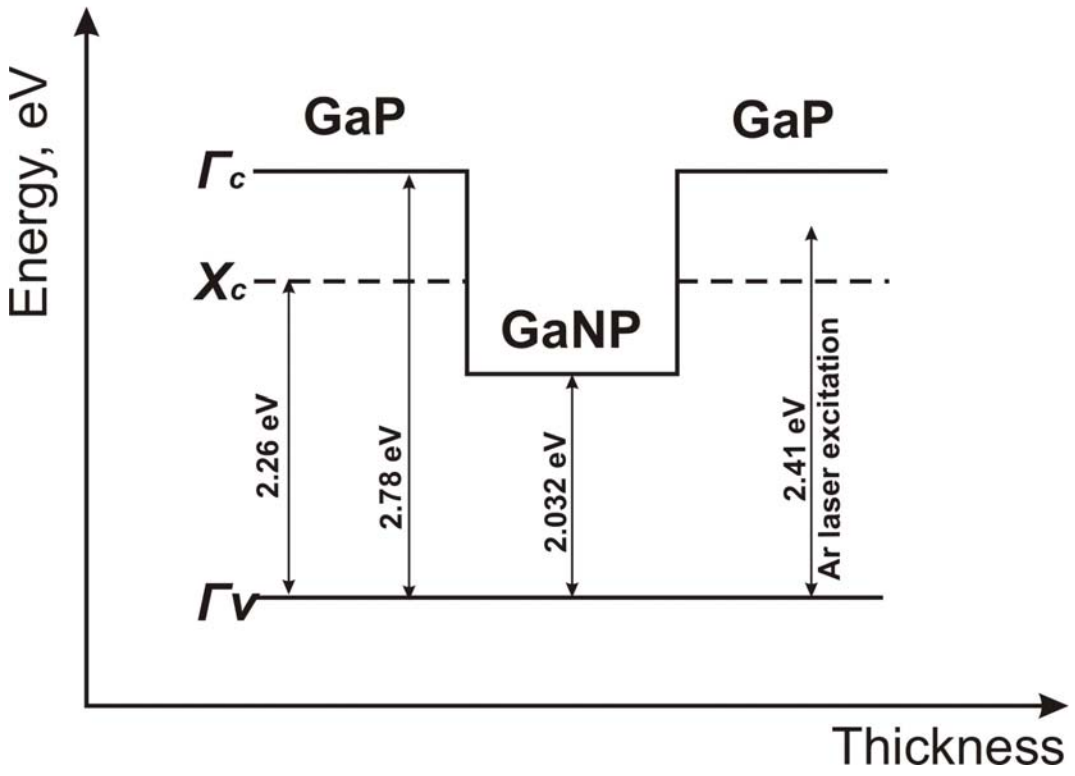

Figure 3.5. A band diagram of GaP/GaNP/GaP double heterostructure.

sufficient to excite electrons to the Γ-valley of GaP, but enough to excite electrons to the X-valley of GaP. The photon absorption in GaP with electron being excited into X-valley is a phonon-assisted process, since electron momentum changes when moved from Γ- to X-valley. This means that optical excitation of GaP is not an efficient process, when an Ar laser is used, as it requires electrons to change their momentum. Thus, only direct bandgap $GaN_{0.0062}P_{0.9938}$ layer can be efficiently pumped with an Ar laser (514 nm) in the structure, presented in Fig. 3.5. Increase of the thickness of the GaNP layer leads to higher absorption and recombination, leading to increase of the PL intensity of the GaNP layer. That is why for the temperature-dependent PL measurements of thin GaNP layers (quantum wells) described below we used a HeCd laser with photon energy of 3.8 eV.

Temperature-dependent PL of a 7-nm-thick $GaN_{0.005}P_{0.995}$ quantum well is studied. Figure 3.6a shows temperature dependence of the transition energy. The symbols are experimental data, and the solid curve is the best fit with the Varshni equation:

$$E(T)=E(0)-\alpha\times T^2/(T+\beta) \qquad (3.1),$$

where α and β are fitting parameters. One can see that the temperature dependence of the transition energy for the GaNP quantum well can be fit very well with the Varshni equation with $\alpha=2.7\times10^{-4}$ eV/K and β=140 K, which means that no localized defects are detected in the studied epi-layer. Figure 3.6b shows PL spectra corresponding to the solid data points in Fig. 3.6a. One can see that PL intensity decreases 900 times when the temperature is increased from 80 K to 300 K. This significant quenching of the PL intensity may indicate the presence of growth impurities (non-radiative recombination centers, e.g. oxygen) in the GaNP layer. For comparison, a typical difference in the PL

intensity between 300 K and 80 K for optimized InGaNAs/GaAs quantum wells is a factor of 20-30 [9].

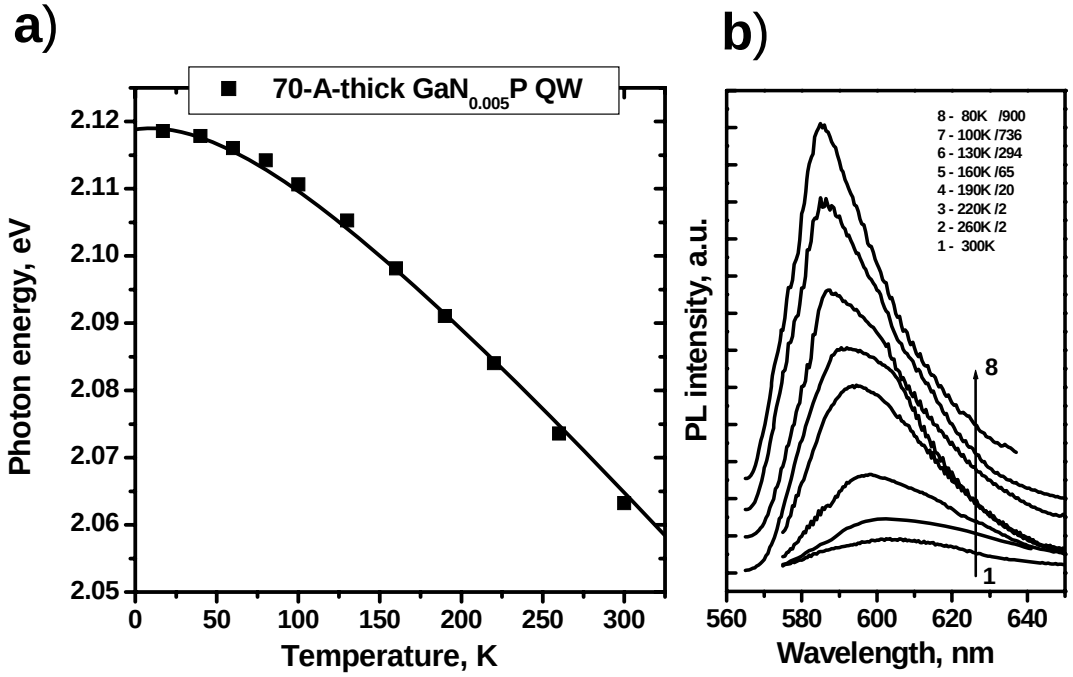

Figure 3.6. a) Dependence of the photon energy vs. temperature for 70-Å-thick $GaN_{0.005}P$ QW. Symbols are experimental data, and solid lines are the best Varshni fit; b) PL spectrums for the 70-Å-thick $GaN_{0.005}P$ QW, taken at different temperatures.

3.2.3. Structural properties

Structural properties of GaNP layers grown on GaP substrates are studied together with optical properties. Nitrogen concentration is determined from x-ray diffraction rocking curves. Figure 3.7 shows x-ray diffraction rocking curves of three 100-nm-thick GaNP samples with different nitrogen concentration (0.4%<[N]<1.16%), grown at the same substrate temperature of 510^0C. The Pendellosung fringes are well resolved, and the

full width at half maximum (FWHM) of the peaks is relatively narrow (~ 90-100 arcsec), which means high crystalline quality. All the layers grown are pseudomorphically strained, i.e. thinner than the critical thickness calculated based on the Matthew and Blakeslee's model. For the $GaN_{0.004}P_{0.996}$ layer the critical thickness is calculated to be ~ 400 nm, for $GaN_{0.006}P_{0.994}$ ~ 300 nm, and for $GaN_{0.0116}P_{0.9884}$ ~ 140 nm.

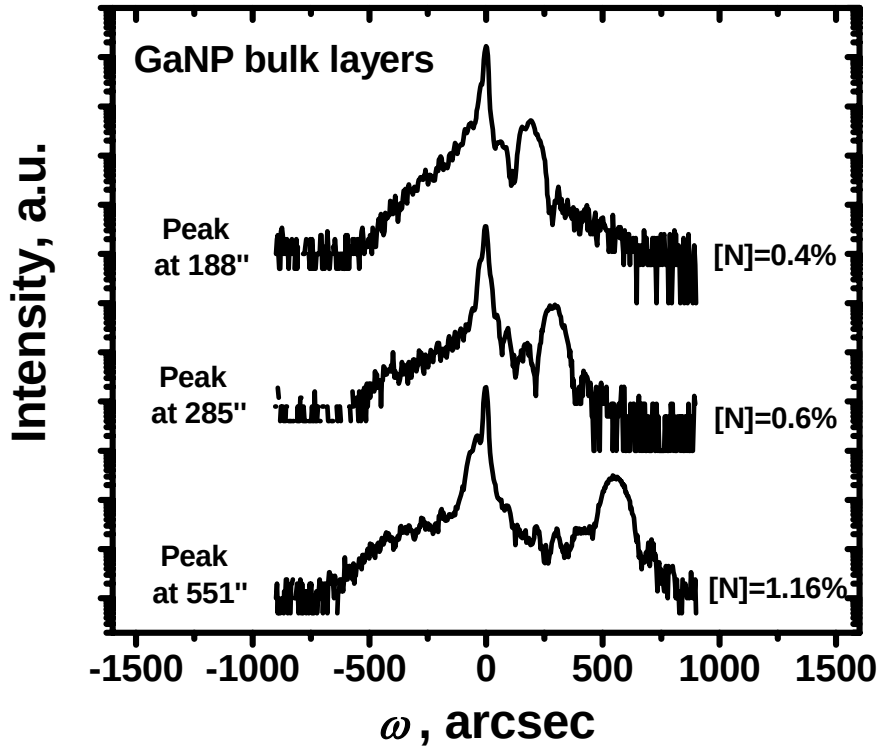

Figure 3.7. (400) x-ray rocking curves for 100-nm-thick GaNP layers with different nitrogen concentrations ([N] = 0.4%, 0.6%, 1.16%).

A series of 200-nm-thick $GaN_{0.006}P_{0.994}$ samples is grown at different substrate temperature ($430^0C<T_{sub}<540^0C$) in order to study the effect of T_{sub} on the structural properties of GaNP. Figure 3.8 shows the dependence of FWHM of the x-ray peaks on

substrate temperature. One can see that for substrate temperature less than 500^0C the FWHM increases slowly, around 10 arcsec per 20^0C, but for substrate temperature higher than 520^0C the FWHM increases rapidly, more than 40 arcsec per 20^0C, indicating degradation of structural quality. This is because of the tendency for clustering with increasing substrate temperature[10] due to the large miscibility gap. RHEED patterns also confirm this observation, streaky at low growth temperature and dash-like at higher growth temperature.

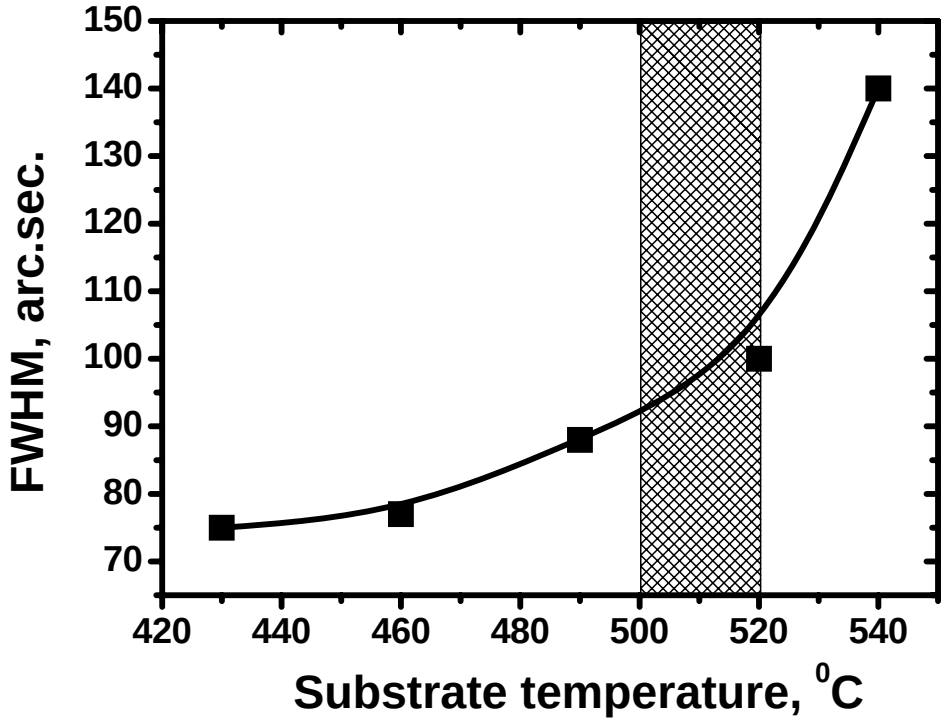

Figure 3.8. Dependence of the FWHM of x-ray peak of $GaN_{0.006}P_{0.994}$ bulk layer on substrate temperature.

The results from Fig. 3.8 combined with the results from Fig. 3.3 of the previous paragraph allow us to conclude that the best substrate temperature for growth of GaNP

layers is $500^0C<T_{sub}<520^0C$ (shaded area in Fig. 3.8). This provides narrow X-ray and PL peaks and the highest PL intensity.

3.3. AlGaNP bulk layers

AlGaNP might be used in order to blue-shift the emission wavelength, since the AlP bandgap (2.71eV) is higher than that of GaP (2.27eV). First green LEDs were based on nitrogen-doped GaP, because nitrogen is known as an effective isolelectronic trap in GaP[11]. There were attempts to decrease the emission wavelength in those kinds of structures by doping AlGaP with nitrogen. Emission wavelength blue-shift has been achieved in AlGaP:N structures, compared to GaP:N structures[12].

This section describes growth and characterization of bulk AlGaNP layers. Thermodynamic approach is used to explain the difference in nitrogen incorporation into GaP and AlP layers. X-ray diffraction measurements are used to determine Al and N concentrations in the AlGaNP layers. Based on that, the peculiarities of the growth of quaternary AlGaNP alloy with different aluminum and nitrogen compositions are discussed and explained.

3.3.1. Growth and characterization details

All samples are grown on GaP (100) substrates with a Varian GEN II MBE system. Substrate temperature is varied from 500^0C to 650^0C for different layers grown,

and a growth rate of 1.5-2.3 Å/s is used. The samples consist of a GaP substrate, a 0.2-μm-thick GaP buffer layer followed by a 0.1-μm-thick GaNP, AlNP or AlGaNP active layer and capped with a 0.1-μm-thick GaP layer. All samples show mirror-like surfaces. Both Al and N mole fractions affect the lattice parameter (and, therefore, x-ray peak position) of quaternary AlGaNP alloys. In order to separate the contributions of each constituent binaries into the x-ray peak position of AlGaNP, a 0.1-μm-thick pseudomorphic AlP layer is grown on a GaP substrate, and the x-ray peak position of the AlP layer is measured to be -750 arcsec (Curve 1 in Fig. 3.9). Then, the x-ray peak position of an $Al_xGa_{1-x}P$ layer with $0 \leq x \leq 1$ can easily be calculated. The Al composition is

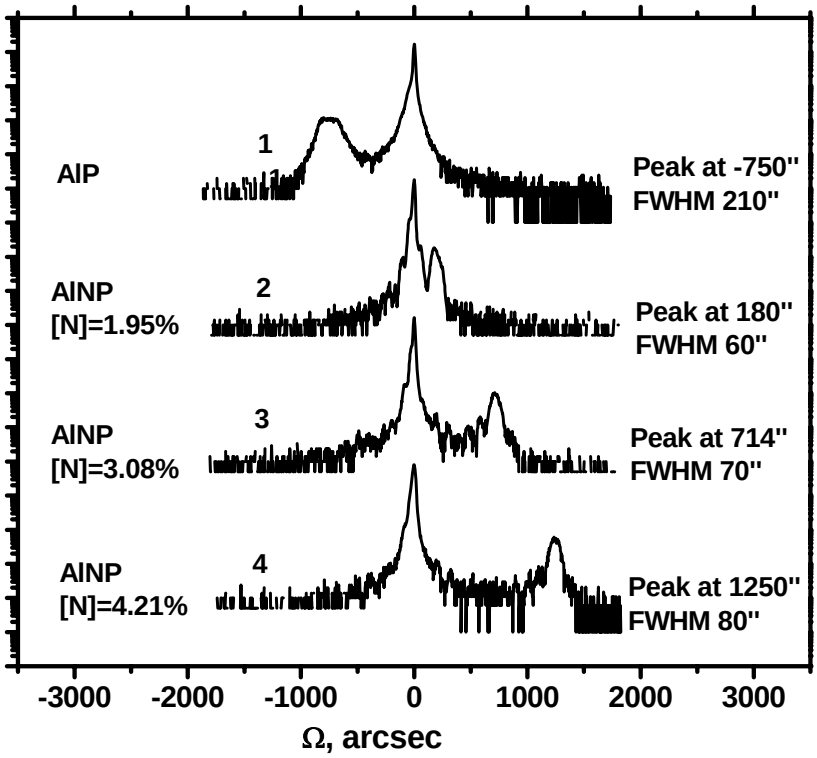

Figure 3.9. (400) x-ray diffraction rocking curves of AlNP layers with the nitrogen composition varied from 0 to 4.21%.

controlled by the Al/Ga flux ratio. When an $Al_xGa_{1-x}N_yP_{1-y}$ alloy is grown, the contribution of Al into the x-ray peak position is known in advance, based on what is described above. The difference between x-ray peak positions of $Al_xGa_{1-x}P$ and $Al_xGa_{1-x}N_yP_{1-y}$ grown on GaP solely depends on the amount of nitrogen incorporated, assuming that nitrogen does not affect incorporation of Al. Then, the nitrogen composition can be determined.

All the layers grown are assumed to be pseudomorphically strained. The lattice constant of GaP is 5.45 Å, and that of AlP is 5.46 Å, so the lattice mismatch between those two alloys is 0.18 % and the critical thickness is calculated to be 3400 Å, based on the Matthew and Blakeslee's model[8]. For the $AlN_{0.042}P_{0.958}$ alloy grown on GaP (Curve 4 in Fig. 3.9), the lattice mismatch is 0.55 % (the highest mismatch among the structures grown), and the critical thickness is calculated to be 1100 Å, based on the Mathew and Blakeslee's model[8]. The above allows determining the nitrogen concentrations in AlNP layers from x-ray diffraction rocking curves, which are presented in Fig. 3.9. The same approach is taken when the N concentration is determined in AlGaNP layers.

3.3.2. Thermodynamic analysis and structural properties

The efficiency of the nitrogen plasma cell producing nitrogen radicals is determined by optical plasma intensity (see Chapter 2.2). The nitrogen composition in a layer is directly proportional to plasma intensity, if all other growth conditions are kept the same. Figure 3.10 shows the dependence of nitrogen composition on plasma intensity

for GaNP and AlNP layers, grown under the same phosphorus flux and substrate temperature. The nitrogen composition is normalized to a growth rate of 1.9 Å/s, since it is inversely proportional to growth rate. Both dependencies are linear as expected, but AlNP layers have more nitrogen by a factor of 3.4.

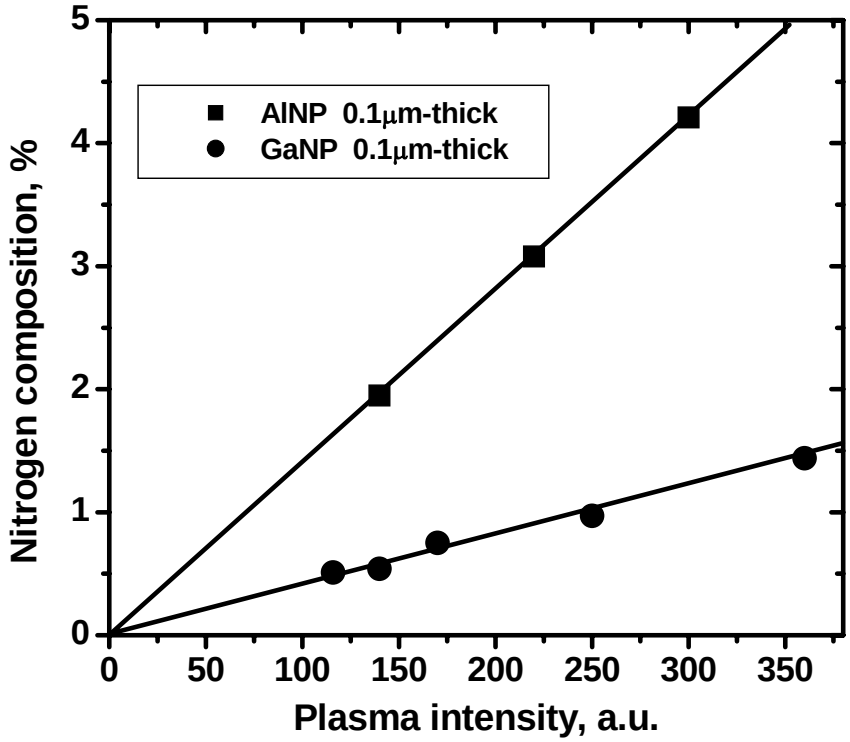

Figure 3.10. Dependence of the nitrogen composition in AlNP and GaNP layers on plasma intensity.

To investigate why nitrogen incorporates into AlP more easily than into GaP, we apply an equilibrium thermodynamic model to describe the growth of these compounds. This model was developed for description of MBE growth process of AlGaAs[13] and InGaAsP[14], and it takes into account growth parameters such as elemental fluxes and substrate temperature. The model was applied to describe the growth of dilute nitrides,

e.g. GaNAs[15,16] and GaInNAs[17], as well. According to the model, the reaction of formation of AlNP and GaNP ternary solutions can be divided into reactions of formation of binary compounds:

$$Al + P \Rightarrow AlP \quad (3.2a),$$

$$Al + N \Rightarrow AlN \quad (3.2b),$$

$$Ga + P \Rightarrow GaP \quad (3.3a),$$

$$Ga + N \Rightarrow GaN \quad (3.3b),$$

Then, a ternary solution is a mixture of two binary components with corresponding interaction parameters. A larger energy released during a reaction results in easier formation of the binary compound from the elements. We will consider Gibbs free energy ($\Delta G(T)$) for each of those reactions. For (3.2a) and (3.3a) $\Delta G(T)$ is calculated from the known temperature dependence of equilibrium constant K [18]:

$$K = \exp(\Delta G/RT) \quad (3.4),$$

where R is the gas constant. For reactions (3.2b) and (3.3b) $\Delta G(T)$ is calculated using Ref. 19, in which thermodynamic analysis applied by the authors leads to $\Delta G(T)$ of GaN and AlN binary compound formation to be written as:

$$\Delta G(T) = A + B/T + C \times T \times ln(T) + D \times T + E \times T^2 \quad (3.5).$$

A, B, C, D and *E* coefficients[19] are also taken from Ref. 19.

Calculation results in the temperature range of 400^0C to 600^0C are presented in Fig. 3.11. ΔG_{GaN} is lower than ΔG_{GaP} in the concerned temperature range, and ΔG_{AlN} is lower than ΔG_{AlP}. This means that nitrogen incorporation into GaP and AlP is energetically favorable. The difference between ΔG_{GaN} and ΔG_{GaP} at 500^0C (growth

temperature) is smaller than that between ΔG_{AlN} and ΔG_{AlP} at 500^0C. Thus, nitrogen incorporation into AlP is easier than nitrogen incorporation into GaP, if growth conditions are kept the same. This qualitative analysis explains the difference in nitrogen incorporation into GaP and AlP.

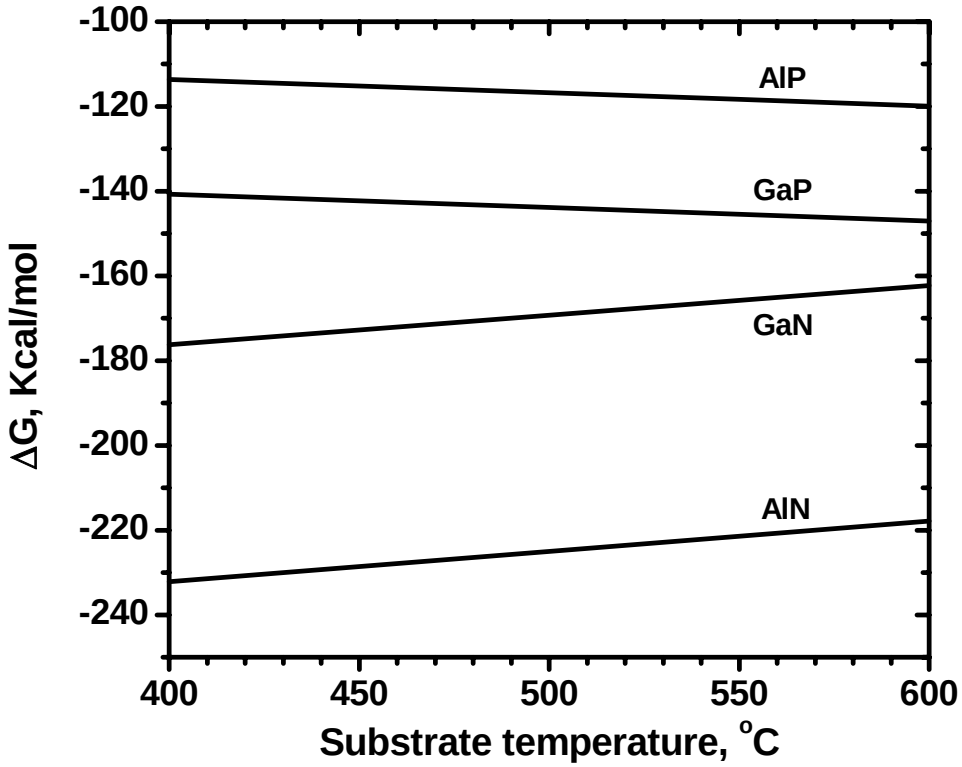

Figure 3.11. Dependence of free Gibbs energy on the substrate temperature for reactions of formation of AlP, GaP, GaN and AlN.

Such a large (factor of 3.4) difference in nitrogen incorporation into AlP and GaP may affect the growth of AlGaNP quaternary alloys. In order to investigate how this incorporation difference influences on the crystal quality of AlGaNP, a series of AlGaNP layers with different aluminum concentration (15, 25, 50 and 80%) is grown. Plasma

source conditions (power and nitrogen flux) are kept the same as well as the total growth rate (1.9 Å/s) and substrate temperature (500^0C). The plasma source conditions result in 0.6% nitrogen incorporated into GaP at a given growth rate (1.9 Å/s). Increasing the aluminum composition in the layer results in increasing nitrogen composition in the layer, as expected. Figure 3.12 shows (004) x-ray diffraction rocking curves of the

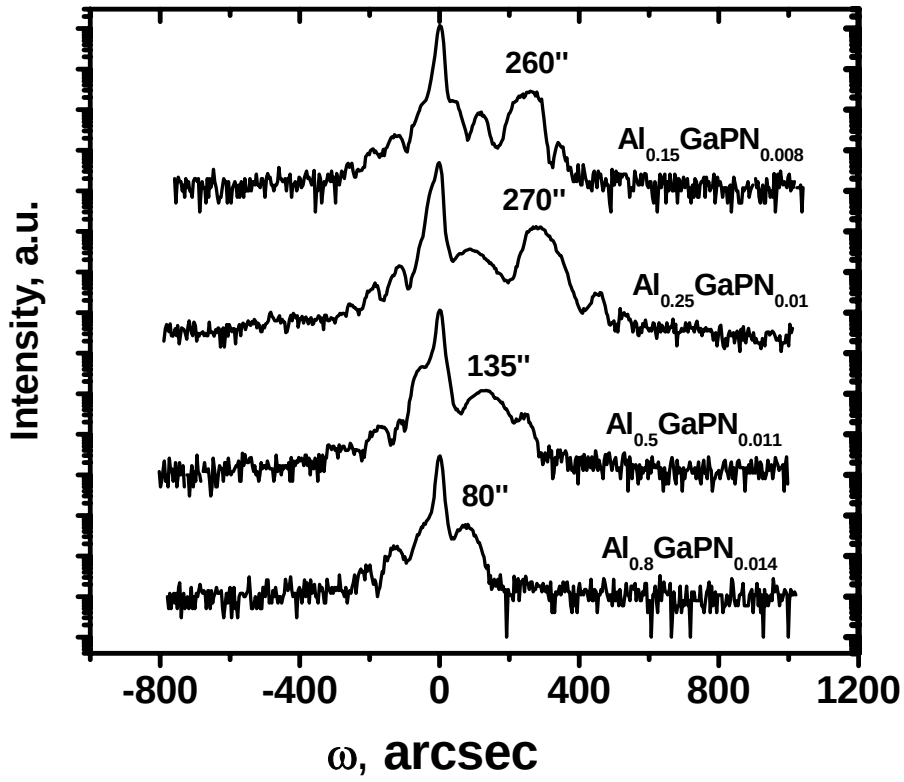

Figure 3.12. (004) x-ray diffraction rocking curves of 0.1-μm-thick AlGaNP layers with different nitrogen and aluminum composition. The peak positions from AlGaNP epi-layers are indicated.

AlGaNP layers grown. One can see that single crystal AlGaNP layers are grown. Pundellosung fringes are well resolved in the x-ray rocking curves. Figure 3.13a shows the nitrogen concentration in the AlGaNP layers vs. aluminum composition. The straight

line is a linear interpolation of nitrogen concentration in AlGaNP, based upon Fig. 3.10. The symbols represent experimental data. Figure 3.13b shows the dependence of full width at half maximum (FWHM) of (004) x-ray diffraction peaks of the AlGaNP layers

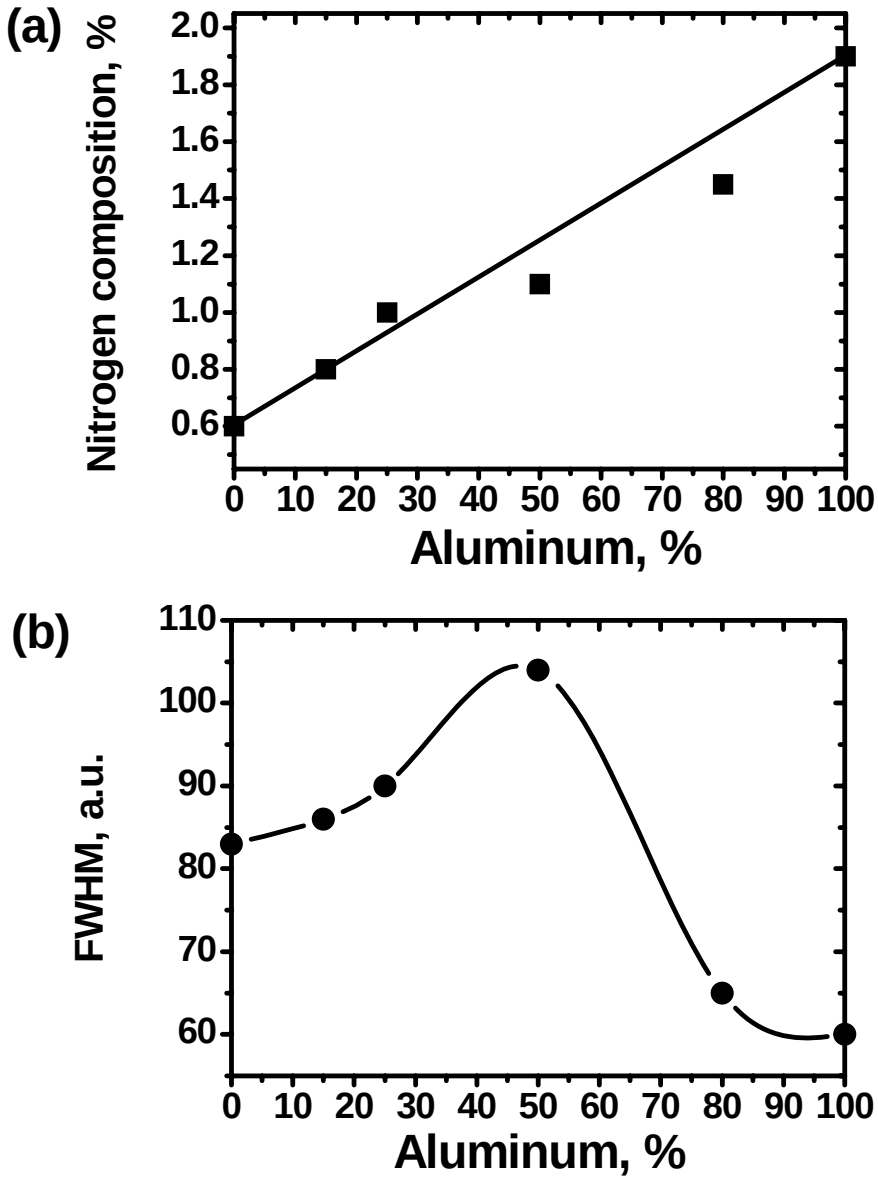

Figure 3.13. a) Nitrogen concentration in AlGaNP layers vs. aluminum composition for the same plasma source conditions used; b) full widths at half maximum of (004) x-ray diffraction peaks vs. aluminum composition in the AlGaNP layer.

on aluminum composition. The corresponding nitrogen concentrations are demonstrated in Fig. 3.13a. One can see that the maximum FWHM is reached at 50% of aluminum in the layer. That means at 50% aluminum the crystal quality of the quaternary alloy is the worst. This result is expected since the difference in nitrogen incorporation into GaP and AlP has the strongest effect in the $Al_{0.5}Ga_{0.5}P$ layer. Other compositions will exhibit more GaNP-like or AlNP-like behavior, and the effect of the nitrogen incorporation difference will be reduced. It is important to notice that the FWHM of AlGaNP with 0%<[Al]<20% (~ 85 arcsec) is larger than that of AlGaNP with 80%<Al<100% (~ 60 arcsec), given the same growth conditions. This is due to the smaller strain in the AlGaNP layer with 80%<Al<100% (see the peak positions in Fig. 3.12).

Thus, during the growth of AlGaNP quaternary alloy, the difference in nitrogen incorporation into GaP and AlP should be taken into account when predicting the average nitrogen concentration in the layer. Adding aluminum will increase nitrogen concentration according to the dependence in Fig. 3.13a. However, these complications may be avoided if using an AlP/GaNP superlattice as a digital alloy of AlGaNP. In this case the average nitrogen concentration in the alloy is simply calculated from the thicknesses of AlP and GaNP layers, and the known nitrogen concentration in GaNP.

Photoluminescence signal has not been detected from the AlGaNP layers both at room temperature and at low temperature (~80 K). We explain this by two reasons. First, GaP/AlGaNP heterojunction is a type II heterojunction, and no carrier confinement for holes exist. Taking into account the use of the relatively thin layers (0.1 μm), we may conclude that holes diffuse from the AlGaNP layer into GaP barrier and cap layers.

Second, more nitrogen is required to convert AlGaP from indirect bandgap into direct bandgap as compared to GaP, because of the larger E_g of AlGaP. The lowest Al concentration used in AlGaNP layer is 15% (Fig. 3.12), and corresponding nitrogen concentration is 0.8%. This may not be enough for converting AlGaP into a direct bandgap material.

3.4. InGaNP quantum wells

Incorporation of only 0.4% of nitrogen into GaP converts the material from indirect into direct bandgap and shifts the emission wavelength into the yellow spectral range. Unlike the InGaNAs/GaAs material system, there is little information available about the optical properties of InGaNP quantum wells (QWs) in GaP barriers. In this section we study the optical properties of InGaNP/GaP QWs and the influence of post-growth annealing on PL properties of InGaNP/GaP QWs, describe temperature-dependent photoluminescence, and determine the electron effective mass in InGaNP material as dependent on the In concentration. Finally, we calculate band offsets of InGaNP QW in GaP barriers.

3.4.1. Growth details

All samples are grown directly on GaP(100) substrates in a Varian GEN II gas source molecular beam epitaxy (GSMBE) system. Substrate temperature is varied from 480^0C to 650^0C for different layers grown and a growth rate of 1 μm/h is used. Post-growth annealing is carried out in situ at a temperature of 700 ^{0}C for 2 minutes under an excessive phosphorous flux.

The sample structure consists of a GaP (100) substrate, a 200-nm-thick GaP buffer layer, a 4-to-10-nm-thick $In_yGa_{1-y}N_xP_{1-x}$ quantum well with various x and y, and a 200-nm-thick GaP cap layer.

Nitrogen plasma source conditions (nitrogen flux, F, and applied RF power, P) are different for the samples grown in order to change the nitrogen concentration in the epi-layers. The nitrogen flux range is 0.3 sccm $\leq F \leq$ 1 sccm, and the applied RF power is changed in the range of 100 W $\leq P \leq$ 375 W. This range of plasma source conditions ensures a nitrogen concentration of 0.04% $\leq$ [N] $\leq$ 2 % in the InGaNP layers. We assume that In has negligible influence on the nitrogen incorporation efficiency into GaP, and calculate the nitrogen concentration by normalizing it to the total group-III flux (growth rate). This assumption is valid for the InGaNAs material system, according to thermodynamic calculations[17]. The total group-V/group-III flux ratio is kept the same for all the samples grown.

PL measurements are carried out at the temperature range of 20 K to 300 K using a 15 mW HeCd laser as the optical pumping source. PL signal is detected by a photoelectron multiplier.

3.4.2. Optical properties

First, we study the effect of the post-growth annealing on the optical properties of InGaNP quantum wells. The reason why we are interested in annealing is that the growth temperature of nitrogen-containing films is relatively low (<500^{0}C). This may lead to a formation of the point defects, due to a suppressed migration of the atoms on the growth surface. Another kind of point defects may be created by high-energy ions coming out of the nitrogen plasma source and bombarding the surface. Post growth annealing allows to reduce the number of point defects in the epi-layers.

In order to study the effect of post-growth annealing on the optical properties of InGaNP quantum wells, two test samples with 7-nm-thick $In_{0.1}Ga_{0.9}N_{0.005}P_{0.995}$ are grown under the same growth conditions. One of the samples is annealed in situ at 700^{0}C for two minutes. Figure 3.14 shows PL spectra of both samples, taken at 300 K. The annealed sample exhibits 5 times stronger PL intensity than the unannealed one and shows a blue shift of 2 nm. Thus, annealing of an InGaNP/GaP QW has similar effects on the optical properties as annealing of an InGaNAs/GaAs QW[20], as expected. All samples used for the following study are annealed according to the procedure described above, to ensure the best optical quality achievable with the equipment and conditions used.

We have studied the optical properties of 7-nm-thick $In_yGa_{1-y}N_{0.008}P_{0.992}$ single quantum wells with GaP barriers. Figure 3.15a presents the dependence of transition energy in $In_yGa_{1-y}N_{0.008}P_{0.992}$ QWs on indium composition at 20K and 300K. The red shift of the PL peak is clearly observed with increasing In composition, as expected. The

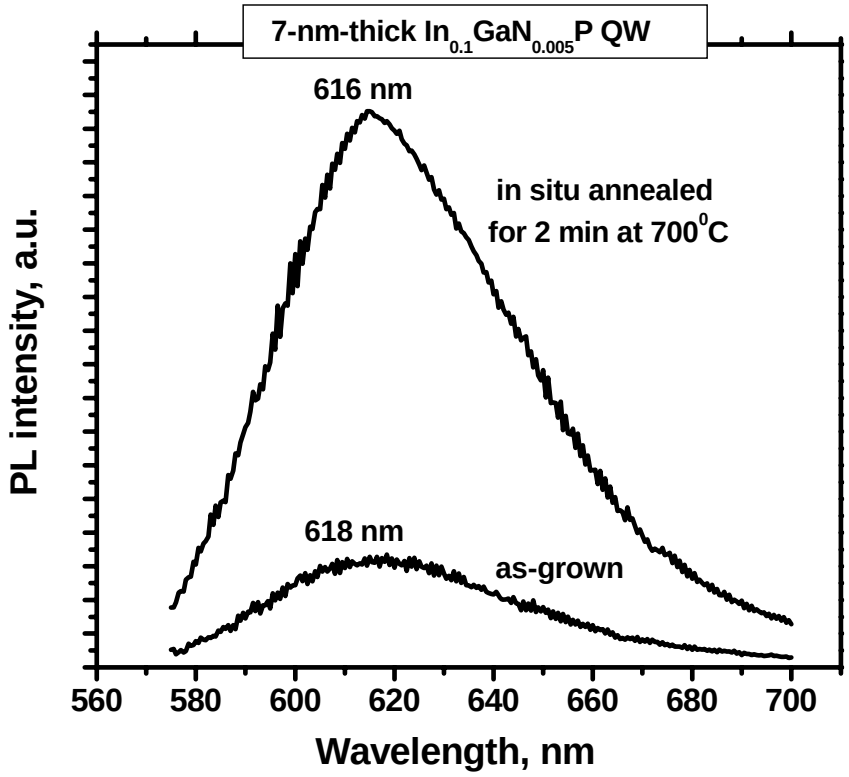

Figure 3.14. Photoluminescence spectra of as-grown and annealed 7-nm-thick $In_{0.1}GaN_{0.005}P$ quantum well in GaP barriers.

dashed curve in Fig. 3.15a shows the dependence of RT PL intensity of $In_yGa_{1-y}N_{0.008}P_{0.992}$ QW on indium composition. The PL intensity increases 12 times, when the indium composition increases from 0 to 20 %, which is probably due to an increase of the band offsets between the barrier layers and the QW layer**.** Figure 3.15b shows RT and low-temperature (20 K) PL spectra of the $In_{0.1}Ga_{0.9}N_{0.008}P_{0.992}$ QW.

The effect of changing the nitrogen and indium concentrations in 7-nm-thick InGaNP/GaP quantum wells has been studied. Twelve samples with different nitrogen ($0.5\% \leq [N] \leq 2\%$) and indium ($0\% \leq [In] \leq 22\%$) concentrations in the quantum wells have

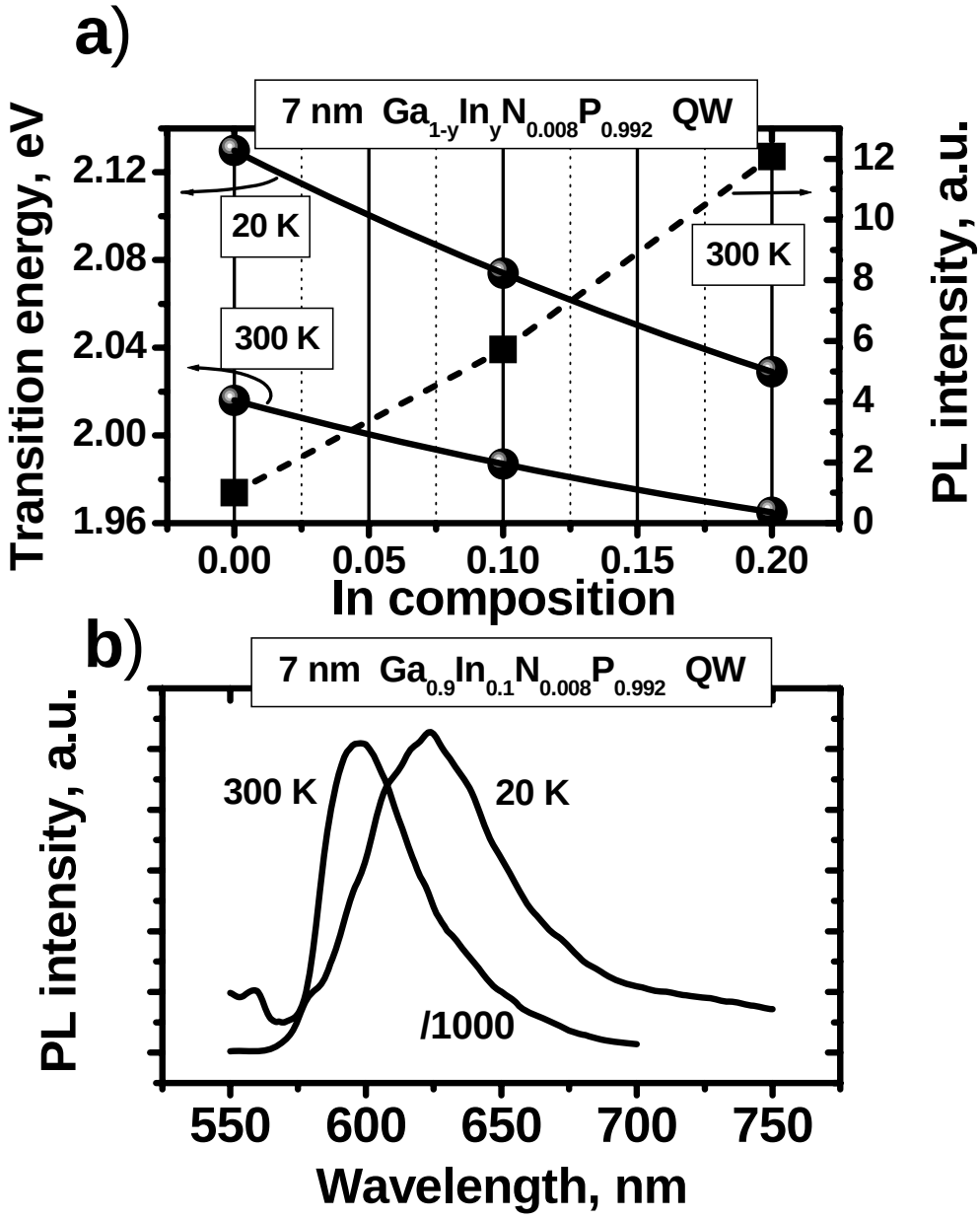

Figure 3.15. a) Dependence of transition energy in $In_yGa_{1-y}N_{0.008}P_{0.992}$ QW on *y*: 1 – at 20K, 2 – at 300K; 3 – dependence of RT PL intensity of $In_yGa_{1-y}N_{0.008}P_{0.992}$ QW on *y*; b) PL spectra of$In_{0.1}$ $Ga_{0.9}N_{0.008}P_{0.992}$ QW recorded at 1 – 20K, 2 – 300K.

been grown. Based solely on interpolation and extrapolation of the experimental data, taken at 300 K, an *x*-*y* diagram for quaternary 7-nm-thick $In_yGa_{1-y}N_xP_{1-x}$ quantum wells with 0%≤[N] ≤3% and 0%≤[In] ≤25% has been generated (Fig. 3.16). The solid lines in the diagram represent constant transition energy for 7-nm-thick InGaNP/GaP quantum wells. The solid squares are experimental data, determined from PL peak positions. The filled area at the bottom of the diagram represents InGaNP with an indirect bandgap. Adding either In or N converts GaP from indirect bandgap into direct bandgap, but adding nitrogen has a much stronger effect, since the transition occurs at about 0.4%,

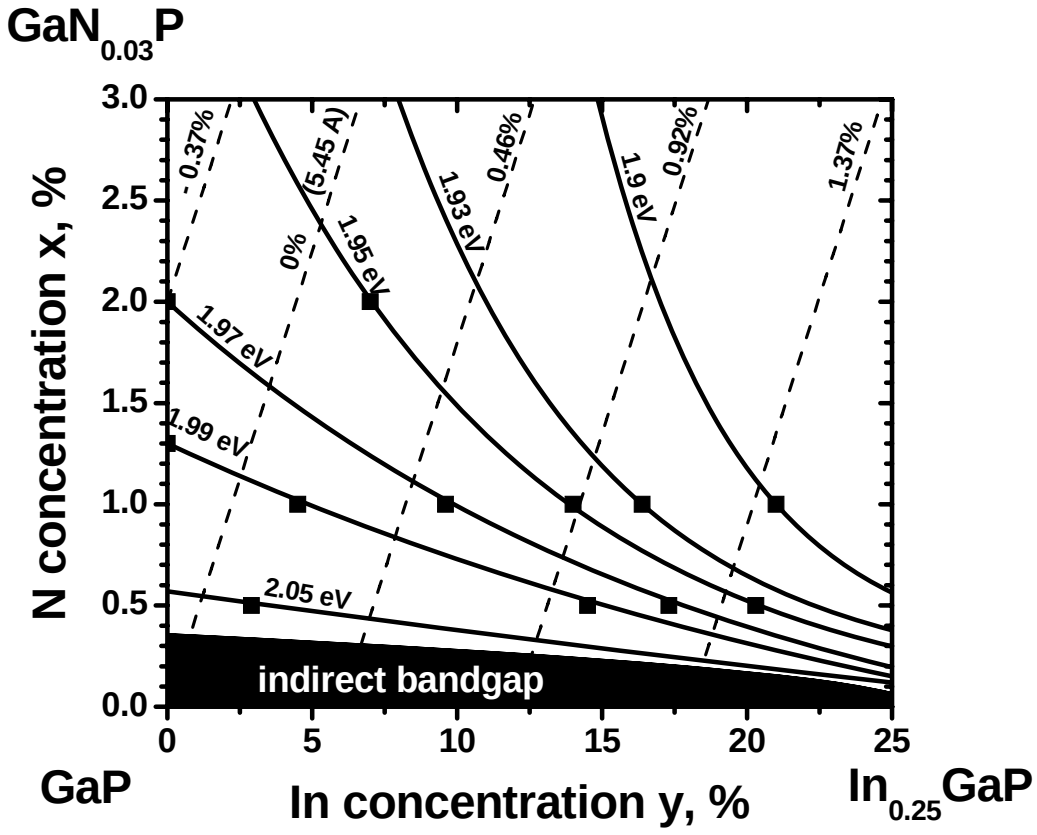

Figure 3.16. The x-y compositional plane for 7-nm-thick $In_yGa_{1-y}N_xP_{1-x}$ QW in GaP barriers at 300 K. Solid lines are constant direct-energy values; dashed lines are constant strain with respect to GaP; symbols are experimental data; and filled area is the indirect bandgap region of $In_yGa_{1-y}N_xP_{1-x}$ material.

compared to about 25% for adding indium. Increasing both nitrogen and indium concentrations in the quantum well leads to a red shift of the PL peak position. The diagram in Fig. 3.16 shows that by simultaneously changing the nitrogen and indium concentration in the quantum well, one can obtain the same transition energy. The dashed lines on the diagram represent constant strain in the quantum well with respect to GaP. The zero-strain line means lattice-matching condition. Using this diagram it is possible to construct a 7-nm-thick InGaNP quantum well emitting from yellow-amber to red, while keeping the strain small or equal to zero.

Temperature-dependent PL of a 7-nm-thick $In_{0.1}Ga_{0.9}N_{0.005}P_{0.995}$ quantum well is studied, and a difference in the behavior of the PL peak position with changing temperature as compared to the $GaN_{0.005}P_{0.995}$ QW is observed. Figure 3.17a shows temperature dependence of the transition energy for a 7-nm-thick $In_{0.1}Ga_{0.9}N_{0.005}P_{0.995}$ quantum well. The symbols are experimental data, and the solid curves are the best fit with the Varshni equation (3.1), where α and β are fitting parameters. Figure 3.17b shows corresponding PL spectra. One can see in Fig. 6a that the temperature dependence of the transition energy for the GaNP quantum well can be fit very well by Varshni equation with $\alpha=2.7\times10^{-4}$ eV/K and $\beta=140$ K. In contrast, the temperature dependence of the transition energy for the InGaNP quantum well (Figure 3.17a) deviates from the best Varshni fit ($\alpha=2.8\times10^{-4}$ eV/K and $\beta=110$ K) in the temperature range of 125 K to 290 K. The maximum deviation of 24 meV is observed at 260 K. We attribute this deviation to the clustering effect, which occur in InGaNP. This is due to partial phase separation, which may take place in quaternary InGaNP alloy, leading to formation of In-rich and N-

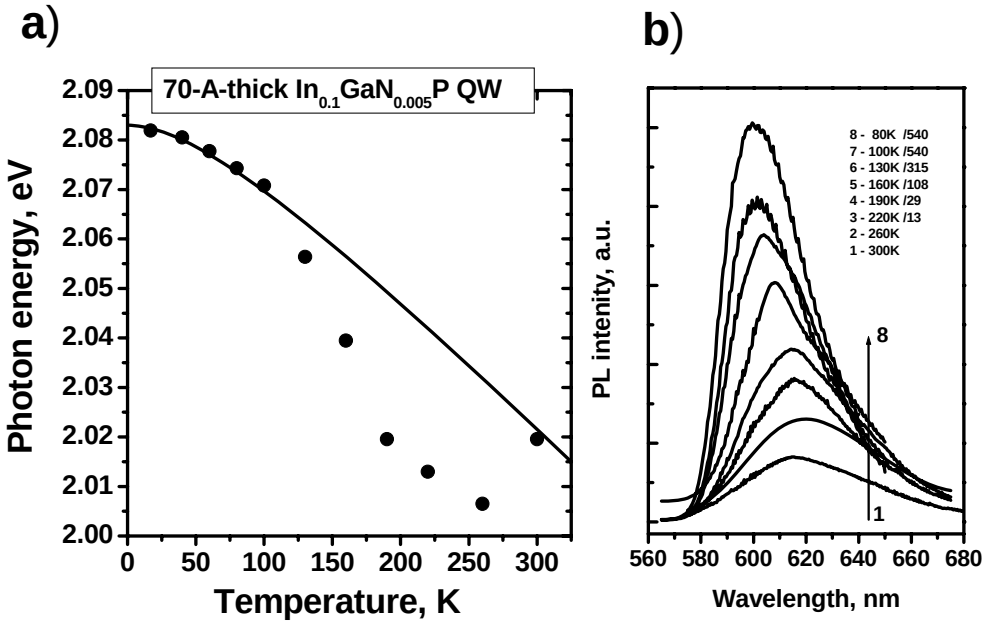

Figure 3.17. a) Dependence of the photon energy vs. temperature for 7-nm-thick $In_{0.1}GaN_{0.005}P$ QW. Symbols are experimental data, solid lines are the best Varshni fit; b) PL spectrums for the 7-nm-thick $In_{0.1}GaN_{0.005}P$ QW, taken at different temperatures.

rich areas, responsible for lower-energy emission in the range of 125 K to 290 K. Both GaNP and InGaNP QWs are grown at the same substrate temperature of 490^0C, which may be high enough to cause partial phase separation in the InGaNP alloy. Analogous effect was observed in $In_{0.3}Ga_{0.7}N_{0.02}As_{0.98}$/GaAs QWs[21]. Growth of high-crystal-quality quaternary InGaNP material may require lower substrate temperature (<450^0C) as compared to the GaNP material, to avoid formation of In-rich and N-rich areas in the alloy. Further optimization of the growth conditions (e.g. substrate temperature) of InGaNP quantum wells is required in order to minimize the effect of clustering on the optical properties of the structure.

3.4.3. Electron effective mass

In order to use InGaNP material system as an active region in LED structure, we need to study its fundamental properties. Electron effective mass is important for calculations of energy levels in the quantum wells, for minority carrier distribution in the LED structure, and for calculations of the current overflow in the quantum well. This paragraph is devoted to determination of the electron effective mass in $In_yGa_{1-y}N_{0.005}P_{0.995}$ with different y.

The dependence of transition energy vs. quantum well width, L, is studied for three sets of $In_yGa_{1-y}N_{0.005}P_{0.995}$ quantum wells with different indium concentration (5%, 10% and 20%). We use the infinite-barrier approximation for the conduction band, but assume no valence band offset. Since the effect of ~1% of nitrogen on the valence band of GaAs is negligible[22], we assume the same for GaP. The effect of indium on the valence band of GaP is also small[23]. We also neglect the effect of strain in the quantum well in our model. The infinite barrier approximation model has been used previously to determine the electron effective mass of InGaNAs[24] and GaNP[25]. According to the model, the energy positions of the quantum levels are determined from:

$$E_n = \frac{\pi^2 \hbar^2 n^2}{2mL^2} = \frac{376}{m_c^* L^2} \text{ (meV), } (L \text{ in nm}). \qquad (3.6).$$

Figure 3.18a shows the dependence of the QW transition energy vs. QW width. In order to use the model described by Equation 3.6, we re-plot the experimental dependence.

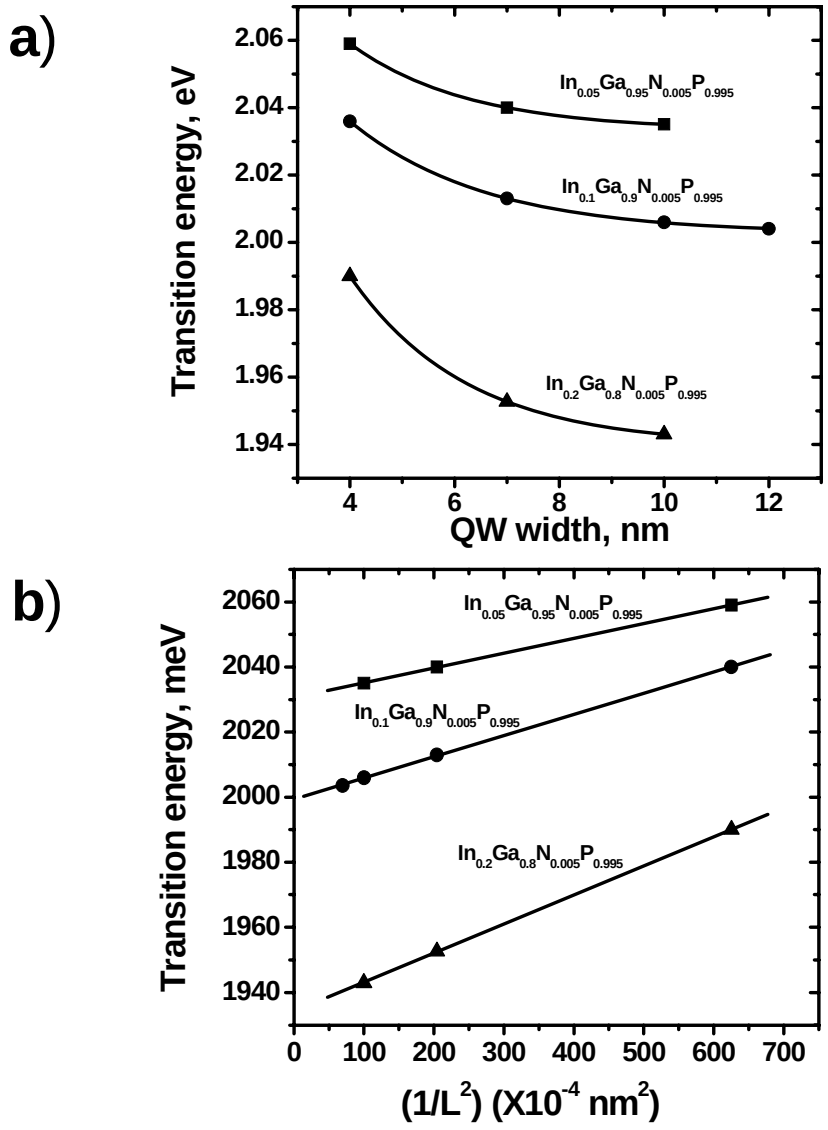

Figure 3.18. a) Dependence of the transition energy vs. quantum well width for $In_yGa_{1-y}N_{0.005}P_{0.995}$ QW with different indium concentrations: 5%, 10% and 20%; b) Dependence of the transition energy vs. inverse squared quantum well width for the QWs in a).

Figure 3.18b shows the dependence of the QW transition energy at room temperature vs. ($1/L^2$). The symbols are experimental data, and the solid lines are the best linear fits. Increasing the quantum well width leads to a red shift of the PL peak position, as expected. The linear fits are excellent, justifying our assumptions for the model. The electron effective mass m_c* can be extracted for $In_yGa_{1-y}N_{0.005}P_{0.995}$ with different indium concentrations. Figure 3.19 shows the dependence of the electron effective mass in $In_yGa_{1-y}N_{0.005}P_{0.995}$ alloy vs. indium concentration. The electron effective mass decreases from 0.77 m_e to 0.4 m_e, where m_e is the free electron mass, when the indium concentration is increased from 5% to 20%. This is expected, since InP has a lower electron effective mass than GaP.

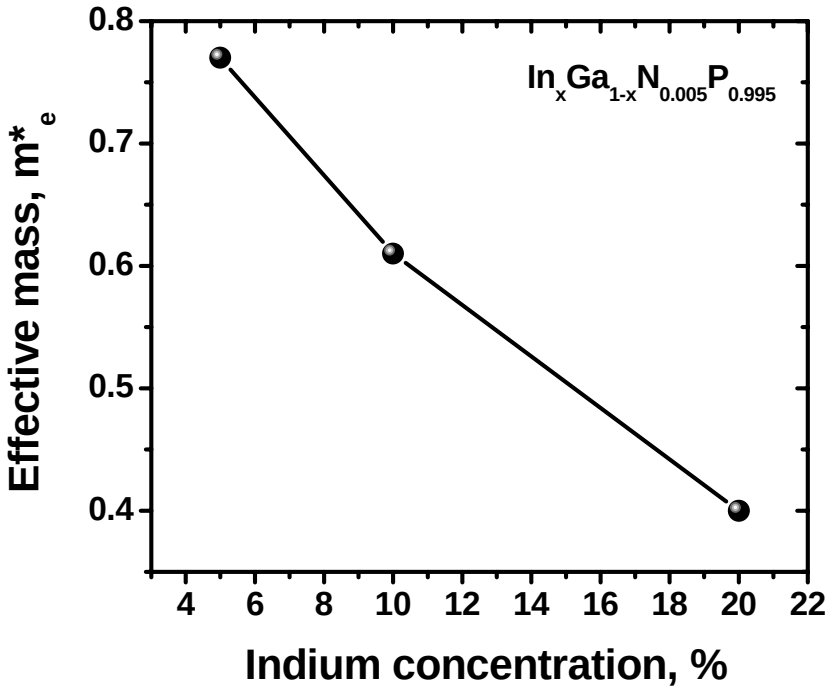

Figure 3.19. Dependence of the electron effective mass in $In_yGa_{1-y}N_{0.005}P_{0.995}$ vs. indium concentration.

We compare electron effective masses of InGaNP material and conventional AlInGaP material currently used for yellow-amber-red LEDs. For the considered bandgap range of 2.05 eV ≤ Eg ≤ 1.94 eV for $In_yGa_{1-y}N_{0.005}P_{0.995}$ material ($0.05 \leq y \leq 0.2$), the electron effective mass is in the range of $0.4\ m_e \leq m_{InGaNP}^* \leq 0.77\ m_e$.

For the same bandgap range for $(Al_zGa_{1-z})_{0.5}In_{0.5}P$ material, the electron effective mass is determined as follow[26]:

$$m^* = (0.092+0.146z)\ m_e \qquad (3.7).$$

According to Equation 3.7, calculated values of m* for $(Al_zGa_{1-z})_{0.5}In_{0.5}P$ in the bandgap range of $0.05 \leq z \leq 0.24$ are $0.1\ m_e \leq m_{AlGaInP}^* \leq 0.127\ m_e$. These values of electron effective mass are 4 to 6 times lower than that for InGaNP. This will result in a decrease of current overflow in InGaNP/GaP quantum wells, as compared to AlGaInP/AlInP QWs. Detailed discussion of this is given in Chapter 4.

3.4.4. InGaNP/GaP band offsets

Band offsets are very important parameters for an LED structure. They determine temperature stability of LED characteristics, e.g. internal quantum efficiency.

In this section we calculate band offsets of InGaNP/GaP heterojunction using Van de Walle's model-solid theory[27], with effects of hydrostatic strain taken into account. We determine the band-offsets of $In_{0.1}Ga_{0.9}N_{0.005}P_{0.995}$/GaP as an example. The bandgap of $In_{0.1}Ga_{0.9}N_{0.005}P_{0.995}$ material is 2 eV, as determined from PL (see section 3.4.2). By conduction band offset in the considered InGaNP/GaP heterojunction we mean the

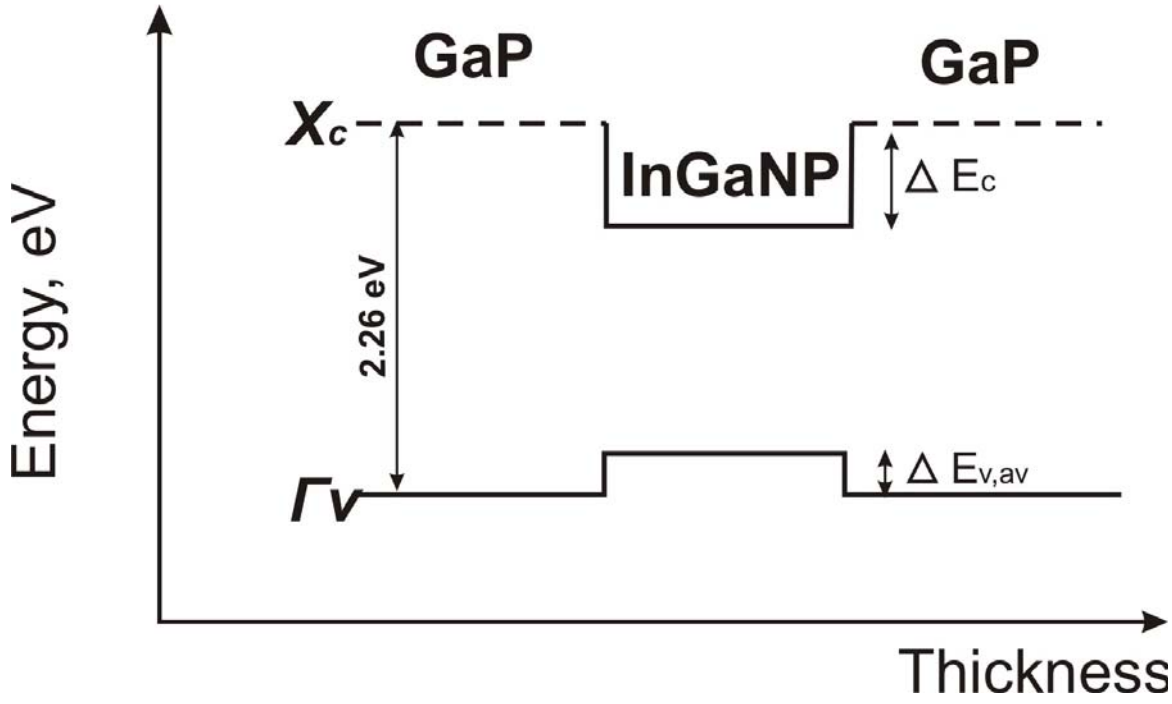

Figure 3.20. A band diagram of GaP/InGaNP/GaP double heterostructure.

energy distance between the *X*-valley in GaP and the *Γ*-valley in InGaNP (Fig. 3.20). First, we determine the valence band offset, $\Delta E_{v,av}$, then we determine the conduction band offset, ΔE_c as follow:

$$\Delta E_c = E_{g,GaP} - \Delta E_{v,av} \qquad (3.8).$$

$\Delta E_{v,av}$ here is the average over the three uppermost valence bands at Γ point (those three are light and heavy hole bands, and the spin-orbit split-off band, according to Ref. [27]).

Since we have a pseudomorphic $In_{0.1}Ga_{0.9}N_{0.005}P_{0.995}$ layer grown on GaP, the lattice constant, parallel to the growth interface, $a_{InGaNP,II}$, is equal to the GaP lattice constant:

$$a_{InGaNP,II} = a_{GaP} = 5.45 \text{ Å} \quad (3.9).$$

The lattice constant of $In_{0.1}Ga_{0.9}N_{0.005}P_{0.995}$ in the growth direction, $a_{InGaNP,\perp}$, is calculated using

$$a_{InGaNP,\perp} = a_{InGaNP}\,[1 - D_{InGaNP}(a_{II}/a_{InGaNP} - 1)] \quad (3.10),$$

where D_{InGaNP} is the constant, which depends on the elastic constants c_{11} and $c_{12,}$ and on the interface orientation.

According to Van de Walle's model, the strain tensor, $\vec{\varepsilon}$, needs to be derived:

$$\varepsilon_{InGaNP,II} = (a_{II}/a_{InGaNP} - 1) \quad (3.11),$$

$$\varepsilon_{InGaNP,\perp} = (a_{\perp}/a_{InGaNP} - 1) \quad (3.12),$$

where a_i's are equilibrium lattice constants.

We consider the (001) interface, for which

$$D^{001} = 2\,(c_{11}/\,c_{12}) \quad (3.13).$$

Using equations (3.9)-(3.13), data from Ref. [27], and linear interpolation for equilibrium lattice constant and elastic constants of $In_{0.1}Ga_{0.9}N_{0.005}P_{0.995}$ we find

$$\varepsilon_{InGaNP,II} = -0.0055 \quad (3.14),$$

$$\varepsilon_{InGaNP,\perp} = 0.005 \quad (3.15),$$

$$a_{InGaNP,\perp} = 5.5 \text{ Å} \quad (3.16).$$

The next step, according to Van de Walle, is to determine the $E_{v,av}$, which is the average over the three uppermost valence bands at Γ point. The $E_{v,av}$ is subject only to shifts due to the hydrostatic component of the strain (corresponding to a volume change). The hydrostatic deformation potential for the valence band is

$$a_v = \frac{dEv,av}{d\ln\Omega} \quad (3.17),$$

which expresses the shift in $E_{v,av}$ per unit fractional volume change, $\frac{\Delta\Omega}{\Omega}$. Then,

$$\Delta E_{v,\,av} = a_v \frac{\Delta\Omega}{\Omega} \quad (3.18),$$

where $\frac{\Delta\Omega}{\Omega} = \mathrm{Tr}\,(\vec{\varepsilon}\,) = (\varepsilon_{\,xx} + \varepsilon_{\,yy} + \varepsilon_{\,zz})$.

For $In_{0.1}Ga_{0.9}N_{0.005}P_{0.995}$ we calculated earlier

$$\varepsilon_{\,xx} = \varepsilon_{\,yy} = -0.0055 \quad (3.19),$$

$$\varepsilon_{\,zz} = 0.005 \quad (3.20),$$

which results in a volume change

$$\frac{\Delta\Omega}{\Omega} = -0.006 \quad (3.21).$$

The relation

$$E_{v,av} = E^{0}_{v,av} + a_v \frac{\Delta\Omega}{\Omega} \quad (3.22),$$

(based on equation 3.18) expresses $E_{v,av}$ in terms of its value in the unstrained material, $E^{0}_{v,av}$.

Using the data from Ref. [27], $\Delta E_{v,\,av}$ follows immediately:

$$E^{GaP}_{v,av} = -7.4 \text{ eV} \quad (3.23),$$

$$E^{InGaNP}_{v,av} = -7.364 - 1.657*0.006 = -7.37 \text{ eV} \quad (3.24).$$

This leads to

$$\Delta E_{v,\,av} = 0.03 \text{ eV} \quad (3.25),$$

$$\Delta E_c = E_{g,GaP} - \Delta E_{v,av} = 0.24 \text{ eV} \quad (3.26),$$

for the $In_{0.1}Ga_{0.9}N_{0.005}P_{0.995}$/GaP heterojunction.

The example listed above has been used to calculate $\Delta E_{v,\,av}$, and ΔE_c for $In_yGa_{1-y}N_{0.005}P_{0.995}$/GaP heterojunctions with $0 \leq y \leq 0.2$. Figure 3.21 shows the $In_yGa_{1-y}N_{0.005}P_{0.995}$/GaP band offsets vs. In concentration in the QW. Quantum size effect was not taken into account, since the electron and hole effective masses in $In_yGa_{1-y}N_{0.005}P_{0.995}$ are relatively large ($m^*_{e,h} > 0.5m_e$).

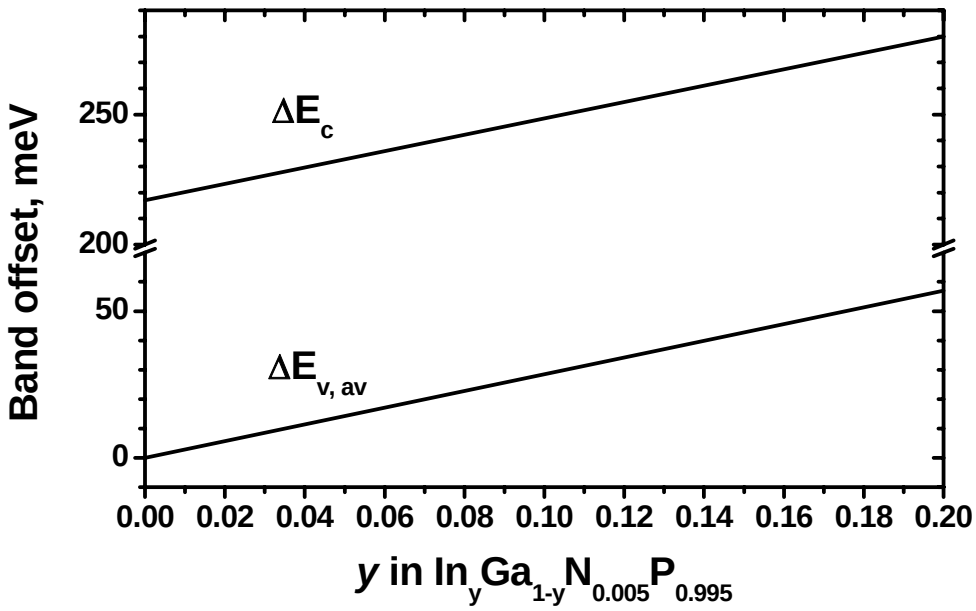

Figure 3.21. Calculated conduction and valence band offsets of GaP/$In_yGa_{1-y}N_{0.005}P_{0.995}$/GaP as a function of y.

3.5. Conclusion

In this chapter we have studied growth and characterization of (In,Al,Ga)NP material system grown directly on GaP (100) substrates by plasma-assisted GSMBE.

In particular, increasing the nitrogen composition in the GaNP bulk layers from 0.6 to 1.7% leads to light emission color from yellow-amber to red. An optimal growth temperature window of 500-520^{0}C for GaNP bulk layers is determined from analysis of their structural and optical properties. Temperature dependence of the PL peak position for 7-nm-thick $GaN_{0.005}P_{0.995}$ QWs agrees well with the Varshni equation.

Then, single-crystal AlGaNP layers with 0%<[Al]<100% are grown on GaP substrates. The difference in nitrogen incorporation into GaP and AlP has been determined (factor of 3.4). An equilibrium thermodynamic model, applied to the growth of AlGaNP, has qualitatively explained this difference. The Gibbs free energy released during the formation of AlN is larger than that of GaN. The best crystal quality (as determined from x-ray diffraction) of AlGaNP layers is achieved for an aluminum compositions of 80%<[Al]<100%, and the worst crystal quality is observed for [Al]=50%, as expected.

Finally, the optical properties of InGaNP quantum wells in GaP barriers are studied. Post-growth annealing of InGaNP QWs leads to higher PL intensity by a factor of 5 and a blue shift of the PL peak position by 2 nm. Emission color from yellow–amber to red can be realized using 7-nm-thick $In_yGa_{1-y}N_xP_{1-x}$ QWs, while lattice-matching condition of $In_yGa_{1-y}N_xP_{1-x}$ to GaP can be satisfied. Temperature dependence of the PL

peak position of the 7-nm-thick $In_{0.1}Ga_{0.9}N_{0.005}P_{0.995}$ QW deviates from the Varshni equation in the temperature range of 125 K to 290 K, most likely as a result of the clustering effect. The electron effective mass of the $In_yGa_{1-y}N_{0.005}P_{0.995}$ alloy decreases from 0.77 m_e to 0.4 m_e, when the indium concentration is increased from 5% to 20%. The conduction and valence band offsets of $In_yGa_{1-y}N_{0.005}P_{0.995}$/GaP heterojunction are calculated for $0 \leq y \leq 0.2$, using Van de Walle's model-solid theory. These will help in LED structure design.

Materials in this Chapter were partially published in Journal of Crystal Growth 279, 20 (2005), Journal of Vacuum Science and Technology B 23, 1317 (2005), Applied Physics Letters 88, 071907 (2006).

References:

[1] H. P. Xin, R. J. Welty and C. W. Tu, Appl. Phys. Lett. **77**, 1946 (2000).

[2] H. P. Xin, C. W. Tu, Y. Zhang and A. Mascarenhas, Appl. Phys. Lett. **76**, 1267 (2000).

[3] W. Shan, W. Walukiewicz, K. M. Yu, J. Wu, J. W. Ager III, E. E. Haller, H. P. Xin, C. W. Tu, Appl. Phys. Lett. **76**, 3251 (2000).

[4] I. A. Buyanova, G. Yu. Rudko, W. M. Chen, H. P. Xin, C. W. Tu, Appl. Phys. Lett. **80**, 1740 (2002).

[5] I. A. Buyanova, G. Pozina, J. P. Bergman, W. M. Chen, H. P. Xin, C. W. Tu, Appl. Phys. Lett. **81**, 52 (2002).

[6] G. Yu. Rudko, I. A. Buyanova, W. M. Chen, H. P. Xin, C. W. Tu, Appl. Phys. Lett. **81**, 3984 (2002).

[7] A. Yu. Egorov, E. S. Semenova, V. M. Ustinov, Y. G. Hong, and C. Tu, Semiconductors **36**, 981 (2002).

[8] J. W. Matthews and A. E. Blakeslee, J. Cryst. Growth **27**, 118 (1974).

[9] S. Shirakata, M. Kondow and T. Kitatani, Appl. Phys. Lett. **80**, 2087 (2002).

[10] W. G. Bi and C. W. Tu, Appl. Phys. Lett. **70**, 1608 (1997).

[11] D. G. Thomas and J. J. Hopfield, Phys. Rev. **150**, 680 (1966).

[12] K. Adomi, N. Noto, A. Nakamura, and T. Takenaka, Appl. Phys. Lett. **63**, 663 (1993).

[13] P. S. Kop'ev and N. N. Ledentsov, Sov. Phys. Semicond. **22**, 1093 (1988).

[14] A. Y. Egorov, A. R. Kovsh, A. E. Zhukov, V. M. Ustinov, and P. S. Kop'ev, Semiconductors **31**, 989 (1997).

[15] Y. Qiu, S. A. Nikishin, H. Temkin, V. A. Elyukhin, and Y. A. Kudriavtsev, Appl. Phys. Lett. **70**, 2831 (1997).

[16] V. A. Odnoblyudov, A. R. Kovsh, A. E. Zhukov, N. A. Maleev, E. S. Semenova, and V. M. Ustinov, Semiconductors **35**, 533 (2001).

[17] V. A. Odnoblyudov, A. Y. Egorov, A. R. Kovsh, A. E. Zhukov, N. A. Maleev, E. S. Semenova, and V. M. Ustinov, Semicond. Sci. Technol. **16**, 831 (2001).

---

[18] Y. Q. Wanga, Z. L. Wanga, T. Brown, A. Brown, and G. May, J. Cryst. Growth **242**, 5 (2002).

[19] A. Koukitu and H. Seki, Jpn. J. Appl. Phys., Part 2 **36**, L750 (1997).

[20] H. P. Xin, K. L. Kavanagh, M. Kondow, and C. W. Tu, J. Cryst. Growth **201**, 419 (1999).

[21] H.P. Xin, K.L. Kavanagh, and C.W. Tu, J. Cryst. Growth **208**, 145 (2000).

[22] W. Shan, W. Walukiewicz, J. W. Ager III, E.E. Haller, J. F. Geisz, D. J. Friedman, J. M. Olson, and S. R. Kurtz, Phys. Rev. Lett. **82**, 1221 (1999).

[23] S. Tiwari and D. J. Frank, Appl. Phys. Lett. **60**, 630 (1992).

[24] E. D. Jones, N. A. Modline, A. A. Allerman, I. J. Fritz, S. R. Kurtz, A. F. Wright, S. T. Tozer, and X. Wei, *Proceeding of the SPIE*, **52**, 3621 (1999).

[25] H. P. Xin and C. W. Tu, Appl. Phys. Lett. **77**, 2180 (2000).

[26] P. Raisch, R. Winterhoff, W. Wagner, M. Kessler, H. Schweizer, T. Riedl, R. Wirth, A. Hangleiter, and F. Scholz, Appl. Phys. Lett. **74**, 2158 (1999).

[27] C. G. Van De Walle, Phys. Rev. B **39**, 1871 (1989).

Chapter 4. (Al,In,Ga)NP-based light-emitting diodes.

4.1. Overview

This chapter is devoted to the growth, fabrication and characterization of (Al,In,Ga)NP – based light emitting diodes.

We describe step-by-step LED chip fabrication procedure and contacts optimization. *N*-type and *p*-type contacts are developed and LED chip fabrication is optimized on a *p*-*i*-*n* diode structure.

Growth details of different (Al,In,Ga)NP-based LED structures are described, and band offsets are compared for (Al,In,Ga)NP-based LED structures and AlInGaP-based LED structures.

Results on growth and fabrication of bulk GaNP-based amber LEDs are reported. Electroluminescence and current-voltage characteristics of 380 μm × 380 μm LED chips are studied for GaNP-based LEDs. Color stability - electroluminescence peak wavelength shift vs. current - is compared for GaNP-based LEDs and AlInGaP-based LEDs.

InGaNP QW-based LEDs are studied. Influence of In concentration in the QW on EL properties of LED chip is reported. Single and multiple InGaNP QW-based LED structures are also grown and characterized. Current overflow is compared for InGaNP QW-based LEDs and AlInGaP QW-based LEDs.

Finally, influence of AlGaP cladding layers on electrical and optical characteristics of InGaNP QW-based LED structures is studied in this chapter.

4.2. Fabrication of (Al,In,Ga)NP LED chips

This section overviews fabrication steps of LED chips from grown LED wafers. General step sequence is given with details of each processing step, and *n*-type and *p*-type contacts optimization is described.

4.2.1. General procedures

Pieces of grown LED wafers with dimensions of 1 cm × 1 cm (sample) are used for processing. Processing equipment (e-beam evaporator, thermal evaporator, RTA, KSM, etc.) is described in Chapter 2.4. The following steps are used in the fabrication:

1. Clean the bottom of the substrate for depositing *n*-type contact, with Tetrachloroethylene (TCE), Acetone (ACE), and Isopropyl Alcohol (IPA) in the given sequence.
2. Bake the sample in an oven for 3 minutes at 105^0C to evaporate moisture.
3. Use Buffer Oxide Etch for 30 sec to etch the oxide on the GaP wafer.
4. Deposit the following layers in the e-beam evaporator with a growth rate of 1 Å/s: 100 Å of Ge, 500 Å of Au, 100 Å of Ni, and 1000 Å of Au.

5. Clean the top of the substrate for depositing *p*-type contact, with TCE, Acetone, and IPA in the given sequence.
6. Spin S 1818 photo resist onto the top of the sample at 4000 rpm for 40 sec.
7. Bake the sample with photo resist in the oven for 1 minute at 105^0C.
8. Use a photo mask with circular 180-μm-diameter features to expose photo resist under UV light in the Karl Seuss microscope.
9. Develop the photo resist in PLSI developer solution for 1 minute.
10. Use Buffer Oxide Etch for 30 sec to etch the oxide in the developed areas of the sample surface.
11. Use thermal evaporator to deposit 1500 Å of $Au_{0.9}Zn_{0.1}$ at a growth rate of 1 Å/s.
12. Lift-off the AuZn layer in acetone. Circular AuZn contacts are left on the sample.
13. Use Rapid Thermal Annealing (RTA) to anneal the sample with deposited *p*-type contact at 370^0C for 30 sec in nitrogen atmosphere.
14. Dice the wafer into individual chips (~ 380 × 380 μm).
15. (*Optional*) Mount the chip on a TO can, and wire bond the top contact to a lead.
16. (*Optional*) Dip the TO can with mounted chip into melted epoxy to form an epoxy dome, and let it freeze.

AuZn and Ge/Au/Ni/Au metal contacts are used in the fabrication of an LED chips, following the earlier work[1] by H. P. Xin, R. J. Welty, and C. W. Tu.

4.2.2. Contacts optimization

The above described contact fabrication steps have to be optimized before utilizing the procedure for LED chip fabrication. The first step is to make sure that both *n*- and *p*-type contacts are ohmic.

In order to check if an *n*-type contact is ohmic we use a piece of *n*-type GaP substrate (S-doped) with free carrier concentration of $5*10^{17}$ cm^{-3}. Steps 5-10 from section 4.2.1 are performed, followed by step 4 (e-beam), then by lift-off of the Ge/Au/Ni/Au and step 13 (RTA). The result of the described steps is to form *n*-type 180-μm-diameter circular Ge/Au/Ni/Au contacts on the substrate surface. Figure 4.1a shows a

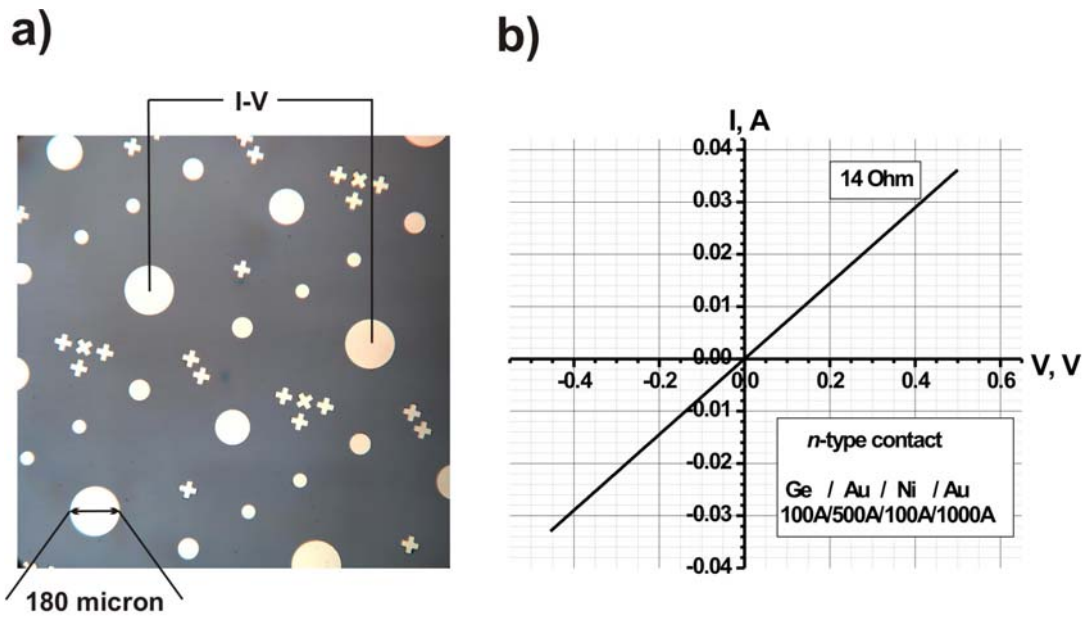

Figure 4.1. a) Micrograph of the *n*-type metal contacts, deposited on a GaP substrate; b) I-V characteristic, recorded between two *n*-type contacts.

photograph of a GaP substrate with deposited metal contacts, taken under an optical microscope. All the metal features are of good shape, with sharp borders. The largest circular features (180-μm-diameter) are used as contacts, and the other features are used for mask alignment. Current – voltage (I-V) characteristics are measured between the contacts (see Fig. 4.1a). Figure 4.1b shows the result of I-V measurements. As the I-V dependence is a straight line, we conclude that the Ge/Au/Ni/Au contact is ohmic. The measured series resistance of this configuration is 14 Ohm.

Similar procedure is performed to check if a *p*-type contact is ohmic. A special sample is grown to make a *p*-type contact, since no *p*-type doped or semi-insulating GaP substrate is available. The sample consists of a GaP *n*-type substrate, a 3-μm-thick undoped GaP buffer layer, and a 0.5-μm-thick GaP *p*-type (Be) $5*10^{19}$ heavily doped contact layer. The reason for introducing the thick undoped GaP layer is to separate the *n*-type substrate and *p*-type contact layer and make sure that the current between the metal contacts is conducted through the *p*-type layer only. AuZn circular metal contacts are formed on top of the grown *p*-type GaP layer, following steps 5-14 from section 4.2.1. A photograph of the sample with p-type contacts is shown in Fig. 4.2a. One can see that the visual quality of *p*-type contacts is much worse than that of *n*-type contact. Figure 4.2b shows corresponding I-V between two metal contacts. It is ohmic, but the measured series resistance of this configuration is 250 Ohm, which is much higher than the one for *n*-type contact (14 Ohm). There are several reasons for the series resistance to be higher for *p*-type contact.

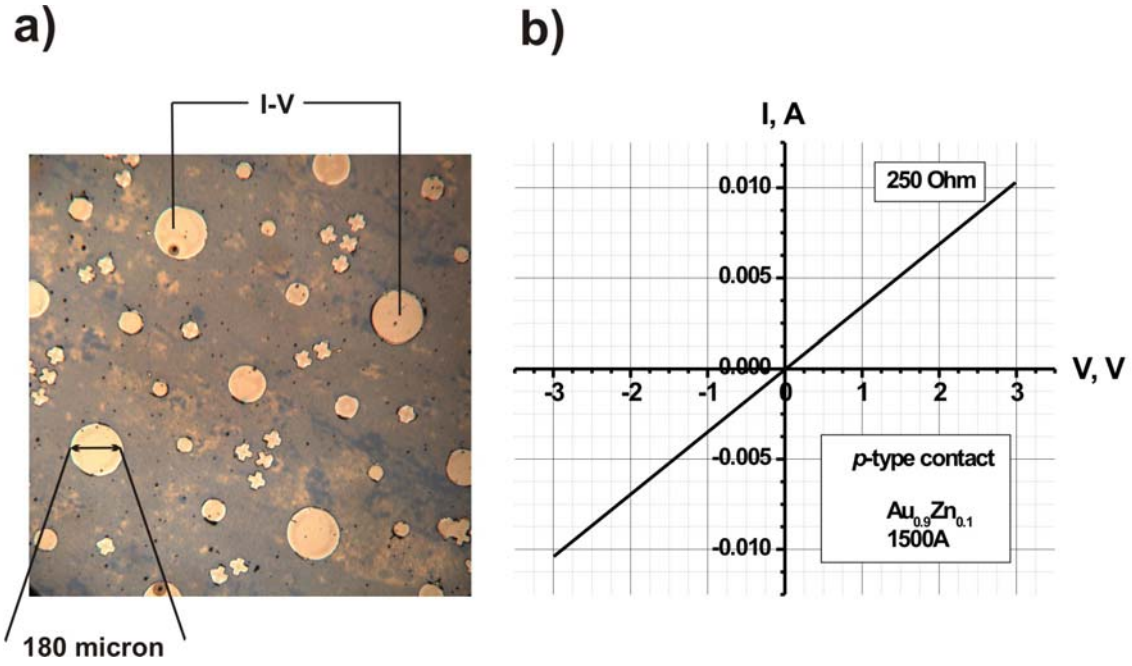

Figure 4.2. a) Micrograph of the p-type metal contacts, deposited on a p-type GaP contact layer; b) I-V characteristic, recorded between two *p*-type contacts.

First, the *n*-type contact is formed on a polished GaP substrate, and *p*-type contact is formed on a grown 3.5-μm-thick layer, which has a much rougher surface and many more surface growth defects (this can be clearly seen if we compare photographs in Fig. 4.1a and Fig. 4.2a). The surface roughness is due to the heavy Be doping. Be tends to segregate from the grown film, and the substrate temperature has to be lowered to about 550^0C for the growth of GaP:Be, as compared to 640^0C for growth of undoped GaP layer. Lowering the substrate temperature results in roughening of the surface.

Second, the hole mobility in Be-doped ($5*10^{19}$) GaP layer is about 8 cm^2/Vs, compared to ~ 100 cm^2/Vs for electron mobility in a GaP:S substrate. The hole mobility and concentration are determined by measuring Hall effect in a series of GaP:Be samples

with different levels of Be doping. Figure 4.3 shows the dependence of free hole concentration vs. hole mobility for a series of GaP:Be samples, the symbols representing experimental data. The electron mobility and free carrier concentration for GaP:S substrates are taken from substrate specifications. As hole mobility is much lower than electron mobility, the series resistance should be higher for *p*-type GaP contacts compared to *n*-type GaP contacts.

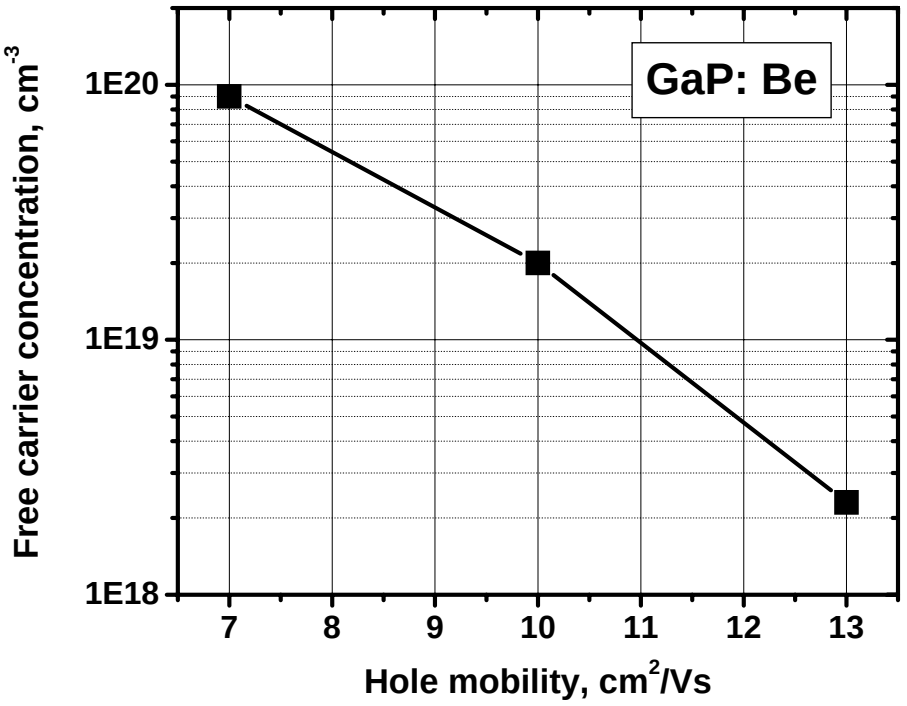

Figure 4.3. Dependence of the free carrier concentration on the hole mobility in p-type GaP layer.

Third, the *p*-type GaP layer, which conducts current between p-type AuZn contacts is thin (0.5 μm) compared to *n*-type GaP layer (the whole *n*-type substrate). A thinner layer has a higher series resistance.

To conclude, *n*-type contact has a much lower series resistance than *p*-type contact, but both contacts are ohmic, and, thus, suitable for fabrication of diodes.

After *n*- and *p*-type contacts are tested for ohmicity separately, it is important to check how they would work together in a GaP *p*-*i*-*n* diode, which has no light-emitting active layer, but *n*- and *p*-type GaP layers with thicknesses and doping concentrations, similar to the real LED structure. The RTA procedure is optimized on this *p*-*i*-*n* diode as well.

A schematic of a *p*-*i*-*n* diode structure is shown in Fig. 4.4a. It consists of an *n*-type GaP (100) substrate, a 0.3-μm-thick *n*-type GaP buffer layer, a 0.3-μm-thick GaP undoped layer, a 0.3-μm-thick *p*-type GaP layer, and a 0.5-μm-thick *p*-type GaP contact layer. Pieces of the grown *p*-*i*-*n* diode wafer are processed to form Ge/Au/Ni/Au *n*-type and AuZn *p*-type contacts, following the fabrication steps 1-12 from the previous section. The processed wafer is cleaved into smaller square pieces (~ 3 mm × 3 mm). Different RTA procedures are performed with each of the pieces. One piece (#1) is left without RTA for comparison. The positive effect on the I-V characteristics of *p*-*i*-*n* diode is achieved when using 370^0C RTA temperature. Figure 4.4b shows I-V's of the 4 samples: #1, #2, #3, and #4. Samples #2-4 are annealed at 370^0C for 1 min 30 sec, 1 min, and 30 sec, consequently. The I-V's are measured on-wafer, without dicing into individual chips. The copper plate in a probe station is used as the negative electrode, and the needle probe is placed on a AuZn circular 180-μm-diameter feature as the positive electrode. All four I-V's show a diode behavior. One can see from Fig. 4.4b that the lowest series resistance, 12 Ohm (determined from the slope of I-V's positive linear area), is achieved on a sample

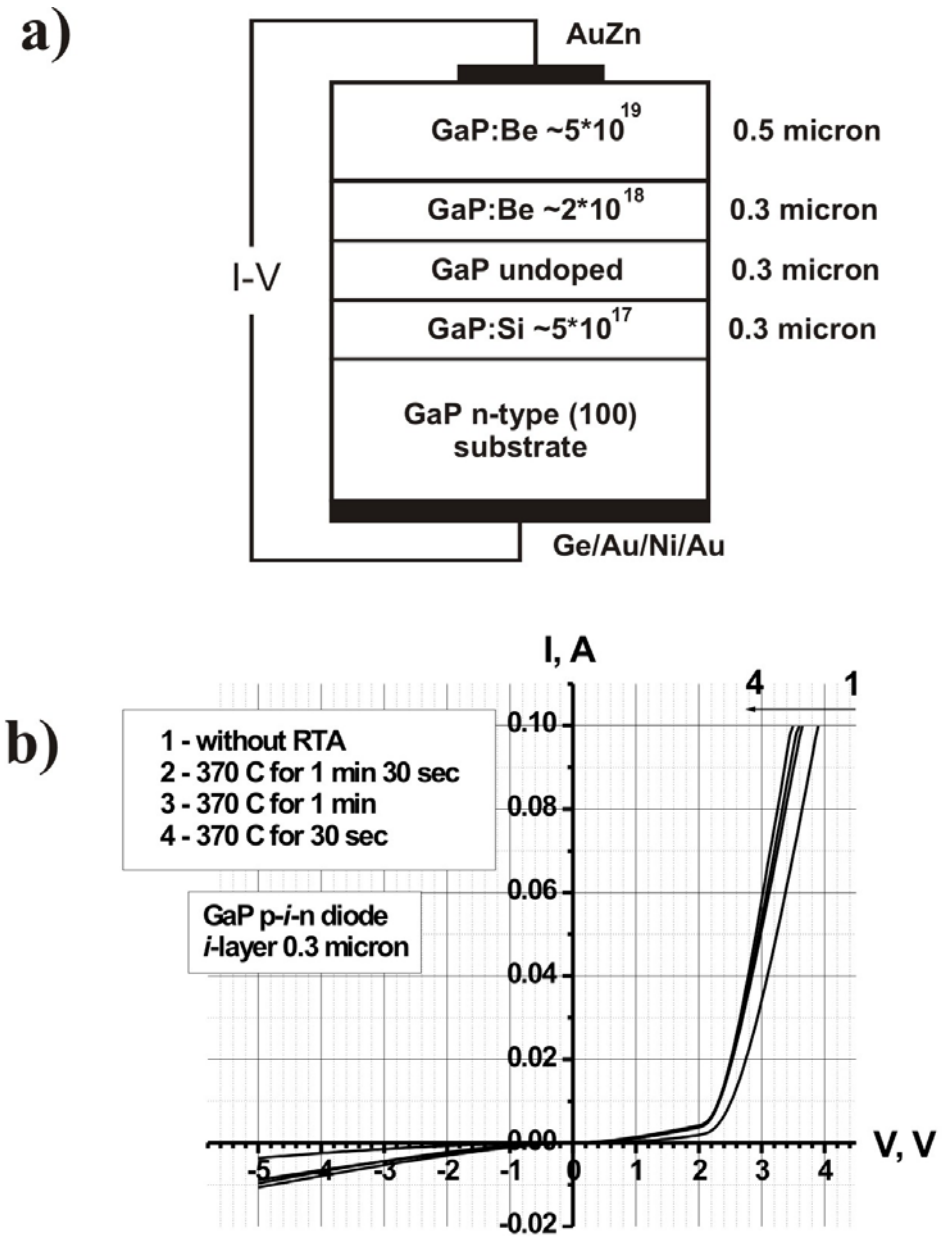

Figure 4.4. a) Schematic of the p-i-n diode structure; b) on-wafer I-V characteristics of the *p-i-n* diode structure with different RTA time.

with 30 sec RTA. The offset voltage for the Sample #1 (2.5 V) is higher than the offset voltage for Samples #2, #3, and #4 (2.27 eV). The offset voltage of samples with RTA (#2, #3, and #4) is close to the bandgap of GaP. This demonstrates that no voltage drop is

observed in the semiconductor-metal contact interface. Fig. 4.4b only shows the results of a series of the samples with 370^0C RTA. RTA temperatures higher than 380^0C (up to 450^0C tested) result in higher series resistance, as compared to Sample #1. This is probably due to deep penetration of the AuZn contact into 0.5-μm-thick GaP:Be contact layer at higher temperatures, which may result in punch through of the metal contact. RTA temperatures lower than 360^0C (as low as 280^0C) result in little or no effect on the *p-i-n* diode's I-V characteristics. This is because the temperature from this range is not sufficient to cause alloying of the semiconductor and metal contact.

This concludes the section about contact optimization. *P-i-n* diodes are successfully grown and fabricated; RTA procedure for the contacts is optimized. Satisfactory diode I-V characteristics are achieved, and contact fabrication procedure can be used for LED chip processing.

4.3. Band offsets of (Al,In,Ga)NP and AlInGaP LED structures

In this section we compare band offsets of conventional AlInGaP-based LEDs with our (Al,In,Ga)NP-based LEDs. We determine conduction and valence band offsets of AlInGaP-based LEDs first.

Figure 4.5[2] shows the energy distance between different valleys of the conduction band and the valence band vs. Al concentration in the active region for the $Al_{0.5}In_{0.5}P$ / $(Al_xGa_{1-x})_{0.5}In_{0.5}P$ / $Al_{0.5}In_{0.5}P$ LED structure, which is shown in the inset of Fig. 4.5.

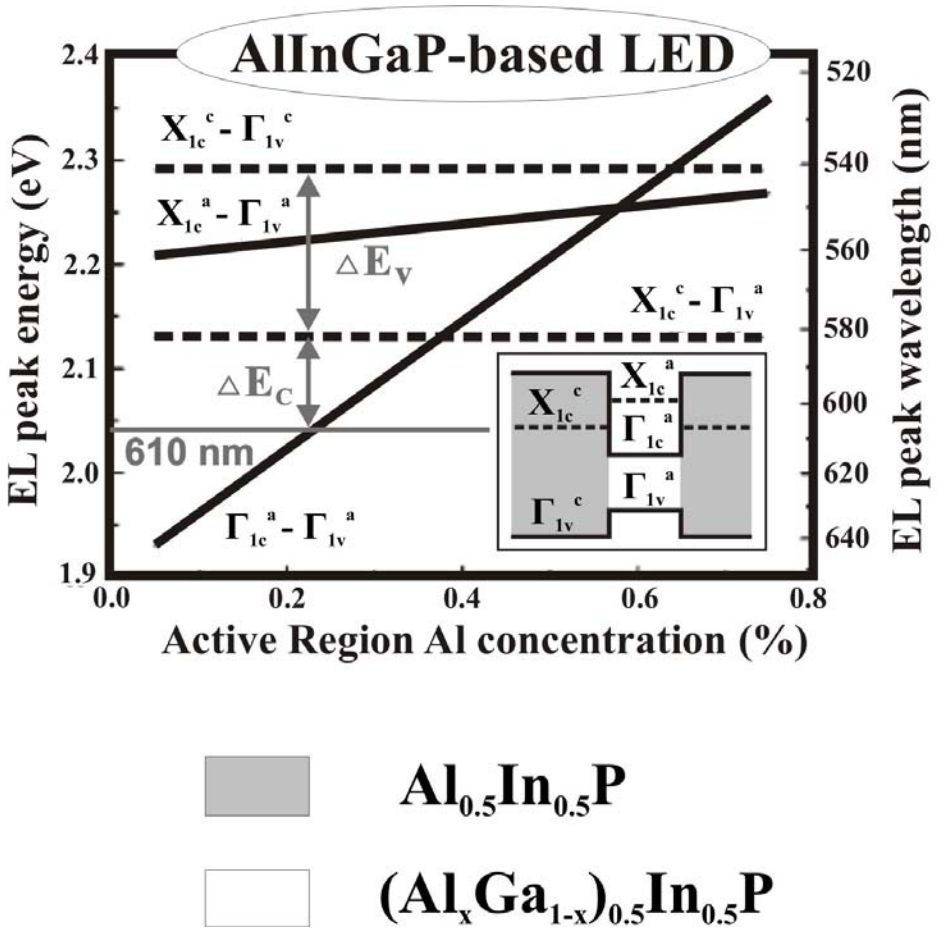

Figure 4.5. Dependence of the EL peak energy vs. Al concentration in AlInGaP-based LEDs.

$Al_{0.5}In_{0.5}P$ is the cladding layers, and $(Al_xGa_{1-x})_{0.5}In_{0.5}P$ is the bulk active region. By conduction band offset we mean the energy distance between X_{1c}^{c} of the cladding layers and Γ_{1c}^{a} of the active region, and by valence band offset we mean the energy distance between Γ_{1v}^{c} and Γ_{1v}^{a}. To determine band offsets, we first fix the wavelength (610 nm, see Fig. 4.5). Then, the conduction band offset is determined as the energy distance between $(X_{1c}^{c} - \Gamma_{1v}^{a})$ and $(\Gamma_{1c}^{a} - \Gamma_{1v}^{a})$:

$$\Delta E_{C,AlInGaP} = (X_{1c}^{c} - \Gamma_{1v}^{a}) - (\Gamma_{1c}^{a} - \Gamma_{1v}^{a}) = X_{1c}^{c} - \Gamma_{1c}^{a} = 75 \text{ meV} \qquad (4.1).$$

The valence band offset is the energy distance between (X_{1c}^{c} - Γ_{1v}^{c}) and (X_{1c}^{c} - Γ_{1v}^{a}):

$$\Delta E_{V,AlInGaP} = (X_{1c}^{c} - \Gamma_{1v}^{c}) - (X_{1c}^{c} - \Gamma_{1v}^{a}) = \Gamma_{1v}^{a} - \Gamma_{1v}^{c} = 150 \text{ meV} \qquad (4.2).$$

We will compare the calculated band offsets of AlInGaP-based LEDs with band offsets of bulk GaNP-based LEDs with $Al_{0.3}Ga_{0.7}P$ claddings. Fig 4.6 shows a band diagram of a bulk GaNP-based LED structure with $Al_{0.3}Ga_{0.7}P$ claddings. All the layers of the GaNP-

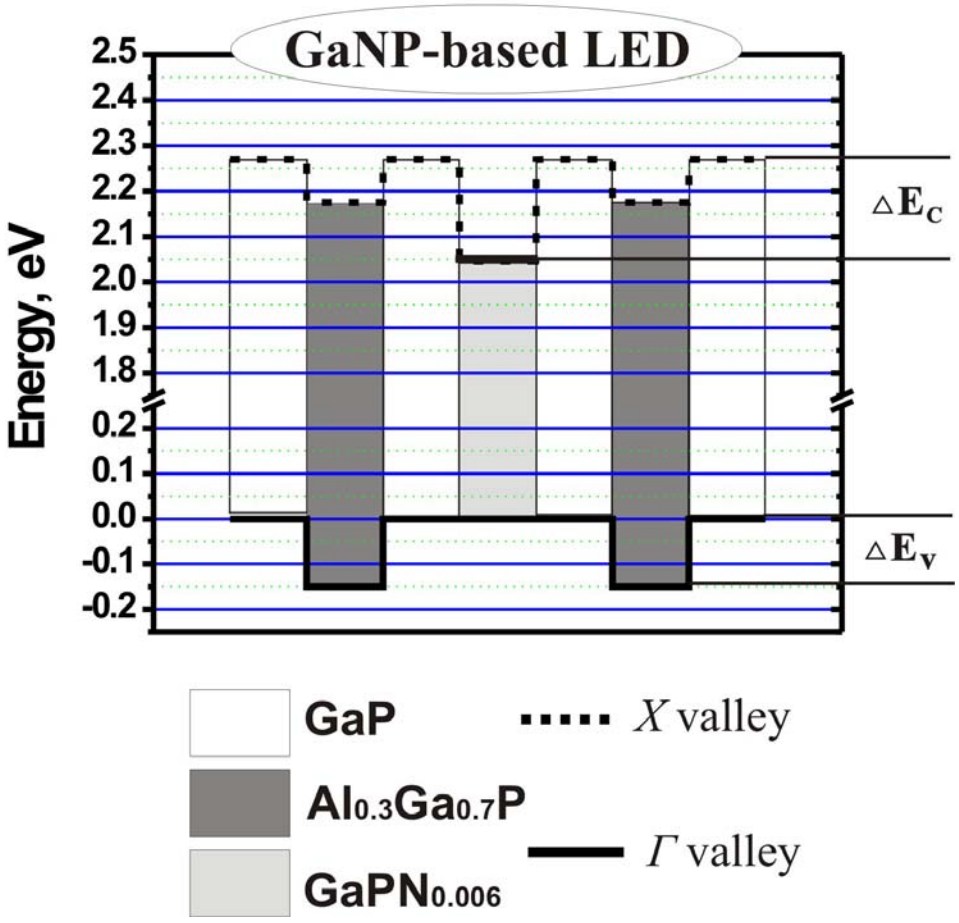

Figure 4.6. Band diagram of a GaNP-based LED.

based LED structures are indirect band gap and transparent for the emitted light, except the GaNP active layer, which has a direct band gap. The conduction band offset is the

energy distance between the X-valley in GaP and the Γ-valley in the GaNP layer. The valence band offset is the energy distance between Γ-valleys of GaP (GaNP) and $Al_{0.3}Ga_{0.7}P$ (see Fig. 4.6). Since ~ 2% of nitrogen has little influence on the valence band of GaP (similar to the effect on the valence band of GaAs[3]), the conduction band offset is the difference of band gaps of GaP and GaNP. As we compare the wavelength emission of 610 nm, the conduction band offset follows immediately:

$$\Delta E_{C,GaNP} = E_{g,GaP} - E_{g,GaNP}(610nm) = 227 \text{ meV} \quad (4.3).$$

The valence band offset is calculated based on Ref. [4]:

$$\Delta E_{V,GaNP} = 150 \text{ meV} \quad (4.4).$$

Thus, the conduction band offset is 3 times larger for GaNP-based LEDs (227 meV) emitting at 610 nm, as compared to AlInGaP-based LEDs (75 meV). The valence band offsets are the same for both kinds of LED structures (150 meV), when using $Al_{0.3}Ga_{0.7}P$ claddings in GaNP-based LEDs. The valence band offset may be increased up to 500 meV for GaNP-based LED structure, if AlP claddings are used (Ref. [4]). In this case both conduction and valence band offsets would be 3 times larger for GaNP-based LEDs, although the use of the high Al concentrations (> 35%) in the cladding layers is not desirable due to expected increase of the series resistance of the LED structure. Adding indium into GaNP will increase valence band offset between GaP and GaNP, according to calculations in section 3.4.4, which will result in an increase of total valence band offset between InGaNP and AlGaP cladding layers.

The larger band offsets of GaNP-based LED structures as compared to AlInGaP-based LED structures should provide higher internal quantum efficiency at higher current densities and/or at higher temperatures.

4.4. LED growth details

This section describes the details of different LED structures grown and corresponding growth conditions.

All LED structures are grown on GaP (100) *n*-type doped substrates, polished on one side and etched on the other side. The etching of the back side of the substrate is used to increase the heat absorption from the substrate heater during growth. Undoped GaP layers and Si-doped GaP and AlGaP layers are grown at 640^0C, and Be-doped GaP and AlGaP layers are grown at 550^0C to prevent Be segregation from the epi-layers. The GaNP or InGaNP active layers are grown at 480-500^0C. The GaP growth rate range of 0.5-2.3 Å/s, the AlP growth rate range of 0.4-1.8 Å/s, and the InP growth rate of 0.25 Å/s are used. A typical total group V / total group III beam equivalent pressure ratio of 3-4 is used during growth. Si is used as *n*-type dopant, and Be is used as *p*-type dopant in GaP and AlGaP layers. Typical nitrogen plasma source conditions are 0.3 sccm for nitrogen flux, and 250 W for RF power, which correspond to a nitrogen plasma optical intensity of 130 a.u.

Three different types of LED structures are studied. The first type is GaNP-based LEDs. These LEDs use a GaNP bulk layer (0.05 μm - 0.2 μm) as the active layer for light emission. The second type of LED structures is InGaNP QW-based LEDs. These LEDs use single and multiple QWs as the active layer(s) for light-emission. The third type of the LED structures is InGaNP single QW-based LEDs with AlGaP cladding layers. Figure 4.7 shows a schematic of the three types of LED structures studied.

A schematic of a generic GaNP-based LED structure is shown in Fig. 4.7a. It consists of a GaP (100) *n*-type substrate, a Si-doped (~ $5*10^{17}$ cm^3) 0.3-μm-thick GaP buffer layer, a 0.35-μm-thick undoped active region, a 0.3-μm-thick Be-doped GaP layer, and a 0.5-μm-thick heavily Be-doped (~ $5*10^{19}$) GaP contact layer. The active region consists of a GaNP active layer sandwiched between GaP waveguide layers.

Fig. 4.7b shows a schematic of a generic InGaNP QW-based LED structure. The structure is similar to the GaNP-based LED structure (Fig. 4.7a), with the only difference in the active region. A 0.35-μm-thick active region consists of $In_yGa_{1-y}N_{0.005}P_{0.995}$ ($0<y<0.2$) single or multiple QWs, sandwiched between GaP waveguide layers. In case of the multiple QW configuration, 100-Å-thick $In_yGa_{1-y}N_{0.005}P_{0.995}$ QW layers are separated by a 300-Å-thick GaP spacer layers.

Fig. 4.7c shows a schematic of a generic InGaNP QW-based LED structure with AlGaP cladding layers. It consists of a GaP (100) *n*-type substrate, a Si-doped (~ $5*10^{17}$ cm^3) 0.3-μm-thick GaP buffer layer, a Si-doped (~ $4*10^{17}$ cm^3) 0.5-μm-thick $Al_xGa_{1-x}P$ ($0<x<0.77$) bottom cladding layer, a 0.35-μm-thick undoped active region, a Be-doped (~ $5*10^{17}$ cm^3) 0.5-μm-thick $Al_xGa_{1-x}P$ top cladding layer, and a 0.5-μm-thick heavily

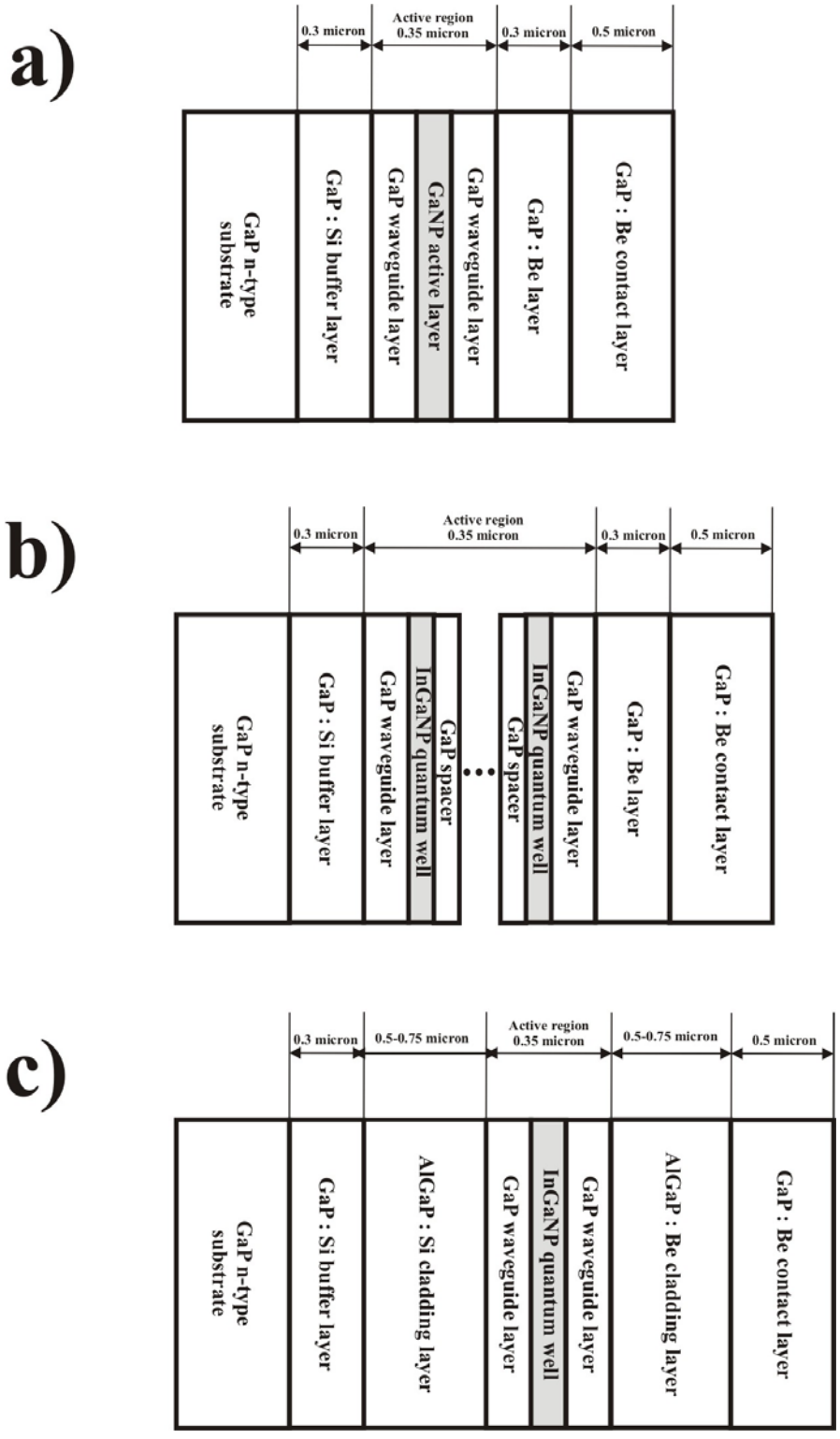

Figure 4.7. Different types of LED structures studied: a) bulk GaNP - based LED; b) InGaNP single or multiple QW – based LED; c) InGaNP single QW – based LED with AlGaP cladding layers.

Be-doped (~ $5*10^{19}$) GaP contact layer. The active region for this LED structure consists of a 100-Å-thick $In_{0.1}Ga_{0.9}N_{0.005}P_{0.995}$ single QW sandwiched between GaP waveguide layers. It is important to notice that all interfaces between GaP and AlGaP are δ-doped to reduce the potential barrier for carriers. δ-doping is done by keeping the Si or Be (depending on the interface) source shutter open for 1 min between the GaP and AlGaP layer growth.

The active region thickness (0.35 μm) is the same for all types of LED structures studied. It is also close to the thickness of the undoped layer (0.3 μm) in *p-i-n* diode structure, discussed in the previous section. The active region thickness (active layers + waveguide layers thickness) may influence I-V and light output characteristics of an LED chip. The active layer thickness is kept the same for all types of LED structures for consistency and direct comparison of the measurement results. The same approach is taken for the doping profile. It influences on the electrical and light output characteristics of an LED as well, so the doping profile (electron and hole concentrations in different layers) are kept the same for all types of the LED structures studied.

4.5. LEDs with a bulk GaNP active layer

This section devoted to fabrication and characterization of GaNP-based LEDs. We study electroluminescence and I-V characteristics of the GaNP-based LEDs, and compare the color stability of GaNP-based LEDs and AlInGaP-based LEDs.

4.5.1. LED chip characterization

The series of three LED structures, shown in Fig. 4.7a, with different active regions are grown for a study: a GaP/$GaN_{0.006}P_{0.994}$/GaP active region with GaNP thicknesses of 0.05, 0.1 and 0.2 μm. The total active region thickness is kept the same for all the LED structures grown. LED chips are fabricated according to steps 1-14 in section 4.2.1. A sample picture of the processed LED chip (top view) is shown in Fig. 4.8.

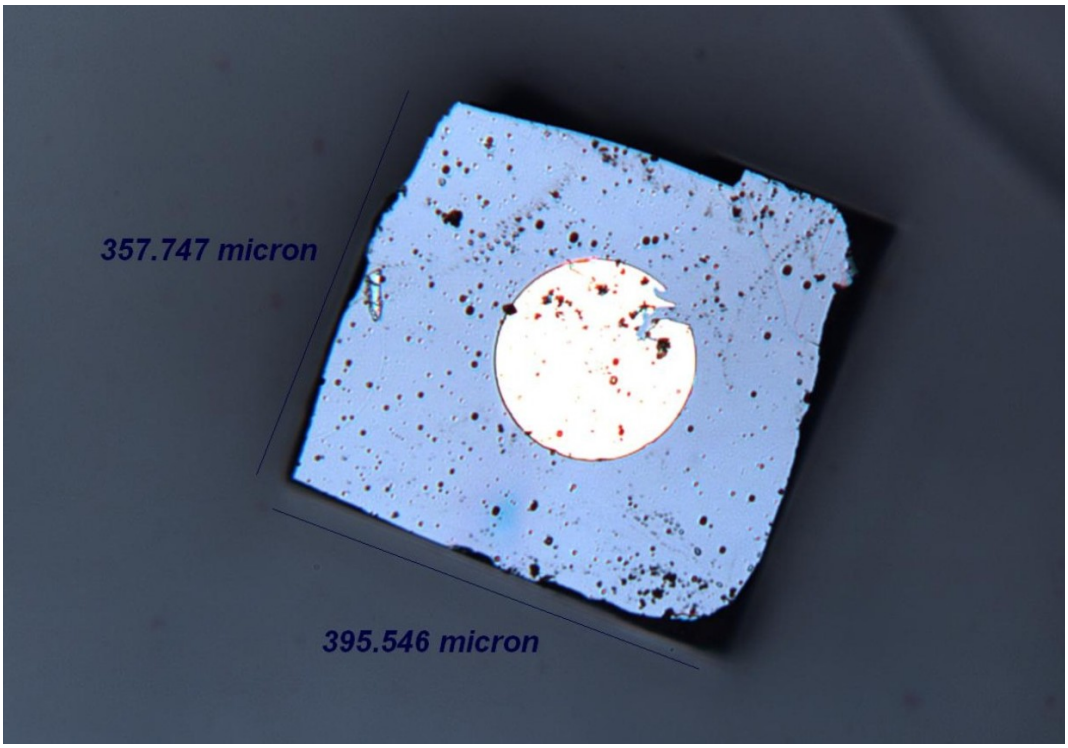

Figure 4.8. LED chip micrograph, taken under optical microscope.

Figure 4.9 shows room-temperature electroluminescence (EL) spectra at different drive currents of the LED chip with a 0.1-μm-thick GaNP active layer. The EL peak is at

612 nm and the EL intensity increases with drive current up to 50 mA. The emission color of the LED can be simply changed from yellow to red by increasing the nitrogen composition in the active region[5].

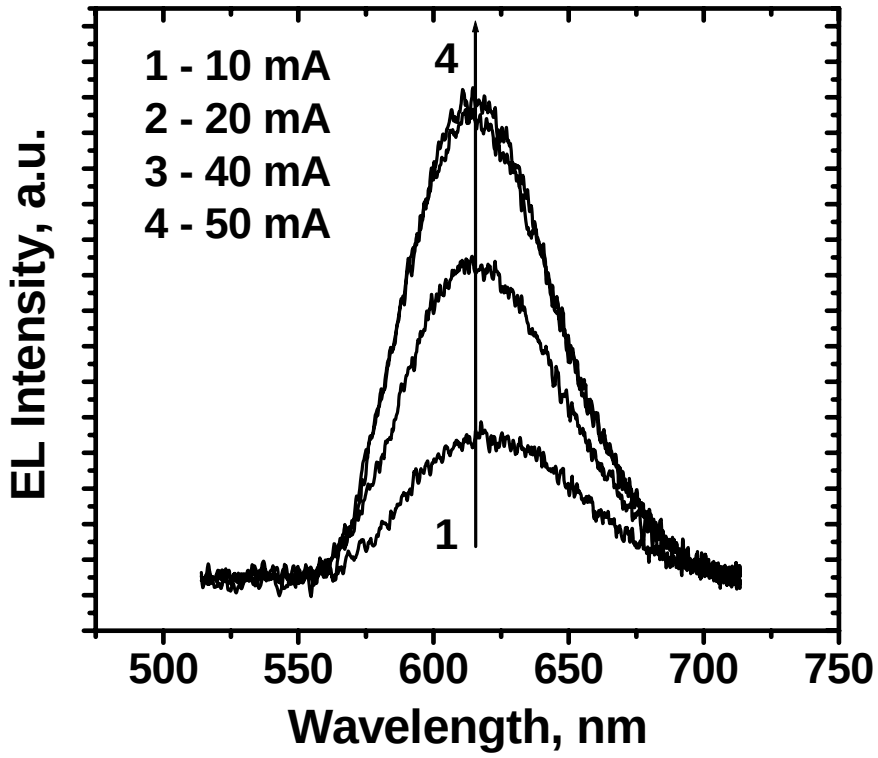

Figure 4.9. Electroluminescence spectra at different drive currents of a 380 μm × 380 μm LED chip with a 0.1-μm-thick $GaN_{0.006}P_{0.994}$ active layer.

Figure 4.10a shows the dependence of EL peak intensity on drive current for three LEDs with three different active layer thicknesses. One can see that decreasing the GaNP thickness from 0.2 μm to 0.05 μm increases the maximum EL intensity. Figure 4.10b shows dependence of the EL peak intensity vs. GaNP thickness. This is in agreement with the fact that the recombination rate in the active region is equal to the injection rate multiplied by the internal quantum efficiency of the diode:

$$n/\tau_r = (J/ed)\times\eta_{int} \quad (4.5),$$

where n is the carrier concentration, τ_r the recombination lifetime, J the current density, d the active layer thickness and η_{int} the internal quantum efficiency. Decreasing d leads to an increase of recombination rate (when keeping J the same), thus, an increase of the EL intensity.

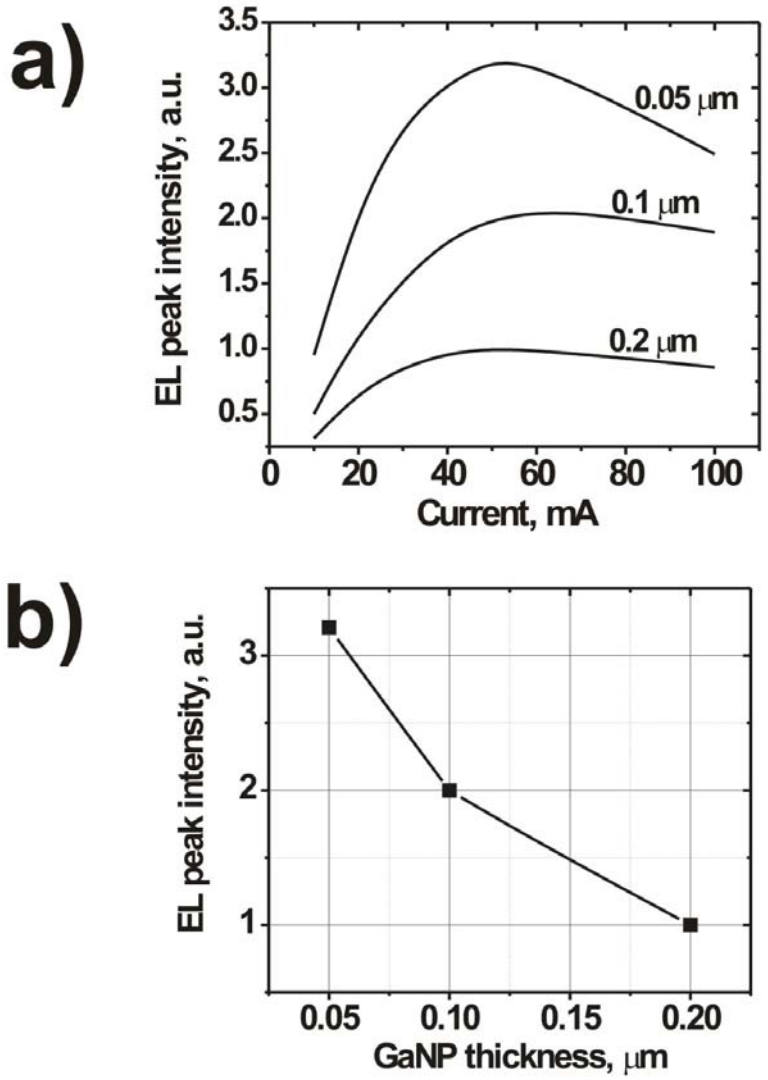

Figure 4.10. a) Normalized electroluminescence peak intensity of three LED chips with different thickness of GaNP active layer; b) normalized EL peak intensity vs. GaNP active layer thickness.

Figure 4.11 shows I-V curves of the three LED chips with different active layer thicknesses. The forward bias shows no significant difference, and the operating voltage at 20 mA is 2.5 V < V < 2.6 V, which is within the specification range of commercially available high-brightness AlInGaP-based LEDs. The offset voltage V_{off} ~ 2.2 V is close to the bandgap of the active region.

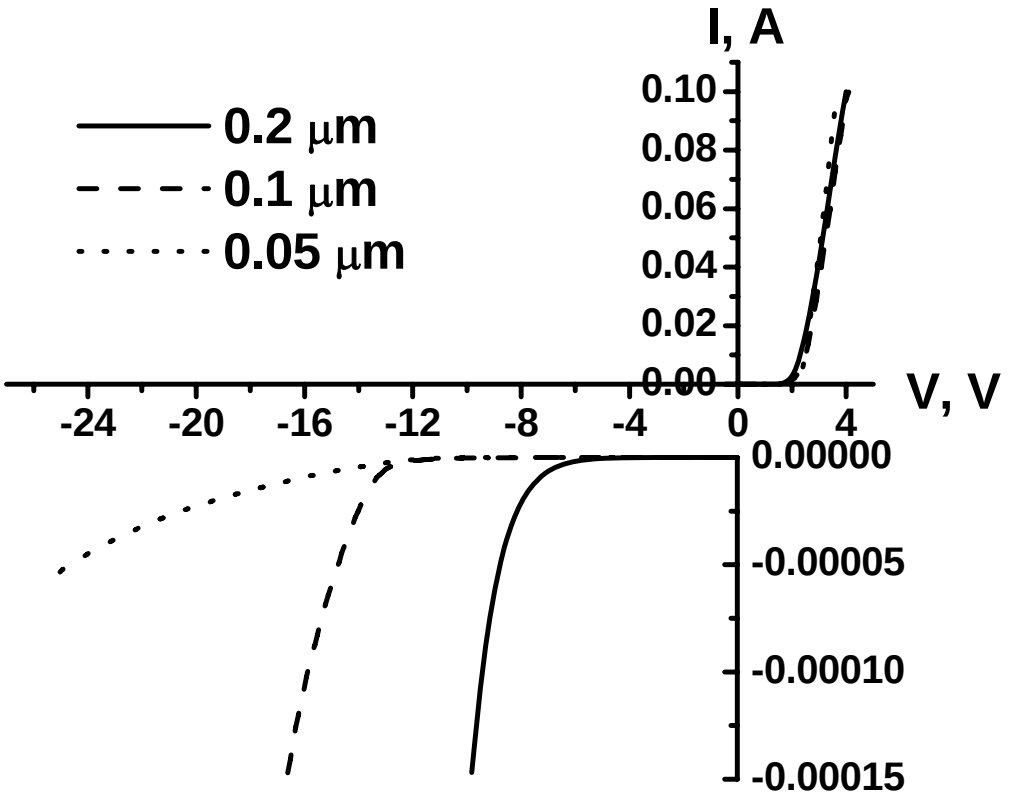

Figure 4.11. Current-voltage characteristics of three LED chips with different thickness of GaNP active layer.

However, the minimum breakdown voltage (V_{bd}) at -100 μA is different for LED chips tested. V_{bd} increases when the active layer thickness is decreased. We attribute this experimental fact to a decrease of the total number of defects in the active layer, when the

thickness of the active layer is decreased. Nitrogen incorporation from the plasma source into a growing film is accompanied by creation of point defects in the epilayer due to ion bombardient. Also, $GaN_{0.006}P_{0.994}$ grown on a GaP substrate (0.12% lattice mismatch) is strained, and some number of threading dislocations may appear, especially when the active layer thickness is close to the critical thickness (3000Å for $GaN_{0.006}P_{0.994}$, based on the Mathew and Blakeslee model[6]). Point defects and threading dislocations decrease the breakdown voltage of a diode, and a thicker active layer would have more defects. $|V_{bd}|$ decreases from 25 V for LED chips with a 0.05-μm-thick active region up more than 9.5 V for LED chips with a 0.2-μm-thick active region. Nevertheless, all $|V_{bd}|$ observed is much higher than that of AlInGaP-based LEDs (typical V_{bd} = - 6V). Higher $|V_{bd}|$ for GaNP-based LEDs may be a result of using a one-step epitaxy process. Conventional AlInGaP-based LEDs are bonded to a GaP substrate, which results in higher defect density in the substrate-LED interface and lower $|V_{bd}|$.

In order to measure the light intensity of the LED chips in an integrating sphere, chips are mounted on a TO can according to fabrication step 15 from the processing procedure, described in section 4.2.1. The light intensity of bare LED chips with a 0.05-μm-thick active region is measured to be 8-10 mcd under a drive current of 50 mA. This is for an LED structure containing no window layer, which can substantially improve light extraction from the LED chip and its external quantum efficiency[7]. The next step in studying (Al,In,Ga)NP-based LEDs is to deploy InGaNP quantum well structures as the active layers for an LED structures.

4.5.2. Color stability

It is important to note that very small red shift of 2 nm of the EL peak position is observed when the drive current is increased up to 60 mA (see Fig. 4.9). For comparison, we have measured the dependence of the EL peak position of commercial AlInGaP-based bare LED chips (Lumileds P3 Series TS). The EL peak wavelength shifts from 590 nm to 603 nm, when the drive current is increased from 10 mA to 60 mA in CW mode. The relative wavelength shifts vs. the drive current of GaNP-based LED bare chip and commercial AlInGaP-based bare LED chip are presented in the Fig. 4.12. The symbols

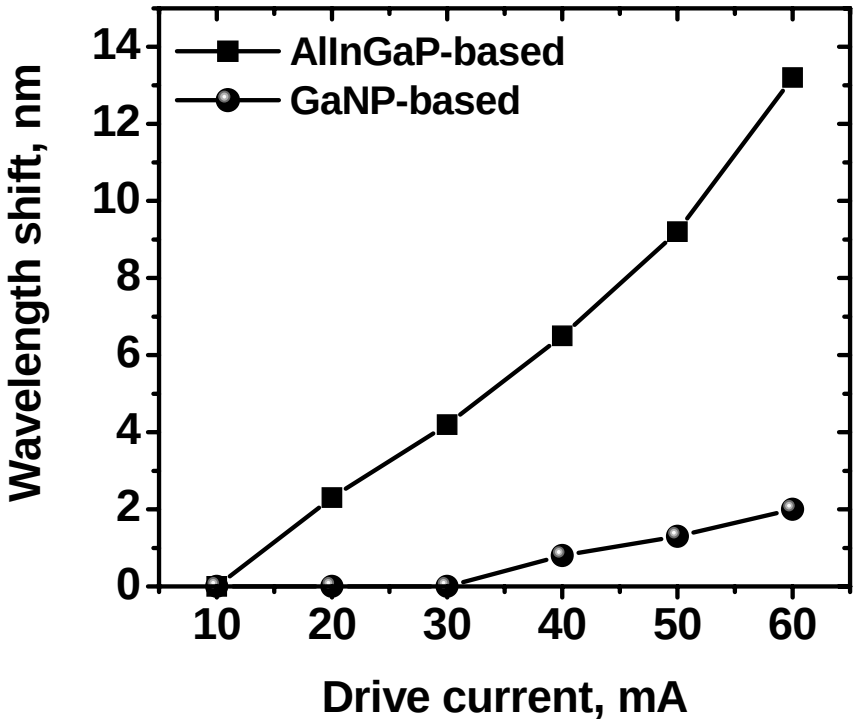

Figure 4.12. Wavelength shift vs. the drive current for bare GaNP-based LED chips and AlInGaP-based LED chips.

are experimental data. One of the factors that result in the smaller wavelength shift is the weaker temperature dependence of the GaNP bandgap as compared to that of the AlInGaP bandgap. The Varshni equation[8] is used to describe the temperature dependence of the bandgap of a semiconductor:

$$E_g(T) = E_g(0) - \frac{\gamma T^2}{T+\beta} \quad (eV) \qquad (4.6),$$

where γ and β are fitting parameters. For AlInGaP[9] $\gamma_{AlInGaP} = 4.1\times10^{-4}$ eV/K and $\beta_{AlInGaP}$ = 136 K. We have measured the temperature dependence of the photoluminescence peak position of a 0.05-μm-thick $GaN_{0.006}P_{0.994}$ layer. The best Varshni fit yields $\gamma_{GaNP}=2.7\times10^{-4}$ eV/K and β_{GaNP} =140 K. While the β parameter is almost the same for both materials, the difference in the γ parameter for AlInGaP and GaNP layers is a factor of 1.5. This means that the bandgap of AlInGaP changes more than that of GaNP in the same temperature range.

Another factor that influences on the LED chip temperature is thermal resistivity of the alloys used in LED structures. The thermal resistivity increases in ternary and quarternary alloys due to increased phonon scattering[10]. In GaNP-based LEDs only the active region is a ternary alloy and the rest of the structure is binary GaP. In AlInGaP-based LEDs lattice-matched to GaAs, the alloy is the most random as the In composition is 50%. For example, the thermal resistivity of $In_{0.5}Ga_{0.5}P$ is around 8 times higher (see Fig. 4.13) than that of GaP[10], and it is even higher if Al is introduced into the alloy, which increases disorder. We conclude that the thermal resistivity of GaNP-based LEDs is lower than that of AlInGaP-based LEDs. This would lead to a higher temperature rise of

an AlInGaP-based LED die as compared to a GaNP-based LED die at the same drive current.

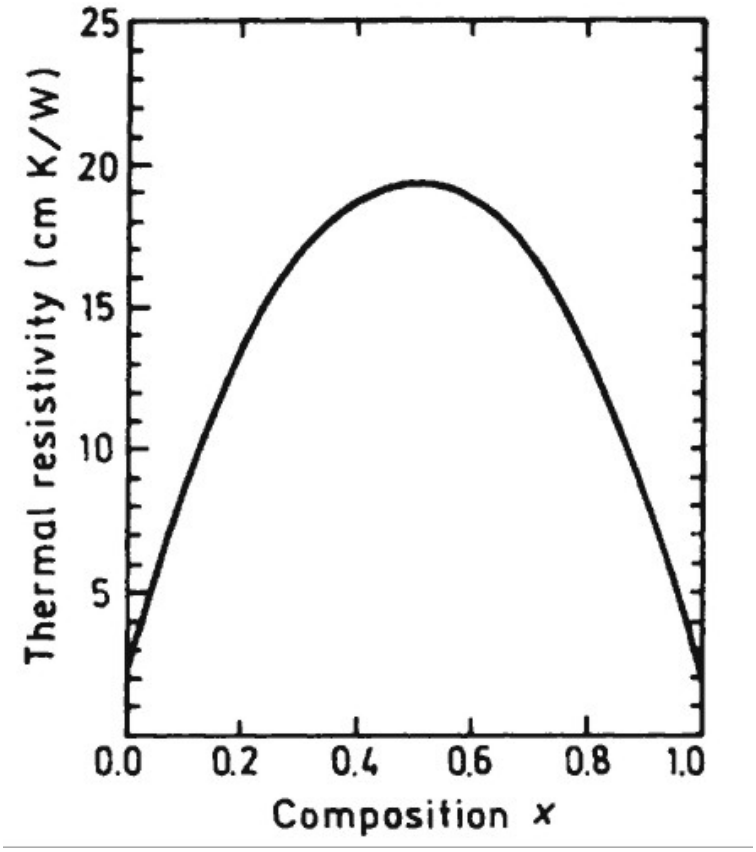

Figure 4.13. Thermal resistivity of InGaP vs. In concentration in the alloy.

4.6. InGaNP QW-based LEDs

In this section we study electroluminescence and I-V characteristics of InGaNP single and multiple QW-based LEDs, and compare the current overflow in InGaNP QW-based LEDs with AlInGaP QW-based LEDs.

4.6.1. Single and multiple quantum well LEDs

The series of three $In_yGa_{1-y}N_{0.005}P_{0.995}$ single QW-based LED structures, shown in Fig. 4.7b, with different In concentration (0%, 13% and 17%) is grown for a study. LED chips are fabricated according to steps 1-14 in section 4.2.1. Figure 4.14 shows EL spectra of the fabricated LED chips at a current of 20 mA. An increase of the indium concentration in the quantum well results in a red shift of the EL peak position and an

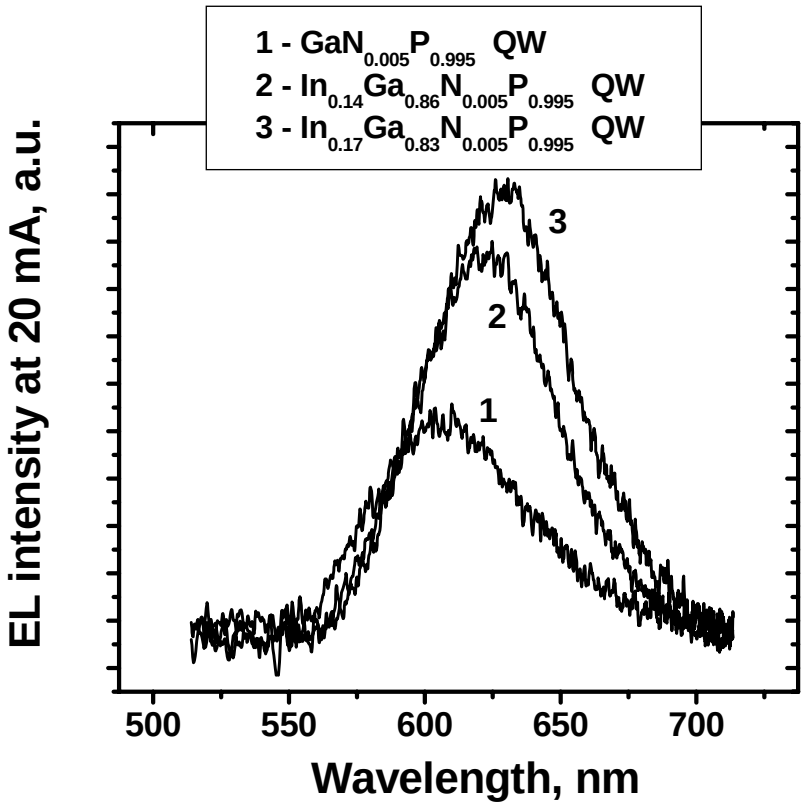

Figure 4.14. EL spectra, taken at 20 mA drive current, for $In_yGa_{1-y}N_{0.005}P_{0.995}$ QW – based LEDs with y = 0, 0.14, and 0.17.

intensity. This result is expected since similar behavior has been observed in the dependence of PL intensity vs. In concentration in $In_yGa_{1-y}N_{0.008}P_{0.992}$, studied in section 3.4.2 (Fig. 3.15), although the increase of the PL intensity is much higher (12 times, for 0<[In]<0.2), than increase of the EL intensity (2 times, for 0<[In]<0.17).

Another series of three $In_{0.1}Ga_{0.9}N_{0.005}P_{0.995}$ multiple QW-based LED structures, shown in Fig. 4.7b, with different number of quantum wells (1, 3 and 6 QWs) is grown in order to study the effect of multiple QWs on EL intensity. The active region consists of multiple $In_{0.1}Ga_{0.9}N_{0.005}P_{0.995}$ QWs (1 to 6 QWs), separated by a 30-nm-thick GaP spacers. The total active region thickness is kept the same for all the LED structures grown. LED chips are fabricated from LED structures with different number of QWs. The peak emission wavelength of all LED chips measured is 620 nm. Figure 4.15 shows the dependence of EL intensity vs. drive current for LED chips with 1, 3 and 6 QWs. The EL intensity increases with the number of QWs. The peak EL intensity of the 6-QW LED structure is higher than that of the 1-QW LED structure by a factor of two. The saturation current increases with the number of QWs, as expected (inset in Fig. 4.15). This is due to decreased current overflow from the active region with more QWs (see next section).

Finally, $In_{0.1}Ga_{0.9}N_{0.005}P_{0.995}$ single QW-based LED chips are packaged, according to optional fabrication steps 15-16 from section 4.2.1. Chips are mounted on TO cans and dipped into epoxy. Figure 4.16 shows the dependence of EL intensity vs. drive current for a bare LED chip and a packaged LED chip. The EL intensity at 50 mA for the packaged chip is 3 times higher than that of bare LED chip. This is because light extraction from the packaged chip is better, when an epoxy dome is used. Using epoxy decreases the

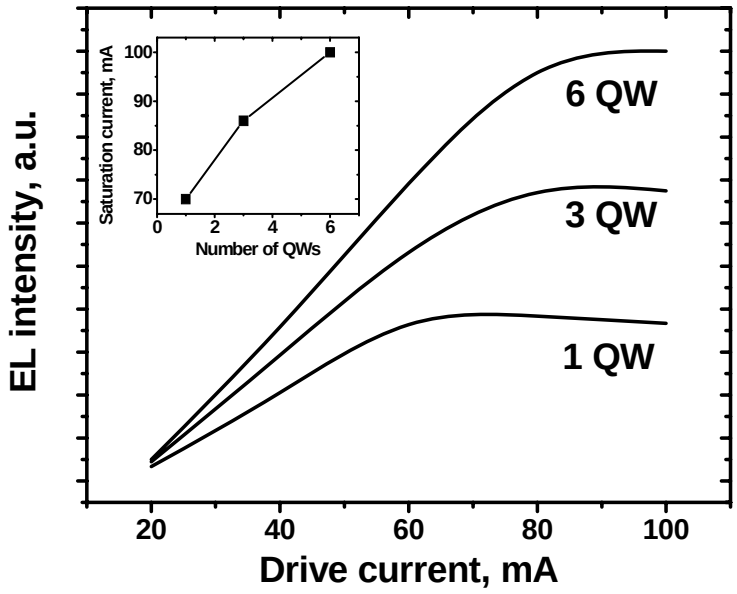

Figure 4.15. EL intensity vs. the drive current for LED chips with different number of QWs. Inset shows saturation current as a function of the number of QWs in the LED structure.

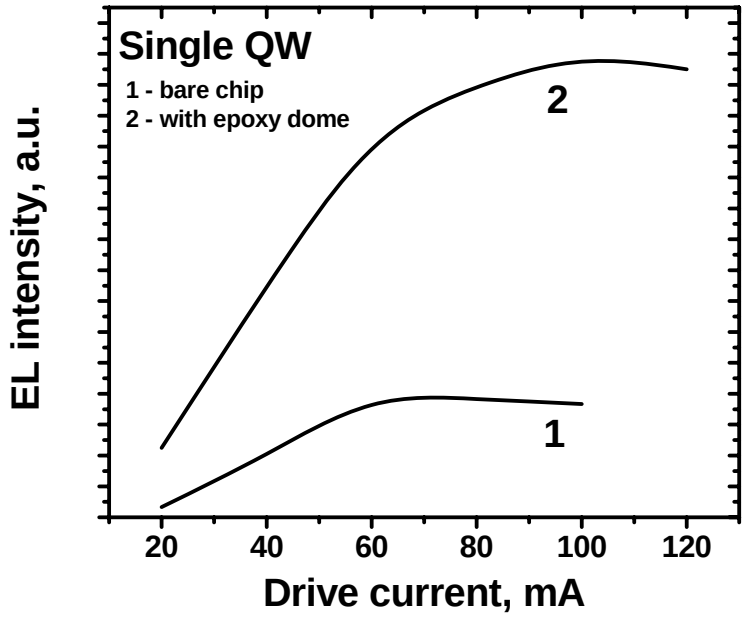

Figure 4.16. EL intensity vs. the drive current for bare InGaNP single QW – based LED chip (curve 1), and for LED chip in epoxy dome (curve 2).

difference in the refractive index between the semiconductor (GaP) and the environment, thus reducing total internal reflection. Therefore, a larger angle is allowed for light to escape from the chip.

4.6.2. Current overflow in the quantum well

In the previous section we discussed an increase of the saturation current of the LED chip, when a larger number of QWs is used in the active region of an LED structure. In this section we compare current overflow in InGaNP QW-based LED structures and AlInGaP QW-based LED structures.

The current overflow in a QW occurs when the Fermi level reaches the top of the barrier. The current density, $J_{overflow}$, when overflow occurs in the QW over the conduction band barrier, can be expressed as follows[11]:

$$J_{overflow} = \left[\frac{m^*}{\pi (h/2\pi)^2} \left(\Delta E_c - E_0 \right) \right]^2 \frac{eB}{W_{QW}} \qquad (4.7),$$

where m^* is the electron effective mass in the QW, ΔE_c is the conduction band offset, E_0 is the ground-state energy of the QW, B is the bimolecular recombination coefficient, and W_{QW} is the QW width. In our case, by ΔE_c we mean the energy separation between the X-valley in the barrier and the Γ-valley in the QW. The bimolecular recombination rate, B, can be simply estimated for a direct bandgap semiconductor, following Garbusov's equation[12]:

$$B = 3\times10^{-10}\,\frac{cm^3}{s}\left(\frac{300K}{T}\right)^{3/2}\left(\frac{E_g}{1.5eV}\right)^2 \qquad (4.8),$$

where E_g is the semiconductor bandgap.

Using (4.7) and (4.8) we can estimate the difference between $J_{overflow}$ in InGaNP-based LEDs and conventional AlInGaP-based LEDs. $In_{0.1}Ga_{0.9}N_{0.005}P_{0.995}$ and $Al_{0.08}In_{0.5}Ga_{0.42}P$[13] have the same bandgap of 2 eV, so B will be the same for both materials, based on equation (4.8). Then, the difference in $J_{overflow}$ between $In_{0.1}Ga_{0.9}N_{0.005}P_{0.995}$/GaP QW and $Al_{0.08}In_{0.5}Ga_{0.42}P/Al_{0.5}In_{0.5}P$ QW will be determined by the electron effective mass, m^*, and (ΔE_c-E_0), if W_{QW} is the same. We have determined the electron effective mass of $In_{0.1}Ga_{0.9}N_{0.005}P_{0.995}$ to be $0.63m_e$[14], whereas the electron effective mass of $Al_{0.08}In_{0.5}Ga_{0.42}P$ equals to $0.115m_e$, according to Ref. [13]. The conduction band offset of $In_{0.1}Ga_{0.9}N_{0.005}P_{0.995}$/GaP QW is 245 meV (see Fig. 3.21 in section 3.4.4), and that of $Al_{0.08}In_{0.5}Ga_{0.42}P/Al_{0.5}In_{0.5}P$ QW is 125 meV (see Ref. [2]). Because of the large electron effective mass in $In_{0.1}Ga_{0.9}N_{0.005}P_{0.995}$ (m^*=$0.63m_e$), we can neglect E_0 in the (ΔE_c-E_0) term, since the quantum level will be very close to the bottom of the conduction band. We will also neglect E_0 in (ΔE_c-E_0) for $Al_{0.08}In_{0.5}Ga_{0.42}P/Al_{0.5}In_{0.5}P$, because this is the worst case scenario for comparing $J_{overflow}$ of the two material systems, as (ΔE_c-E_0) for $Al_{0.08}In_{0.5}Ga_{0.42}P/Al_{0.5}In_{0.5}P$ QW will be the largest. Finally, the difference between $J_{overflow}$ of the two quantum wells considered can be expressed as follows:

$$\frac{J_{overflow,In_{0.1}Ga_{0.9}N_{0.005}P_{0.995}}}{J_{overflow,Al_{0.08}In_{0.5}Ga_{0.42}P}} = \left(\frac{m^*_{In_{0.1}Ga_{0.9}N_{0.005}P_{0.995}}}{m^*_{Al_{0.08}In_{0.5}Ga_{0.42}P}}\frac{\Delta E_{c,In_{0.1}Ga_{0.9}N_{0.005}P_{0.995}}}{\Delta E_{c,Al_{0.08}In_{0.5}Ga_{0.42}P}}\right)^2 \geq 100 \qquad (4.9).$$

Thus, because of the higher electron effective mass and larger conduction band offsets of $In_{0.1}Ga_{0.9}N_{0.005}P_{0.995}$/GaP QW vs. $Al_{0.08}In_{0.5}Ga_{0.42}P/Al_{0.5}In_{0.5}P$ QW a higher light output at high drive currents of InGaNP-based LEDs over conventional AlInGaP-based LEDs can be expected.

4.7. Effect of AlGaP claddings

This section describes the effect of AlGaP cladding layers on $In_{0.1}Ga_{0.9}N_{0.005}P_{0.995}$ single QW-based LED performance (I-V and EL intensity). We study the influence of AlGaP cladding thickness and AlGaP/GaP interface δ-doping on the I-V characteristics, and the influence of the Al concentration in the cladding layers on the I-V characteristics and EL intensity of the LED chips.

First, we consider the influence of AlGaP cladding thickness and AlGaP/GaP interface δ-doping on the I-V characteristics. Two LED structures (A and B), shown in Fig. 4.7c, are grown with $Al_{0.3}Ga_{0.7}P$ cladding layers. The LED structure A has 0.75-μm-thick $Al_{0.3}Ga_{0.7}P$ cladding layers but has no AlGaP/GaP interface δ-doping. The LED structure B has 0.5-μm-thick $Al_{0.3}Ga_{0.7}P$ cladding layers and has an AlGaP/GaP interface δ-doping, described in section 4.4. The SEM image of the LED structure A is shown in Fig. 4.17. The interfaces are abrupt and all the layers (claddings, active region, contact layer), except the quantum well, can be clearly seen in the micrograph. We compare the I-V characteristics (Fig. 4.18) of LED chips, fabricated according to steps 1-14 (section

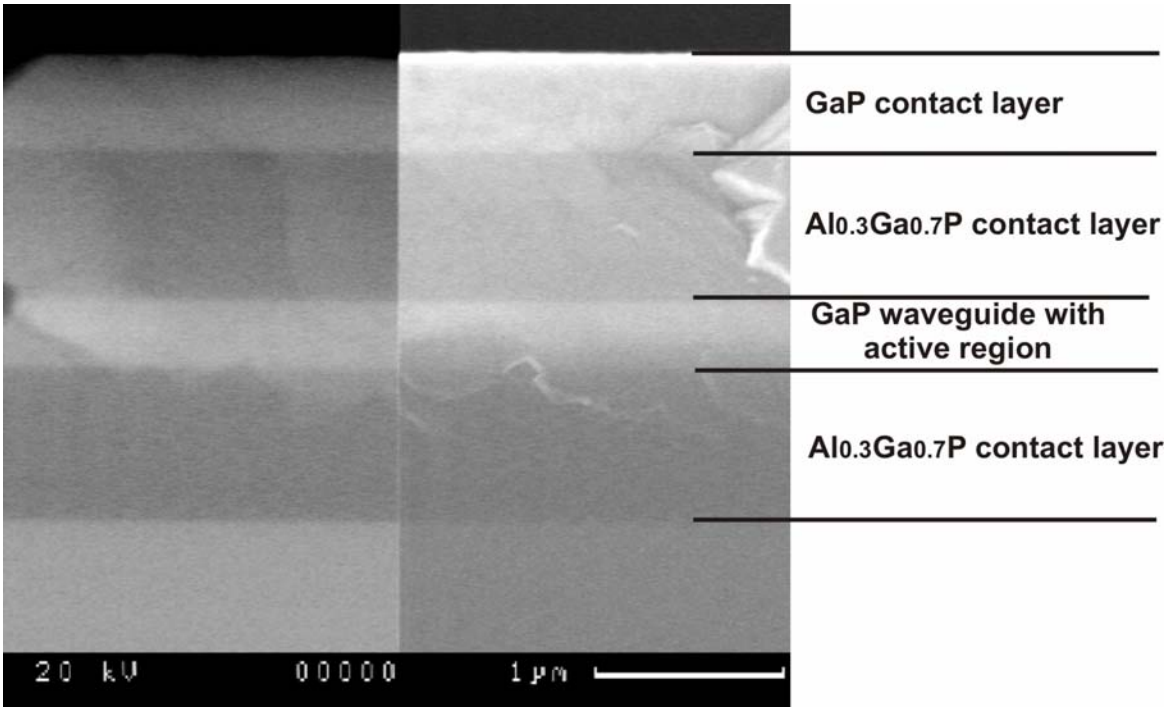

Figure 4.17. Cross section SEM image of InGaNP single QW – based LED with AlGaP cladding layers.

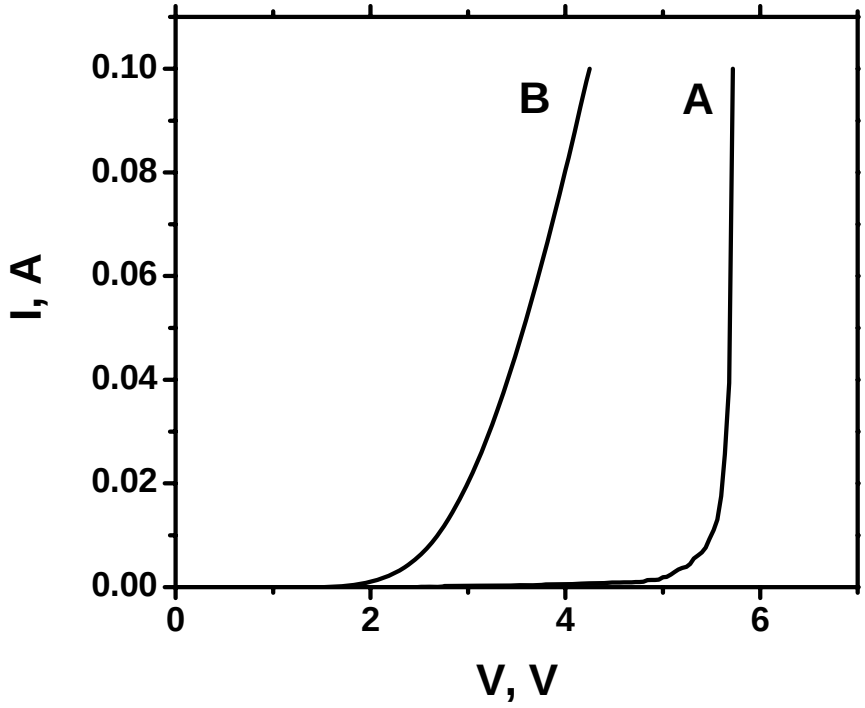

Figure 4.18. I-V characteristics of LED structure A and LED structure B.

4.2.1) from LED structures A and B. The I-V characteristics of LED structure A has an offset voltage V_{off} ~ 5.5 V, which is much higher than the GaP band gap (2.26 V). This large voltage drop may occur on the AlGaP/GaP interfaces, due to the large AlGaP/GaP band offsets. Once the applied forward voltage to LED structure A is sufficient (> 5 V) for the carriers to overcome the potential barriers on the AlGaP/GaP interfaces, the current increases rapidly. For comparison, LED structure B (with δ-doping) has a much lower offset voltage V_{off} ~ 2.7 V, which is closer to the GaP band gap (2.26 eV). This may be caused by lowering the potential barriers for the carriers on the interface, when δ-doping is used.

It is important to mention that both LED structures (A and B) are processed at the same time to assure no processing mistakes, which may influence on the I-V characteristics. LED structure A is processed two times to assure good contact quality. The same I-V result is observed for the LED chips from the second processing of LED structure A. Thus, we have made sure that the large offset voltage V_{off} ~ 5.5 V is due to internal properties of the LED structure, not contact performance. Since decreasing the thickness of AlGaP cladding layers from 0.75 μm to 0.5 μm and introducing δ-doping at the AlGaP/GaP interfaces reduce the offset voltage V_{off} from 5.5 V to 2.7 V, we use 0.5-μm-thick AlGaP claddings with δ-doping for the study of the AlGaP claddings with different Al concentration.

We use AlGaP cladding layers in the LED structures, but AlGaP/GaP is a type II heterojunction. This will influence on the electrical and optical properties of the LED structure in ways different from conventional type I heterostructures. We have calculated,

Fig. 4.19, the band offsets between $Al_xGa_{1-x}P$ and GaP (ΔE_c and ΔE_v) based on Ref. [4]. The AlGaP cladding layers provide optical and electrical confinement for holes in the active region. Optimization of the Al concentration in the $Al_xGa_{1-x}P$ cladding layers is required, since there is no additional confinement for electrons. The beneficial effect of the $Al_xGa_{1-x}P$ cladding layers on the light output can be achieved within a certain Al concentration range. A series of four single $In_{0.1}Ga_{0.9}N_{0.005}P_{0.995}$ QW LED structures is grown with different Al concentrations in the cladding layers: 0, 0.14, 0.3 and 0.77. The symbols in Fig. 4.19 correspond to the samples grown.

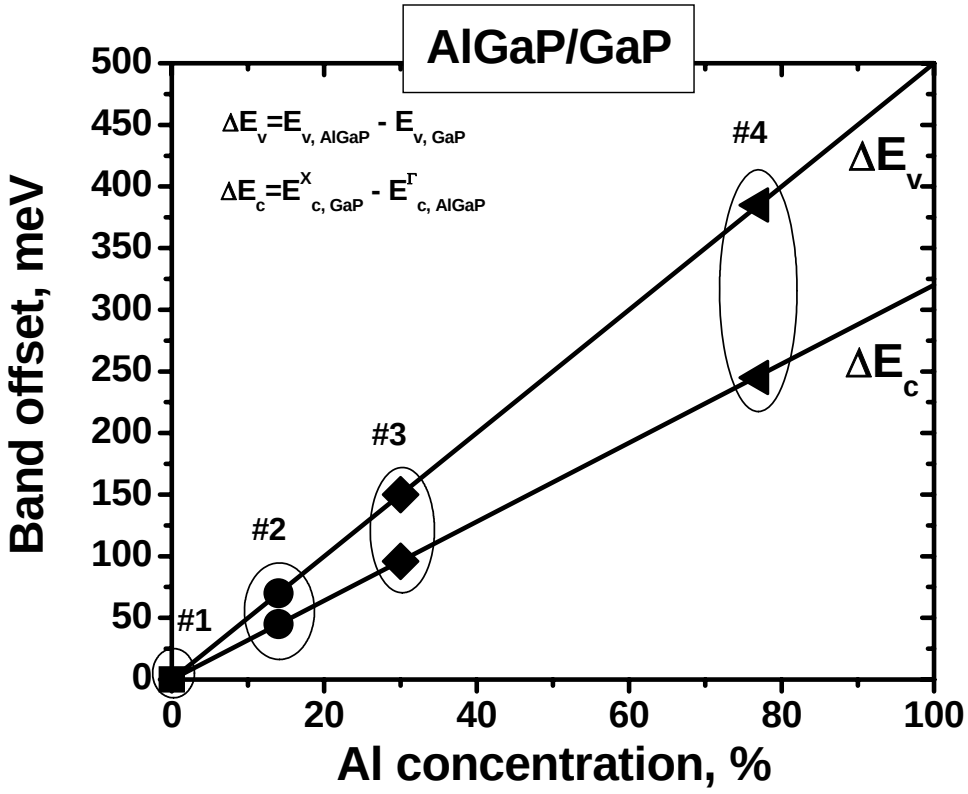

Figure 4.19. Conduction and valence band offsets of $Al_xGa_{1-x}P$/GaP as a function of x.

The advantages of introducing the AlGaP cladding layers include optical and electrical confinement for holes in the active region. Figure 4.20 shows current voltage characteristics for LED chips fabricated from structures with different Al concentrations. The series resistance changes from 13.8 Ω to 15.4 Ω, when the Al concentration in the cladding layers is increased from 0 to 0.3. When $Al_{0.77}Ga_{0.23}P$ cladding layers are used, the I-V characteristic can be divided into two regions with different series resistance: 280 Ω and 13.5 Ω. This high initial series resistance is most likely due to the large potential barrier for holes (385 meV). Using δ-doping does not improve I-V characteristic much, when such a high Al concentration is used.

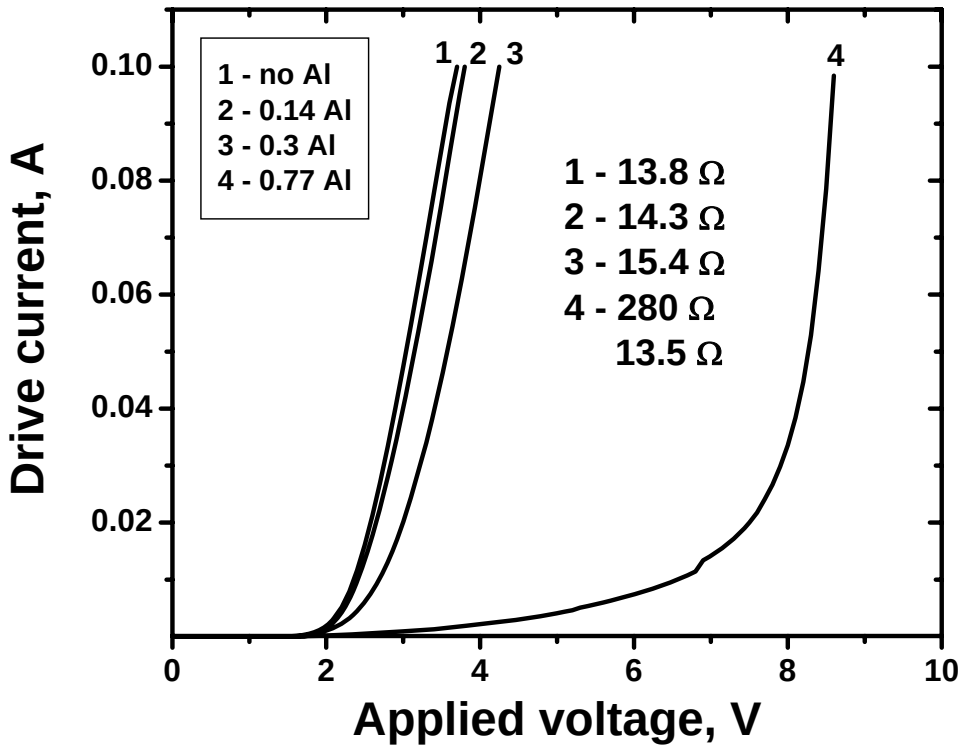

Figure 4.20. Current-voltage characteristics for LED structures with different Al concentration in the cladding layer ($0 \leq x \leq 0.77$).

To find the optimal Al concentration in the cladding layer, EL measurements are performed. Figure 4.21 shows the dependence of the EL peak intensity at 50 mA drive current vs. Al concentration in the cladding layers. One can see that the optimal Al concentration is 0.14 as this provides an overall light output improvement of 15%. When the Al concentration increases from 0.14 to 0.3 the series resistance increases by 8% (Fig. 4.20), and light output experiences a 64% drop (Fig. 4.21). The reasons for an increase in the series resistance are an increase of ΔE_{c1} from 43 meV (< 2kT) to 93 meV (~ 4kT), and an increase of ΔE_{v1} from 70 meV (< 3kT) to 150 meV (~ 6kT) in this range of Al concentrations (0.14<x<0.3).

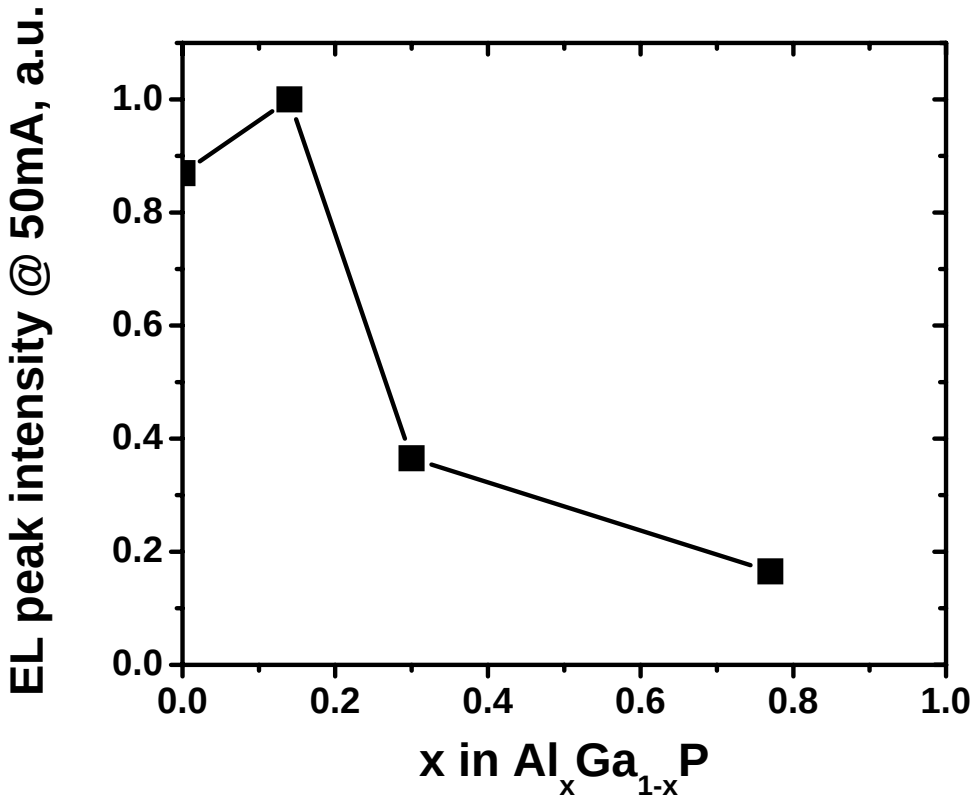

Figure 4.21. Current-voltage characteristics of three LED chips with different thickness of GaNP active layer.

4.8. Conclusions

In this chapter we have studied growth, processing and characterization of (In,Al,Ga)NP-based LEDs grown directly on GaP (100) substrates by plasma-assisted GSMBE.

In particular, we have developed a processing procedure for (In,Ga,Al)NP-based LEDs grown on GaP (100) substrates, and performed contact optimization on a specially grown *p*-*i*-*n* diode structure, to ensure that *n*- and *p*-type contacts are ohmic.

Band offsets of (In,Al,Ga)NP-based LEDs are calculated to be about 3 times higher compared to those for AlInGaP-based LEDs. This should provide higher internal quantum efficiency at higher current densities and/or at higher temperatures.

Amber GaNP-based LEDs, directly grown on a transparent GaP substrate, have been realized. The red shift of the EL peak position for GaNP-based LEDs (2 nm) is much smaller than that of AlInGaP-based LEDs (13 nm), when the drive current is increased from 10 to 60 mA. This is because of the weaker temperature dependence of the GaNP bandgap as compared to that of the AlInGaP bandgap and higher thermal resistance of the AlInGaP alloy. The EL intensity increases, when the GaNP active layer thickness is decreased, which is in agreement with the equation for injection-recombination rate. A decrease of the active layer thickness of GaNP-based LEDs results in an increase of the breakdown voltage, since fewer defects are introduced into the structure. Currently achieved light intensity (8-10 mcd) satisfies requirements for

indicator lamp application, but the LED structure can be optimized further to increase the light intensity for high-brightness applications.

A series of InGaNP QW-based LEDs has been grown on a transparent GaP (100) substrates. An increase of the In concentration in the QW from 0% to 17% results in an increase of EL intensity by a factor of two. An increase of the number of QWs in the LED structure from 1 to 6 results in an increase of EL intensity by a factor of two as well. An increase of the saturation current with an increase of the number of QWs in the active region has been also observed. Packaging of bare LED chip (using epoxy dome) increases EL intensity by a factor of three. For the same bandgap and well width, the current overflow density, $J_{overflow}$, is estimated to be 100 times higher for InGaNP QW-based LEDs as compared to conventional AlInGaP QW-based LEDs.

Finally, the effect of AlGaP cladding layers on I-V characteristics and EL intensity of InGaNP single QW-based LED is studied. δ-doping of AlGaP/GaP interfaces substantially reduces the offset voltage, V_{off}. The optimal Al concentration in the AlGaP cladding layers is found to be 0.14. It provides an EL intensity increase of 15%.

In conclusion, the best LED structure design would be InGaNP MQW–based LEDs with $Al_{0.15}Ga_{0.85}P$ claddings, since both approaches – QW active layer and cladding layers, when optimized, exhibited increased light output from LED chips.

Materials in this Chapter were accepted for publication in Applied Physics Letters and in Journal of Vacuum Science and Technology B.

References:

[1] H. P. Xin, R. J. Welty, and C. W. Tu, Appl. Phys. Lett., **77**, 1946 (2000).

[2] D. Patel, J. M. Pikal, C. S. Menoni, K. J. Thomas, F. A. Kish, M. R. Hueschen, Appl. Phys. Lett., **75**, 3201 (1999).

[3] W. Shan, W. Walukiewicz, J. W. Ager III, E.E. Haller, J. F. Geisz, D. J. Friedman, J. M. Olson, and S. R. Kurtz, Phys. Rev. Lett. **82**, 1221 (1999).

[4] S. Tiwari and D. J. Frank, Appl. Phys. Lett. **60**, 630 (1992).

[5] V. A. Odnoblyudov, C. W. Tu, J. Vac. Sci. Tech. B **23**, 1317 (2005).

[6] J. W. Mathews and A. E. Blakeslee, J. Cryst. Growth **27**, 118 (1974).

[7] E. Fred Schubert, *Light-emitting diodes*, Cambridge, 126 (2003).

[8] Y. P. Varshni, Physica **34**, 149 (1967).

[9] M.-F. Huang, P.-H. Liu, J. S. Liu, Y.-K. Kuo, Y.-L. Huang, Y. Chang, H.-C. Huang, K.-K. Horng, J.-Y. Chang, SPIE Proc **4078**, 595 (2000).

[10] S. Adachi, J. Appl. Phys. **54,** 1844 (1983).

[11] E. Fred Schubert, *Light-Emitting Diodes*, Cambridge, 75 (2003).

[12] E. Fred Schubert, *Light-Emitting Diodes*, Cambridge, 52 (2003).

[13] P. Raisch, R. Winterhoff, W. Wagner, M. Kessler, H. Schweizer, T. Riedl, R. Wirth, A. Hangleiter, and F. Scholz, Appl. Phys. Lett. **74**, 2158 (1999).

[14] V. A. Odnoblyudov, C. W. Tu, Appl. Phys. Lett., to be published.

Chapter 5. Summary and suggestions for future work.

5.1. Summary

Nitrogen incorporation into GaP (100) changes the band structure of GaP, and converts this material from indirect band gap into direct band gap material. The phenomenon of giant band gap 'bowing' observed in GaNP (similar to GaNAs) is promising to increase the flexibility in the choice of semiconductor band gaps available for specified lattice constants. In particular, InGaNP material, directly grown on GaP (100) substrates, is a perfect candidate for making yellow-amber-red LEDs. The main driving force for this dissertation is to investigate some optical and structural properties of (Al,In,Ga)NP, grown on GaP (100) substrates, demonstrate feasibility of this novel material system for LED applications, and develop and optimize LEDs, based on this material system.

There are two major chapters in the dissertation: Chapter 3 and Chapter 4. In Chapter 3 we described the growth and characterization of the (Al,In,Ga)NP material system. In particular, increasing the nitrogen composition in the GaNP bulk layers from 0.6 to 1.7% leads to light emission color from yellow-amber to red. An optimal growth temperature window of 500-520^{0}C for GaNP bulk layers was determined from an analysis of their structural and optical properties. Temperature dependence of the PL peak position for 7-nm-thick $GaN_{0.005}P_{0.995}$ QWs agrees well with the Varshni equation.

Then, single-crystalline AlGaNP layers with 0%<[Al]<100% were grown on GaP (100) substrates using a RF nitrogen plasma source and thermally cracked phosphine. The difference in nitrogen incorporation into GaP and AlP has been determined (factor of 3.4). An equilibrium thermodynamic model, applied to the growth of AlGaNP, has qualitatively explained this difference. The Gibbs free energy released during the formation of AlN is larger than that of GaN. The best crystal quality (as determined from x-ray diffraction) of AlGaNP layers is achieved for an aluminum compositions of 80%<[Al]<100%, and the worst crystal quality is observed for [Al]=50%, as expected.

Finally, the optical properties of InGaNP quantum wells in GaP barriers were studied. Post-growth annealing of InGaNP QWs leads to higher PL intensity by a factor of 5 and a blue shift of the PL peak position by 2 nm. Emission color from yellow–amber to red can be realized using 7-nm-thick $In_yGa_{1-y}N_xP_{1-x}$ QWs, while lattice-matching condition of $In_yGa_{1-y}N_xP_{1-x}$ to GaP can be satisfied. Temperature dependence of the PL peak position of the 7-nm-thick $In_{0.1}Ga_{0.9}N_{0.005}P_{0.995}$ QW deviates from the Varshni equation in temperature range of 125 K to 290 K, most likely as a result of the clustering effect. The electron effective mass of the $In_yGa_{1-y}N_{0.005}P_{0.995}$ alloy decreases from 0.77 m_e to 0.4 m_e, when the indium concentration is increased from 5% to 20%. The conduction and valence band offsets of $In_yGa_{1-y}N_{0.005}P_{0.995}$/GaP heterojunction were calculated for $0 \leq y \leq 0.2$, using Van de Walle's model-solid theory.

The results of Chapter 3, given above, allowed the use of the (Al,In,Ga)NP material system to develop new technology for yellow-amber-red LEDs. Chapter 4 describes growth, optimization and processing of (Al,In,Ga)NP-based LEDs.

In particular, we have developed a processing procedure for (Al,In,Ga)NP-based LEDs grown on GaP (100) substrates, and performed contacts optimization on a specially grown *p*-*i*-*n* diode structure, to ensure that *n*- and *p*-type contacts were ohmic.

The band offsets of (Al,In,Ga)NP-based LEDs were calculated to be about 3 times than those of AlInGaP-based LEDs. This should result on higher internal quantum efficiency at higher current densities and/or at higher temperatures.

Amber GaNP-based LEDs, directly grown on a transparent GaP substrate, have been realized. The red shift of the EL peak position for GaNP-based LEDs (2nm) is much smaller than that of AlInGaP-based LEDs (13nm), when the drive current is increased from 10 to 60 mA. This is because of the weaker temperature dependence of GaNP bandgap as compared to that of AlInGaP bandgap and higher thermal resistance of the AlInGaP alloy. The EL intensity increases when the GaNP active layer thickness is decreased, which is in agreement with the equation for injection-recombination rate. A decrease of the active layer thickness of GaNP-based LEDs results in an increase of the breakdown voltage, since fewer defects are introduced into the structure. Currently achieved light intensity (8-10 mcd) satisfies requirements for indicator lamp application, but the LED structure can be optimized further to increase the light intensity for high-brightness applications.

A series of InGaNP QW-based LEDs have been grown on a transparent GaP (100) substrates. An increase of the In concentration in the QW from 0% to 17% results in an increase of EL intensity by a factor of two. An increase of the number of QWs in the LED structure from 1 to 6 results in an increase of the EL intensity by a factor of two

as well. An increase of the saturation current with an increase of the number of QWs in the active region has also been observed. Packaging of bare LED chip (using epoxy dome) increases EL intensity by a factor of three. For the same bandgap and well width, the current overflow density, $J_{overflow}$, is estimated to be 100 times higher for InGaNP QW-based LEDs as compared to conventional AlInGaP QW-based LEDs.

Finally, the effect of AlGaP cladding layers on I-V characteristics and EL intensity of InGaNP single QW-based LEDs was studied. δ-doping of AlGaP/GaP interfaces substantially reduces the offset voltage, V_{off}. The optimal Al concentration in the AlGaP cladding layers was found to be 0.14. It increased the EL intensity by 15%.

In conclusion, the best LED structure design would be InGaNP MQW–based LEDs with $Al_{0.15}Ga_{0.85}P$ claddings, since both approaches – QW active region and cladding layers, when optimized, exhibited increased light output from LED chips.

5.2. Accomplished tasks

This work was planned to accomplish certain tasks, described in Chapter 1, Section 1.3. The following is a summary of the accomplished tasks.

1. The growth conditions of the GaNP/GaP material system were optimized.
2. High structural quality AlGaNP/GaP materials were synthesized using plasma-assisted GSMBE, and their structural properties were studied.

3. InGaNP/GaP quantum wells were successfully grown, sand some of the optical properties were studied.
4. The InGaNP material system was used as the active region of LEDs, emitting in the yellow-red spectral range.
5. Fabrication process for (Al,In,Ga)NP–based LEDs was successfully developed.
6. Optimization of the LED structure and its growth conditions were performed.

Thus, all the tasks, planned to be accomplished in this dissertation, were successfully accomplished.

The next section describes suggestions for future work.

5.3. Suggestions for future work

There are a number of areas not within the scope of this dissertation, but they require further research and optimization in order to bring (Al,In,Ga)NP-based LEDs to the level of commercially available yellow-amber-red AlInGaP-based LEDs.

First is optimization of the growth conditions of InGaNP/GaP quantum wells. The growth temperature can be varied and the PL intensity of the samples can be studied in order to determine the optimal growth temperature. The PH_3 flux can also be varied as it may impact the PL intensity as well.

Second is further LED structure/design optimization. This may include optimization of the InGaNP quantum well placement in the waveguide region (barrier thickness); optimization of the doping profile; optimization of the contact/window layer.

The doping profile, combined with QW placement, is a very important LED optimization parameter. Improper (too high or to low) doping concentrations of the *n*-type and *p*-type diode areas may lead to a *p*-*n* junction displacement away from the active region, which may result in a significant drop in the LED light output[1]. Doping profile has to be carefully chosen in order to keep the center of the *p*-*n* junction in the active region of the LED structure. The best way is to calculate the minority carrier distribution in the *p*-*n* junction, depending on the doping concentration.

The contact/window layer of the LED structure also has to be optimized. Increasing the thickness of the window layer leads to a better light extraction from the LED chip and to better current spreading. The contact/window layer alone may increase the external quantum efficiency of the device by a factor of eight[2].

Third, further study of the AlGaNP material for green LED application. Al increases the band gap of GaP, and nitrogen converts material from indirect band gap into a direct band gap. This is the basis for moving the emission wavelength into the green spectral region.

In this dissertation, only structural properties of the AlGaNP material system were studied. No PL signal was detected from the AlGaNP bulk layers. One of the reasons for no PL signal is type-II heterojunction, formed by GaP/AlGaNP. No confinement for holes exists, thus, holes may diffuse into GaP and do not participate in the recombination

process. The special LED structure design may be applied in order to create a type-I heterojunction between the active AlGaNP layer and barrier layers. This may be achieved by using a higher Al concentration (x>y) in the $Al_xGa_{1-x}P$ barrier (cladding) layers than in the $Al_yGa_{1-y}NP$ active layer. Figure 5.1 shows an example of such an LED structure.

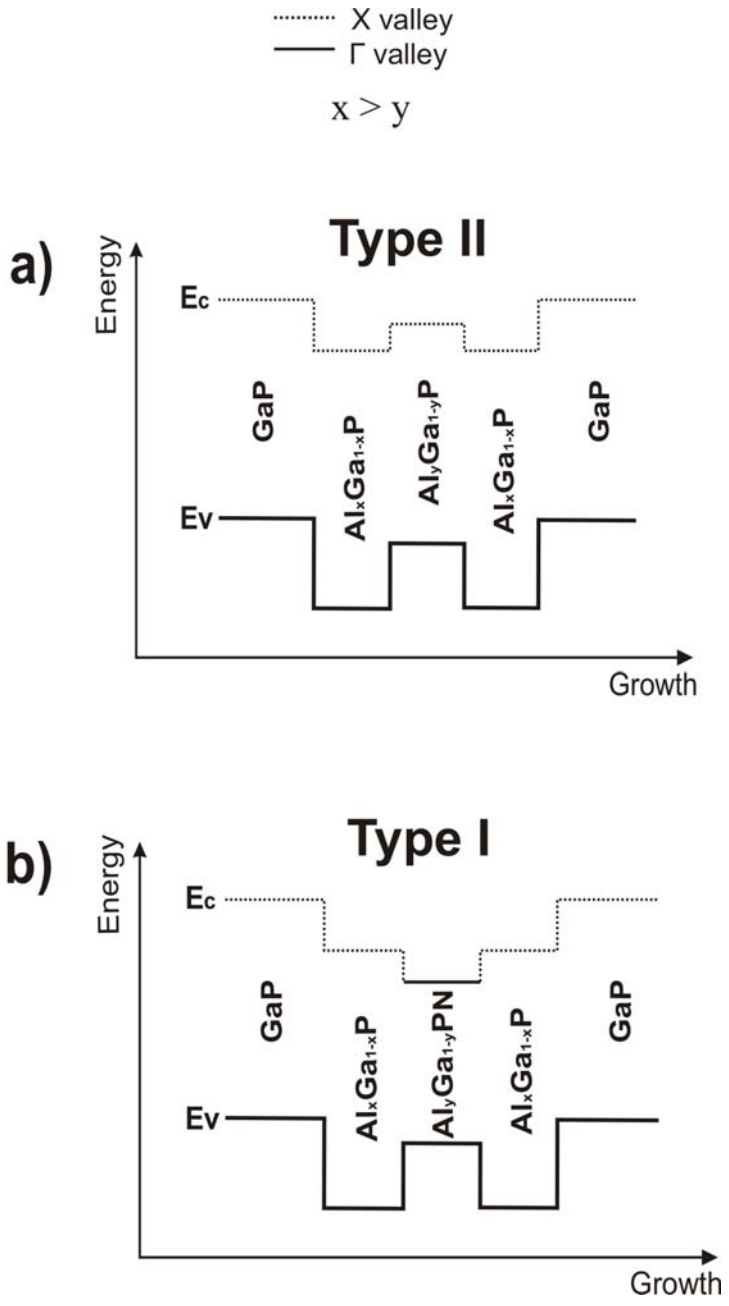

Figure 5.1. a) Band diagram of $Al_xGa_{1-x}P/Al_yGa_{1-y}P/Al_xGa_{1-x}P$ structure; b) band diagram of $Al_xGa_{1-x}P/Al_yGa_{1-y}NP/Al_xGa_{1-x}P$ structure for LED application.

Fig. 5.1a shows a band diagram of the LED structure without nitrogen in the $Al_yGa_{1-y}P$ active layer, which is sandwiched between $Al_xGa_{1-x}P$ cladding layers. $Al_yGa_{1-y}P/Al_xGa_{1-x}P$ form type-II heterojunction. Adding nitrogen into the $Al_yGa_{1-y}P$ active layer would result in converting the material from indirect band gap into direct band gap, and lowers the conduction band of $Al_yGa_{1-y}NP$ below the conduction band of $Al_xGa_{1-x}P$. This process results in the formation of a type-I heterojunction between $Al_yGa_{1-y}NP$ and $Al_xGa_{1-x}P$ layers (see Fig. 5.1b). Further experimental work is required to grow and optimize such an LED structure and observe electroluminescence in the green-yellow spectral range.

References:

[1] E. Fred Shubert, Light Emitting Diodes, p. 103, Cambridge, 2003.

[2] E. Fred Shubert, Light Emitting Diodes, p. 127, Cambridge, 2003.

Appendix A. Metamorphic growth of InGaP layers on GaP (100) substrates.

A.1. Overview

This appendix is devoted to the initial results on the growth and characterization of metamorphic InGaP layers on GaP (100) substrates for yellow-red light emitters. This is an alternate approach to the use of the (Al,In,Ga)NP material system, grown directly on a GaP (100) substrate, described in previous chapters.

The approach is to grow the desired light-emitting structure on a transparent, larger-lattice-constant $In_xGa_{1-x}P$ metamorphic buffer layer on a transparent GaP substrate. Metamorphic devices have been produced from Si_xGe_{1-x}/Si[1,2], $In_xGa_{1-x}As/GaAs$[3,4,5], $In_xGa_{1-x}As/InP$[6], and $In_xGa_{1-x}P/GaP$[7,8]. Close to 100% strain relaxation and reduction in threading dislocation density to below the detection limit of plan-view transmission electron microscopy (TEM), 10^6 cm^{-2}, have been reported[5,8]. The demonstrated high efficiency of strain relaxation is related to the control of misfit dislocation formation rates (in-plane between the substrate and the epitaxial layer) in the material. Our current approach differs from our previous work[7,8] in lowering the growth temperature to 400^0C and using quantum wells rather than bulk layers for the active region.

We present a systematic investigation of the structural and optical properties of InGaP using a metamorphic $In_xGa_{1-x}P$ buffer layer grown on GaP (100) substrates. Surface morphology of a metamorphic $In_xGa_{1-x}P$ buffer layer as dependent on substrate temperature is studied using AFM. Structural quality of the constant-composition and linearly graded metamorphic $In_xGa_{1-x}P$ is compared. $In_{0.5}Ga_{0.5}P$ quantum wells with $In_{0.3}Ga_{0.3}P$ barriers are grown on a constant-composition metamorphic buffer layer, and room-temperature photoluminescence is studied.

A.2. Growth and characterization details

All samples were grown by Gas Source Molecular Beam Epitaxy (GSMBE) with a Varian Gen II MBE system. Two sample structures have been studied, as shown in Fig. A.1. Sample structure #1 consists of a 0.5-μm-thick $In_xGa_{1-x}P$ metamorphic buffer layer followed by a 0.5-μm-thick $In_xGa_{1-x}P$ buffer layer. On top of this a 0.4-μm-thick $In_xGa_{1-x}P$ waveguide layer was grown, sandwiched between 0.03-μm-thick $Al_{0.3}Ga_{0.7}P$ barrier layers. 0.4 μm was chosen because it is similar to the typical thickness of the active region in AlInGaP-based LEDs. Finally, the structure was capped with a 10-nm-thick $In_xGa_{1-x}P$ layer. The composition *x* was varied for different samples. Sample structure #2 is the same as that of Structure #1 except a 7-nm-thick $In_yGa_{1-y}P$ quantum well inserted in the middle of the $In_xGa_{1-x}P$ waveguide layer with $y>x$. The metamorphic buffer layer of Structure #1 was grown two different ways: constant composition of $In_xGa_{1-x}P$ on GaP

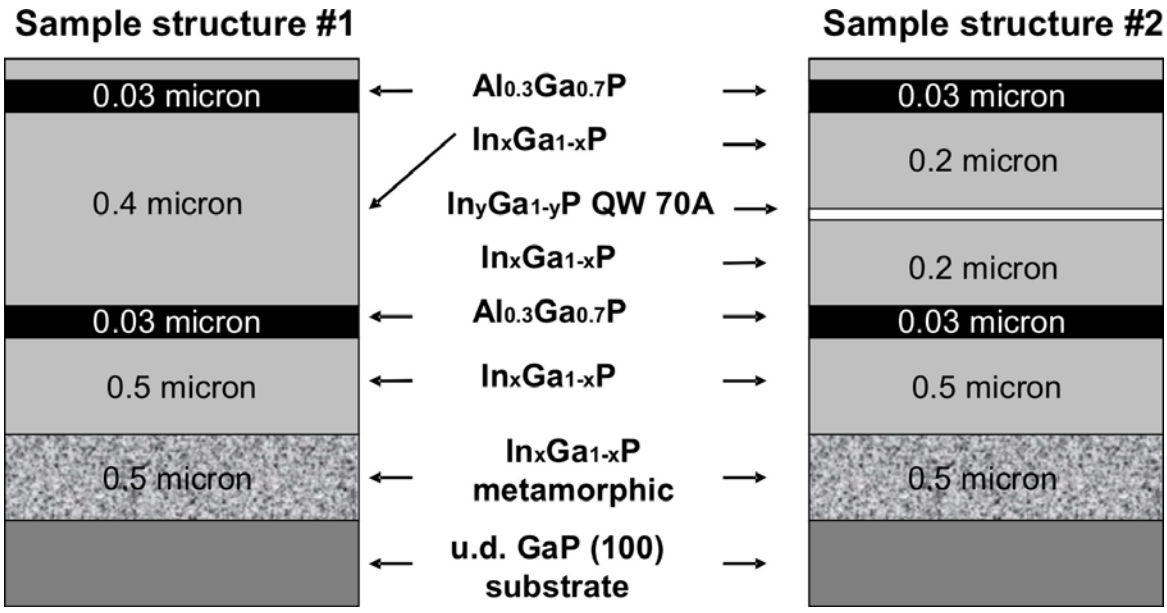

Figure A.1. Layer-by-layer schematic of Structures #1 and #2.

and linearly graded $In_xGa_{1-x}P$, where x was varied from 0 to the desired value by changing the temperature of the In cell during growth. The growth temperature of the layers subsequent to the metamorphic layer of all structures was kept to be 500^0C.

(400) x-ray rocking curves were measured by a Philips double-crystal diffractometer, and photoluminescence (PL) measurements were carried out at 20 K and 300 K using a 70 W/cm^2 Ar laser as the optical pumping precursor. A GaAs cathode photomultiplier tube was used to detect the signal at the exit of a 50-cm monochromator through a lock-in amplifier.

A.3. Optical and structural properties

Figure A.2 shows AFM images of 0.5-μm-thick constant-composition $In_{0.3}Ga_{0.7}P$ metamorphic buffer layers grown at substrate temperatures of (a) 500^0C and (b) 400^0C at 5 μm full scale (top row) and 20 μm full scale (bottom row). The metamorphic buffer layer grown at 400^0C shows much smoother morphology than that grown at 500^0C. The

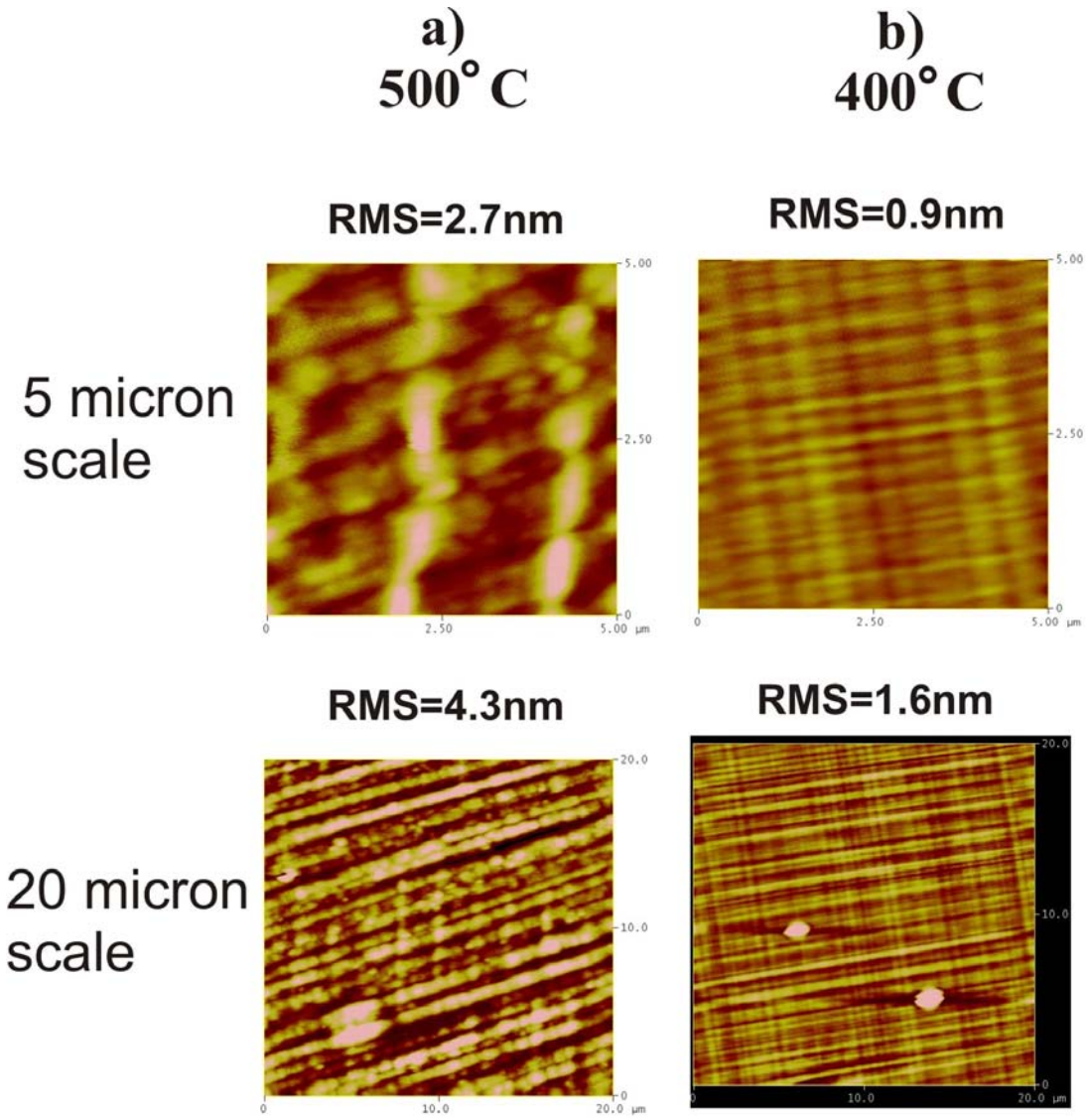

Figure A.2. AFM images at 5 μm (top row) and 20 μm (bottom row) full scale of the metamorphic buffer layer grown at (a) 500^0C and (b) 400^0C.

RMS roughness (shown in Fig. A.2) of the buffer layer grown at 400^0C is one third that grown at 500^0C. This is in agreement with the results reported for InGaAs/GaAs[5], which show that constant-composition InGaAs metamorphic buffer layer grown on GaAs at 450^oC or lower results in injection lasers emitting at 1.3 μm due to much reduced threading dislocations. Without the metamorphic buffer layer, i.e., direct growth of a constant-composition layer at higher temperatures shows three orders of magnitude higher threading dislocation density (10^9 cm^{-2}), and injection lasers could not be realized. Thus, a metamorphic layer is required.

Our earlier work demonstrates that a linearly graded $In_xGa_{1-x}P$ metamorphic layer, grown on GaP at a substrate temperature varying from 650^oC to 500^oC as *x* is varied from 0 to 0.3, confines the dislocations and results in reduced threading dislocation density in the top layer[7]. To check the influence on crystal quality of a linearly graded metamorphic buffer layer grown at a low temperature of 400^oC, we compare two Structure #1 samples with $In_{0.3}Ga_{0.7}P$: one with a 0.5-μm-thick linearly graded $In_xGa_{1-x}P$ (*x* from 0 to 0.3) metamorphic buffer layer and the other with a 0.5-μm-thick constant-composition metamorphic buffer layer. X-ray rocking curves of these two structures are shown in Fig. A.3. The peak positions of the x-ray curves are the same for both structures as expected. The x-ray signal between the epi-layer peak and the substrate peak in Curve #1 represents the linearly graded metamorphic buffer layer. The FWHMs of the epilayer peaks for both samples are the same (around 700 arcsec), which means that linear grading grown at low temperature (400^oC) results in comparable structural quality of the subsequent InGaP epilayer as the simpler process of constant composition grown at the same temperature.

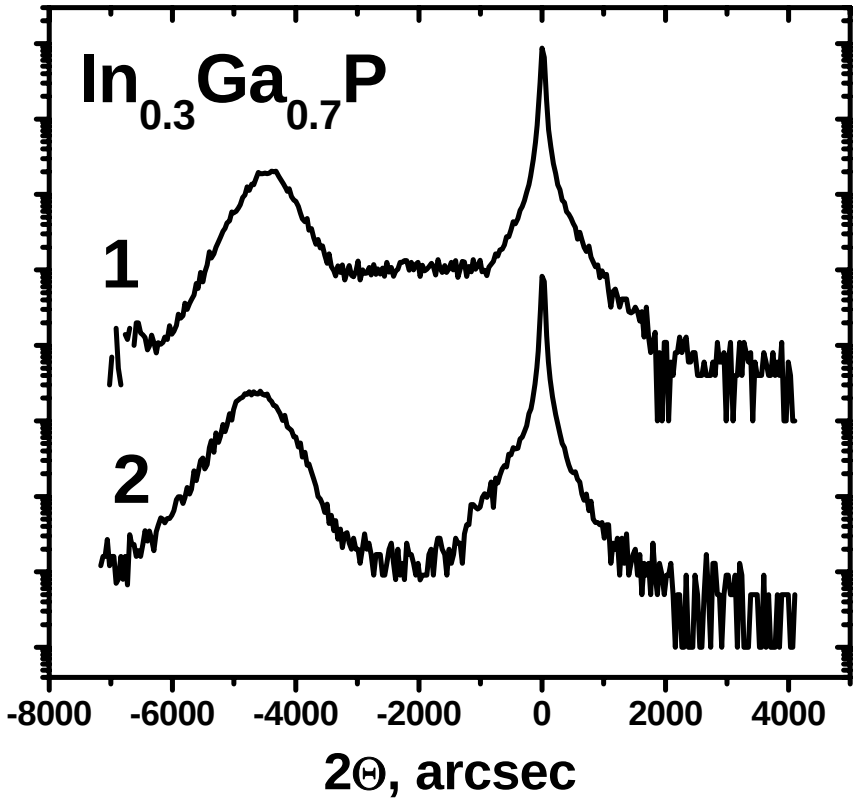

Figure A.3. (400) x-ray rocking curves of Structures #1: 1- $In_xGa_{1-x}P$ linearly graded (x from 0 to 0.3) metamorphic buffer layer; 2- $In_{0.3}Ga_{0.7}P$ constant-composition metamorphic buffer layer.

Therefore, for subsequent samples we use a constant-composition metamorphic buffer layers grown on GaP (100) substrates at 400^0C.

Figure A.4 shows the dependence of the FWHM of x-ray peak vs. indium composition (0.22, 0.30, 0.36, and 0.42) in the metamorphic layer (0.5 μm thick).The FWHM remains almost the same when the In composition is less than 0.30. When the indium composition exceeds 0.3, the FWHM starts to increase rapidly, indicating degradation of structural quality due to increased lattice mismatch. The FWHM increases

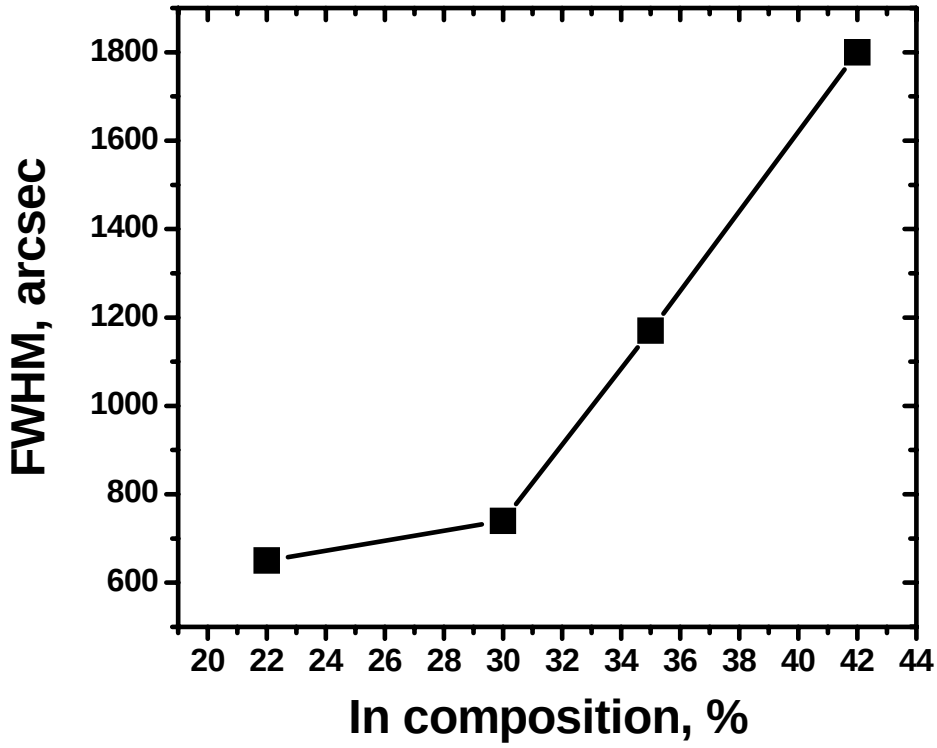

Figure A.4. Dependence of FWHM of x-ray peak vs. indium composition in the structures of Fig. A.3.

from 740 arcsec to 1800 arcsec when the In composition increases from 0.30 to 0.42. This means that using a 0.5-μm-thick metamorphic layer containing more than 30% of In is not reliable.

A series of Structure #1 with different In composition *x* (0.26, 0.30, 0.35, and 0.41) was grown for photoluminescence measurements. The PL spectra of these structures, taken at 20 K, are presented in Fig. A.5a. With increasing indium composition, a red shift of PL peak position is clearly observed. The dependence of PL peak wavelength on In composition is shown in Fig. A.5b. While the In composition is

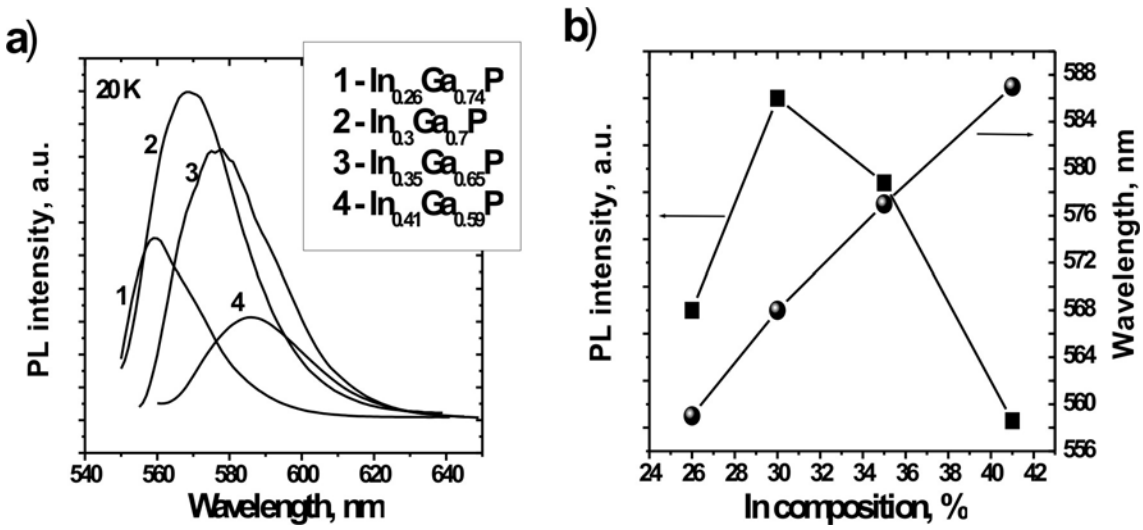

Figure A.5. a) PL spectra (recorded at 20 K) of a series of Structures #1 samples with different x; b) dependence of PL peak position and PL intensity on In composition.

increased from 0.26 to 0.41, the emission wavelength shifts from 559 to 587 nm. The PL intensity increases first for $0.25<x<0.3$, and then it starts to decrease for $x>0.3$. This non-monotonic behavior of PL intensity vs. In composition can be explained by several reasons. InGaP becomes direct bandgap when [In]>0.25, and the PL intensity increases. When $x>0.30$ the crystal quality of the structure degrades, as shown in Fig. A.4, and the PL intensity decreases. In that case, a thicker metamorphic layer is required.

Finally, a sample of Structure #2 (x=0.30, y=0.50, well width W=7nm) was grown in order to obtain room-temperature light emission with peak wavelength around 600 nm. Figure A.6 shows the PL spectra recorded at 20K (curve 2) and 300K (curve 1). Room-temperature PL with peak wavelength at 610 nm was observed. Low-temperature PL shows two peaks. The high-energy peak at 568 nm corresponds to the $In_{0.3}Ga_{0.7}P$ waveguide layers and agrees well with the PL peak position of bulk $In_{0.3}Ga_{0.7}P$ in Fig.

A.5a. The low-energy peak at 594 nm corresponds to the $In_{0.5}Ga_{0.5}P$ QW emission. There is no low-energy defect-related tail, which means good structural quality of the sample.

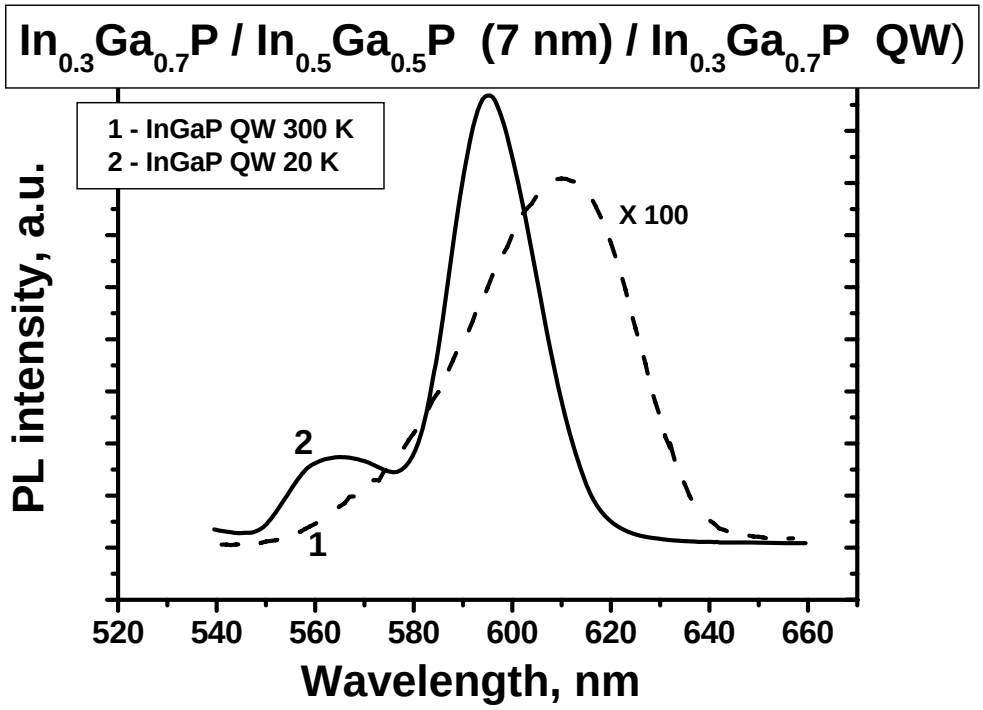

Figure A.6. Room-temperature (curve 1) and low-temperature (curve 2) PL spectrum of Structure #2 with $In_{0.3}Ga_{0.5}P/In_{0.5}Ga_{0.5}P$ (7 nm)/$In_{0.3}Ga_{0.7}P$ QW.

A.4. Conclusions.

Structures with an $In_xGa_{1-x}P$ metamorphic buffer layer grown on GaP(100) were investigated. The morphology of the metamorphic buffer layer is much smoother when grown at 400^0C than at 500^0C. When grown at 400^0C, a constant-composition metamorphic buffer layer results in comparable structural quality of the top layers as a

linearly graded metamorphic buffer layer. When the In composition of a 0.5 μm-thick constant-composition $In_xGa_{1-x}P$ buffer layer is less than 0.30, the structural quality remains good. When x>0.30 the structural quality degrades rapidly with increasing x, and a thicker (>0.5 μm) metamorphic layer is required. PL spectra of Structures #1 show red shift of the PL peak position with increasing x. The PL intensity vs. x dependence has a maximum around x=0.30 because of indirect-direct cross over point of $In_xGa_{1-x}P$ at x around 0.26 and degradation of the sample crystal quality when x>0.30. A peak wavelength of 610 nm of room-temperature PL emission from an $In_{0.3}Ga_{0.7}P$/ $In_{0.5}Ga_{0.5}P$ (7 nm)/ $In_{0.3}Ga_{0.7}P$ QW grown on a constant-composition $In_{0.3}Ga_{0.7}P$ metamorphic buffer layer on GaP (100) was achieved.

Materials in this Appendix were published in Journal of Crystal Growth 279, 20 (2005).

References:

[1] E. A. Fitzgerald, Y. H. Xie, M. L. Green, D. Brasen, A. R. Kortan, J. Michel, Y. J. Mii, and B. E. Weir, Appl. Phys. Lett. **59**, 811 (1991).

[2] F. K. LeGoues, B. S. Meyerson, and J. F. Morar, Phys. Rev. Lett. **66**, 2903 (1991).

[3] J. C. P. Chang, J. Chen, J. M. Fernandez, H. H. Weider, and K. L. Kavanagh, Appl. Phys. Lett. **60**, 1129 (1992).

[4] S. M. Lord, B. Pezeshki, S. D. Kim, and J. S. Harris Jr., J. Crystal Growth **127**, 759 (1993).

[5] A. E. Zhukov, A. R. Kovsh, S. S. Mikhrin, E. S. Semenova, N. A. Maleev, A. P. Vasil'ev, E. V. Nikitina, N. V. Kryzhanovskaya, A. G. Gladyshev, Yu. M. Shernyakov, Yu. G. Musikhin, M. V. Maksimov, N. N. Ledentsov, V. M. Ustinov, and Zh. I. Alferov, Semiconductors, 37, 1119 (2003).

[6] A. Fisher-Colbrie, R.D. Jacowitz and D.G. Ast, J. Crystal Growth 127, 560 (1993).

[7] T. P. Chin, J. C. P. Chang, K. L. Kavanagh, C. W. Tu, P. D. Kirchner and J. M. Woodall, Appl. Phys. Lett. **62**, 2369 (1993).

[8] J. C. P. Chang, T. P. Chin, C. W. Tu and K. L. Kavanagh, Appl. Phys. Lett. 63, 500 (1993).